SERF is a modifier of amyloid formation

Dissertation

zur Erlangung des

Doktorgrades der Naturwissenschaften (Dr. rer. nat.)

der

Naturwissenschaftlichen Fakultät I – Biowissenschaften –

der Martin-Luther-Universität

Halle-Wittenberg,

vorgelegt

von Herrn Ben Alexander Meinen

geb. am 29.01.1990 in Düsseldorf

Content

Content

Figures and Tables

Summary

As the global population ages, the number of people suffering from neurodegenerative disorders like Alzheimer's (AD) and Parkinson's (PD) disease is expected to more than double between now and the year 2050. For Alzheimer's disease (Aβ40/42) and Parkinson's disease (α-synuclein) patients the assembly of small disordered proteins into highly ordered amyloid fibrils is closely associated with dementia and neurodegeneration. An in-depth understanding of the process of amyloid formation is thus essential for the development of effective treatments for these devastating neurodegenerative diseases. A small, highly conserved protein called SERF was discovered to modify amyloid formation in *Caenorhabditis elegans* and humans.

In this thesis, I characterize the *Saccharomyces cerevisiae* homologue ScSERF and its effect on amyloid formation of the amyloid proteins Aβ40 and α-synuclein. The structural characterization revealed an intrinsically disordered protein, with the propensity to form a C-terminal α-helical structure at low temperatures. The small sizes of ScSERF, Aβ40 and α-synuclein allows us to study the mechanism of amyloid formation and how it is affected by ScSERF in great detail. I used kinetic amyloid measurements to identify that ScSERF affects the rate of primary nucleation in amyloid formation for both amyloid proteins.

I found that ScSERF binds to monomeric Aβ40 and α-synuclein present during primary nucleation. Primary nucleation is the initial and slowest step of amyloid formation. Nuclei formation is difficult to observe because the nuclei species are extremely short-lived due to the rapid equilibrium between monomeric states, nuclei and elongated fibrillar aggregated states. To study the early steps of amyloid formation we utilized native ion-mobility mass-spectrometry. The data revealed that multiple ScSERF conformations interact with various conformations of monomeric Aβ40 and α-synuclein to form structurally diverse, fuzzy complexes. The complexes also exist in different stoichiometries of ScSERF to Aβ40 and α-synuclein (1:1, 2:1, 1:2, or 2:2). These structural diverse complexes are present during primary nucleation. This work shows for the first time that two human disease-related amyloid proteins form elongated fuzzy complexes with a conserved modifier of amyloid formation, ScSERF. The results suggest that the structural changes occurring during primary nucleation are more diverse and comprise more than just one amyloid-prone conformation.

Zusammenfassung

Der demographische Wandel hin zu einer immer älter werdenden Gesellschaft führt dazu, dass Menschen zunehmend an neurodegenerativen Erkrankungen wie Alzheimer oder Parkinson leiden werden. Es wird prognostiziert, dass sich die Zahl der Erkrankten mit der Diagnose Alzheimer und Parkinson bis zum Jahr 2050 mehr als verdoppelt. Bei diesen Erkrankungen formen die amyloid-bildenden Proteine Aβ40/42 und α-Synuclein jeweils durch Selbstassoziation unlösliche Amyloidfibrillen, die zu Demenz und Neurodegenerationen führen. Das kleine, evolutionär hochkonservierte Protein SERF wurde als neuer amyloid-modifizierender Faktor im Modelorganismus *Caenorhabditis elegans* und in menschlichen Zellen entdeckt. In dieser Arbeit habe ich das bisher unbekannte homologe Protein aus *Saccharomyces cerevisiae* ScSERF strukturell charakterisiert und den Mechanismus wie ScSERF die Fibrillerungskinetik der zwei amyloid-bildenden Proteine Aβ40 und α-Synuclein beeinflusst, aufgeklärt.

Die Struktur von ScSERF wurde mittels CD- und NMR-Spektroskopie untersucht und zeigten, dass ScSERF ein intrinsisches, ungeordnetes Protein ist.

Zur funktionellen Charakterisierung wurde die Fibrillierung mittels ThT-Fluoreszenz gemessen. Die Kinetik zeigte, dass ScSERF den ersten Nukleationsschritt (*primary nucleation*) der Fibrillenbildung beschleunigt. In diesem ersten Schritt findet eine Konformationsänderung der Monomere hin zu Strukturen (*Nuclei*), die Fibrillen bilden, statt. Diese *Nuclei* sind kurzlebig und aufgrund des sich schnell einstellenden Gleichgewichts zwischen Monomer, *Nuclei* und Fibrillen schwer zu detektieren.

Die Protein-Protein Interaktion zwischen ScSERF und den amyloid-bildenden Protein wurde mittels Fluoreszenz-Anisotropie und nativer Massenspektrometrie untersucht. ScSERF interagiert mit Aβ40 und α-Synuclein in ihrer monomeren Form. Die native Massenspektrometrie zeigte außerdem, dass ScSERF in mehreren Konformationen existiert und beide amyloid-bildenden Proteine in mehreren Konformationen binden kann. Eine Ansammlung von strukturell verschiedenen Proteinkomplexen zwischen ScSERF und Aβ40/α-Synuclein konnte während des ersten Nukleationsschritt (*primary nucleation*) detektiert werden. ScSERF und beide amyloid-bildenden Proteine interagieren auch in verschiedener Stöchiometrie (1:1, 1:2, 2:1, 2:2) miteinander.

Proteinkomplexe zwischen dynamischen und strukturell ungeordneten Proteinen können als „*fuzzy*"-Komplexe klassifiziert werden. Hier wurde zum ersten Mal diese Art von strukturell

dynamischen Proteinkomplexen im Kontext des amyloid-modifizierende Proteins ScSERF und den zwei amyloid-bildenden Proteinen Aβ40 und α-Synuclein gezeigt. Die Ergebnisse belegen, dass die strukturellen Veränderungen in der frühen Phase des Fibrillierungsprozesses komplexer sind, als bisher angenommen und mehr als nur eine amyloid-bildene Konformation vorliegt.

1 Introduction

1.1 Protein homeostasis

Most proteins must be correctly folded and assembled to be functional. A eukaryotic yeast cell for instance contains around 6000 different proteins and a human cell expresses even more than 10 000 proteins. The abundance of a protein varies from cell to cell, ranging from fewer than 50 molecules up to over 10 million molecules per cell[1].

A protein must fold into its correct three-dimensional structure, or native state, in order to function properly. For most proteins, the native state is a compromise between thermodynamic stability and conformational flexibility. Conformational change is often essential for protein function, however this flexibility results in marginal stability for proteins in their physiological environment and can lead to misfolding and aggregations[2–4]. A subset of about 30 % of proteins in mammalian cells are predicted to be intrinsically unstructured proteins which can adopt stable structures upon binding to interaction partners or can even remain unstructured while present in complex[5,6]. Furthermore, the cellular environment is crowded with an approximate protein concentration of 300 mg/ml[7]. Macromolecular crowding increases the tendency of misfolded or unstable proteins to from non-native contacts and aggregates compared with dilute solutions[7].

On the path to its native state, the polypeptide chain explores a funnel-shaped potential energy surface which represents the large number of possible conformations the protein can adopt. The folding process relies on multiple weak, noncovalent interactions. Although the native state is the lowest energy structure for a single protein, misfolded proteins can adopt harmful aggregated states, which may have a lower free energy state than native proteins. Misfolded and aggregated states can engage in nonnative interactions that can be harmful to the cell either because they decrease the function of the proteins that are part of the aggregate or because the misfolded proteins themselves are toxic. To combat harmful interactions that result from protein misfolding, cells have evolved to create a network of proteins that prevent protein misfolding and keep protein homeostasis (Fig. 1).

Protein homeostasis describes a network of factors that control the levels of functional proteins and minimize harmful off-pathway reactions (e.g. misfolding or protein aggregation). Protein synthesis, folding, conformational maintenance, localization, and degradation all contribute to protein homeostasis (Fig. 1)[1].

Molecular chaperones are proteins that assist the folding and assembly of proteins without being part of the final structure. Molecular chaperones can be classified into two broad categories: ATP-dependent chaperone foldases (e.g. GroEL, Hsp70, Hsp90) and ATP-independent holdases (e.g. HdeA, Hsp33, small Hsps) which are often stress-induced[8]. Molecular chaperones also cooperate with the ubiquitin-proteasome system and autophagy to degrade misfolded or aggregate proteins (Fig. 1).
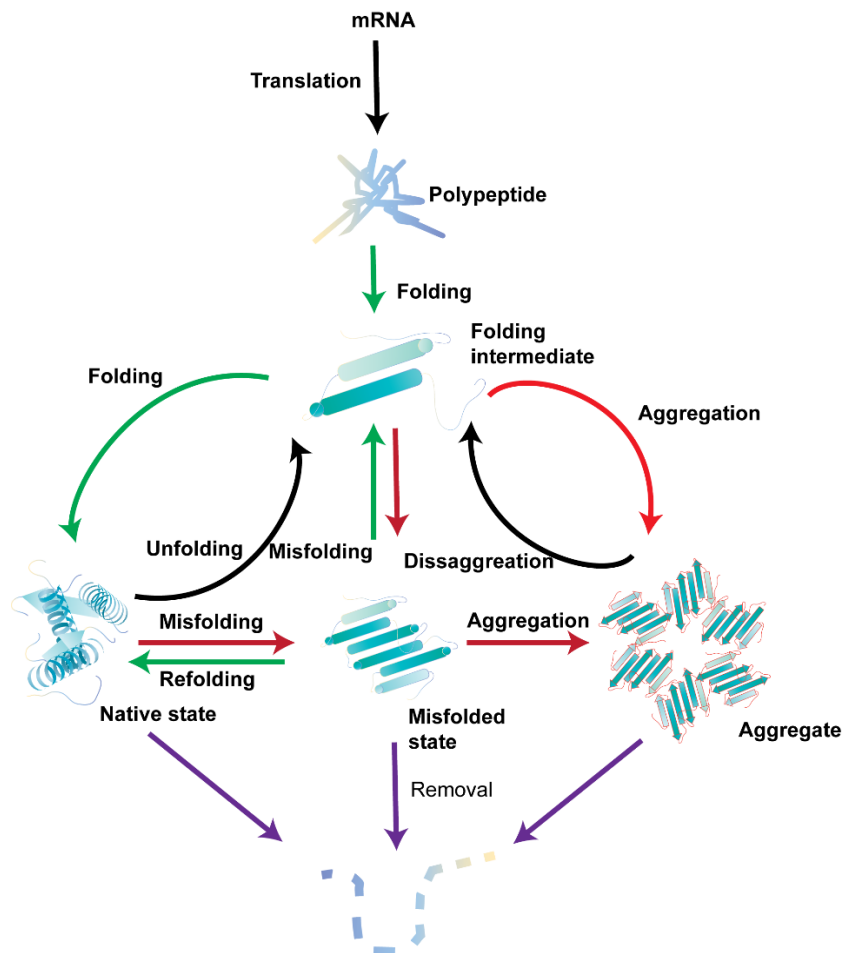
Figure 1: Proteostatsis network
The proteostasis network encompasses all proteins and pathways necessary to stabilize proteins in their native state and reduce the amount of dysfunctional and dangerous protein misfolding and aggregation (red arrows). The protein synthesis and folding cluster contains about 400 different proteins (green arrows). Proteins and pathways that responsible for maintaining conformational stability have about 300 protein members (black arrows). The pathways of protein degradation prominently ubiquitin-proteasome system and the autophagosome-lysosomal system have over 1000 protein members (purple arrows) (figure adapted after Hipp MS et al. (2019))[1].

Acute stress like elevated temperatures or the presence of reactive oxygen species and chronic stress conditions can lead to protein misfolding and aggregation. Protein aggregation can overwhelm the chaperone network's capacity and lead to an accumulation of misfolded and aggregated proteins. A range of diseases have been associated with protein misfolding and

aggregation[9]. Two kinds of protein aggregates are distinguishable: amorphous aggregates and amyloid fibrils. Amorphous aggregates can occur when proteins are partially or completely unfolded and expose hydrophobic regions, which are buried in the core of a native protein, and these sticky hydrophobic patches bind to other hydrophobic regions or non-specifically to other proteins resulting in insoluble protein aggregates. One example of an amorphous aggregates involved in disease is cataracts which can be caused by the aggregation of various crystallin's[10]. Amyloids are ordered cross-β structures consisting of parallel or anti-parallel β-strands that assemble perpendicular to the long fibril axis. The cross-β scaffold is stabilized by an extended H-bonding network of backbone amides[11].

Amyloid fibrils are the hallmark of neurodegenerative diseases including Alzheimer's, Parkinson's, and Huntington's and other diseases including Type II diabetes, Lysozyme amyloidosis and AL amyloidosis[12]. Amyloid fibrils are visible as insoluble inclusions in patients illustrated in Fig. 2 for Alzheimer's and Parkinson's patients.

Amyloid formation and protein aggregation can cause cellular dysfunction and eventually cell death. There are several mechanisms by which protein aggregation can be harmful to the cell[1,12]. One is the nonspecific interaction of these aggregates with other cellular proteins or RNA molecules. These interactions sequester proteins into aggregates and leads to the loss of their function in the cell. If the proteostasis network reaches its capacity and becomes overwhelmed with protein aggregates, more aberrant interactions of cellular proteins can occur and more protein aggregates can form creating a feedback loop that can lead to a collapse of protein homeostasis (Fig. 2 B)[12]. Proteins sequestered in protein aggregates tend to be metastable and characteristically contain intrinsically disordered regions or low complexity domains[13]. Another mechanism of toxicity is the interaction between oligomers and aggregates with biological membranes, which creates pores that in turn can disrupt protein localization or damage ion gradients that are important for cellular function[1,14]. The generation of reactive oxygen species (ROS) upon protein aggregation can lead to further damage to the cell[15].

It has been recognized that the protein homeostasis capacity declines with age[16]. The biological reasons for the decline of proteostasis network with aging are complex and not fully understood. One reason for this decline may be the lack of evolutionary pressure to maintain the proteome beyond the point when the organism has reproduced and passed on their genomic information to the next generation[17]. Studies using the model system *C. elegans* show that the proteasome changes significantly as a function of age[18]. Therefore, targeting the protein homeostasis network may be a promising strategy to target age-related protein aggregation.
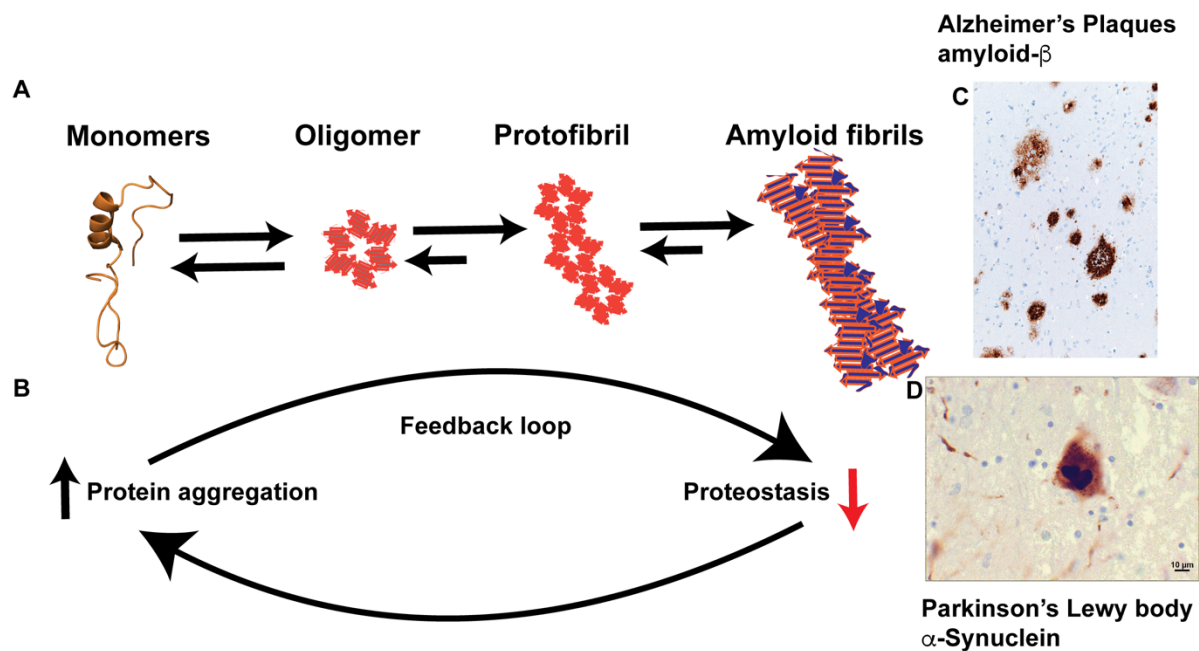
Figure 2: Amyloid aggregation scheme
(A) Amyloid formation starts from a monomeric, often intrinsically disorder proteins, that can self-assemble into oligomeric intermediates, that form protofibrils, that ultimately form amyloid fibrils in amyloid deposits. (B) Decline in proteostasis leads to an increase in protein aggregation, which can overwhelm the proteostasis system leading to a further decline in proteostasis network causing a vicious cycle. (C) Image of amyloid-β plagues in Alzheimer's patients (D) Image of Lewy body in Parkinson's patients. Images (C, D) are creative-common-license (CC-BY, wikipedia.org).

1.2 Protein disorder and its connection to misfolding diseases

Intrinsically disordered proteins (IDPs) lack a distinct three-dimensional structure and exist as an ensemble of multiple conformations[19]. Despite the lack of well-defined structures, intrinsically disordered proteins are important for the regulation of transcription and the cell cycle[20,21]. The ability of intrinsically disordered proteins to be functional is due to some advantage IDPs have in the separation of binding specificity and affinity, and their adaptability to various binding partners. Intrinsically disordered proteins can often adopt a stable structure when interacting with a well-folded binding partner[22]. It has been found that the affinity of IDPs in protein complexes spans a range from low nanomolar to micromolar affinities[23].

In other cases, intrinsically disordered proteins do not undergo a disorder-to-order transition but instead engage in fuzzy complexes. The term fuzzy complex is based on the concept of fuzzy logic, where a value can range between 0 and 1, indicating an inherent ambiguity in describing the structural state of the complex[24]. Therefore, fuzzy complexes cannot be described by one defined structure. A challenge in studying these complexes is the existence of multiple states that often undergo fast conformational exchange. One example of a complex

with extreme disorder is the interaction between the two intrinsically disordered proteins histone H1 and prothymosin-α. In this complex both proteins keep their disordered structure without adopting a folded ensemble[5].

Extended conformations of intrinsically disordered proteins make them prone to engage in unintended interactions that can result in protein aggregation. Therefore, structural transitions of intrinsically disordered proteins in misfolded states have been associated with a range of diseases associated with protein misfolding, especially neurodegenerative diseases like Alzheimer's disease, Parkinson's disease, Huntington disease and the prion diseases[12].

For example, the intrinsically disordered proteins, amyloid-β protein and tau protein are associated with Alzheimer's disease (AD), and the IDP α-synuclein forms amyloid fibrils in Parkinson's disease (PD). In Huntington disease, polyglutamine expansion in the huntingtin protein (HTT) leads to a partially disordered protein resulting in protein misfolding and amyloid formation[25]. Proteins forming amyloid fibrils in disease do not exhibit any obvious similarities in terms of sequence, size or expression and in vivo function[26,27].

This thesis is focused on two important disease associated IDPs, the amyloid-β protein (Aβ 40) which is involved in Alzheimer's and α-synuclein which is involved in Parkinson's. Alzheimer's disease (AD) is the world's most prevalent neurodegenerative disease. In 2030, the world's population of AD patients will exceed 70 million. It is sobering to realize that nearly one in three people over the age of 85 years will develop Alzheimer's disease. The histopathological hallmarks in Alzheimer's patients are intracellular neurofibrillary tangles (tau) and amyloid plaques (amyloid-β) peptide (Fig. 2C)[28].

The amyloid-β peptide is generated by proteolytic cleavage of the amyloid precursor protein (APP). The amyloid precursor protein (APP) is a transmembrane protein, and it is physiological function has not been clearly established[29]. The amyloid cascade hypothesis first described by Hardy and Selkoe[30] identifies amyloid-β as the causative agent in AD pathology. Amyloid-β aggregation is followed by the formation of neurofibrillary tangles and culminates in neuronal loss which leads to the symptoms of Alzheimer's disease[31].

In non-amyloidogenic cases the extracellular domain of APP is cleaved by α-secretase and γ-secretase resulting in the peptide p3. The peptide p3 is 24 to 26 amino acids long and is missing the N-terminal 16 residues present in Aβ40/42. Aβ40/42 are the cleavage products that accumulate when β-secretase cleaves the extracellular domain of Aβ instead of α-secretase[32].

Aβ40/42 sequences has three distinguishable parts a flexible and unstructured N-terminus (residues 1-15), a central hydrophobic region (residues 17-21) and a hydrophobic C-terminus (residues 34-40)[13].

Parkinson's disease (PD) worldwide is the second most common neurodegenerative disease affecting around 1 % of the world population over 65 years. The histopathological hallmark for PD is the aggregation of α-synuclein in Lewy bodies and Lewy neurites. Several point mutations (e.g. A30P, A53T. E46K) in the gene encoding α-synuclein, have been linked to familial early on-set Parkinson's disease that occurs approximately at 40 years of age[33,34]. Some mutations (e.g. A53T) accelerate the formation of amyloid fibrils, or lead to the formation of more toxic oligomeric species[34]. The molecular mechanism linking the amyloid aggregation of α-synuclein into Lewy bodies and the development of PD is not yet clear (Fig. 2 D)[35].

α-synuclein itself is an intrinsically disordered protein that contains three domains, a N-terminal domain (residue 1–60), a central domain (61-95) and a C-terminal domain (61-95)[36]. The N-terminal domain contains an apolipoprotein lipid-binding motif and is predicted to form an amphiphilic helix when bound to membranes. The central domain is the so-called non-amyloid-β component (NAC) domain with multiple hydrophobic regions. Lastly, the C-terminal domain is a disordered highly negatively charged and proline-rich part of the protein[36].

1.3   Investigation of amyloid formation in vitro

Current evidence points toward the idea that it is the process of amyloid formation rather than the presence of amyloid plaques that leads to neurodegeneration[37,38]. Thus, elucidating the mechanism, process and external factors that lead to amyloid formation can potentially provide information that may eventually lead to measures to inhibit or prevent amyloid associated neurodegeneration. There are several methods that allow us to study the mechanism of amyloid formation in vitro.

Measuring amyloid kinetics by fluorescence spectroscopy

Monitoring the kinetics of amyloid formation is commonly performed with the fluorescence dye Thioflavin T (ThT) (Fig. 3). As ThT binds to amyloid fibrils, its excitation maximum shifts from 385 nm to 450 nm and its emission maximum shifts from 445 nm to 482 nm. ThT free in solution has a rotating carbon-carbon bond between the benzylamine and benzathiole ring, and the rotation of this bond quenches the excited state. In the amyloid fibril bound state, ThT is sterically restricted to one conformation and this prevents excited state quenching[39]. This

excited state results in a large enhancement of the fluorescence emission and this makes ThT a very sensitive dye for the detection of amyloid fibrils. A typical amyloid aggregation experiment with Thioflavin T results in a sigmoidal curve. Unfortunately, the early steps of amyloid formation that occur during the lag-phase are invisible in a ThT-assay.

Kinetic of amyloid formation

As described above, the use of the fluorescence dye Thioflavin T enables the overall, macroscopic monitoring of amyloid formation. The challenge is to interpret this result in quantitative terms by extracting microscopic rates that help us understand the fundamental steps involved in the process of amyloid formation. Recent advances in studying the process using chemical kinetics led to the generation of a mathematical framework describing the mechanism[40]. This new framework, was successfully applied by the Knowles group to characterize the mechanism underlying the amyloid formation of Aβ40/42[41]. They found self-assembly of Aβ40/42 peptides to be composed of several microscopic steps; primary nucleation, elongation and secondary nucleation (Fig. 3). In general, amyloid formation follows a nucleation-dependent polymerization mechanism.
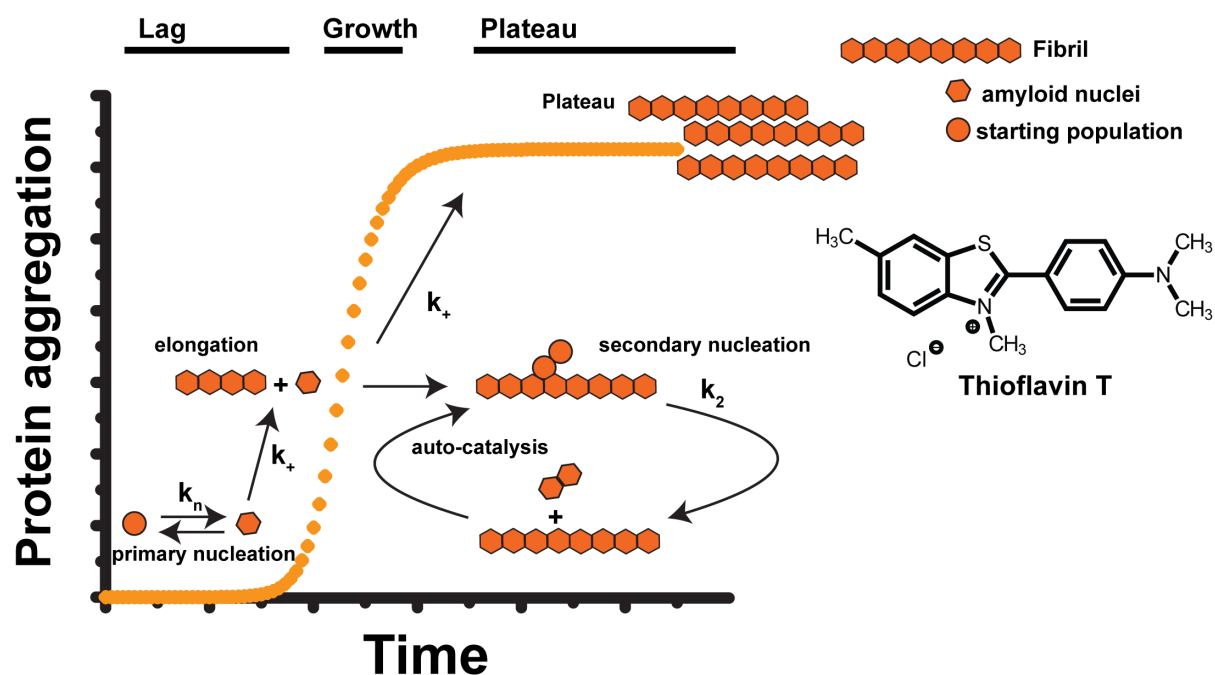
Figure 3: Mechanism of amyloid formation.
Amyloid kinetics studied in vitro under non-seeding conditions generally follows a sigmoidal curve. During the lag phase, the process of primary nucleation k_n takes place. The growth phase contains two processes, elongation (k_+) and secondary nucleation (k_2). The plateau indicates the complete consumption of monomeric protein into amyloid fibrils. The insert shows the structure of the dye Thioflavin T.

Primary nucleation

Primary nucleation is the initial step which occurs when the amyloid protein exists in its monomeric state in solution. In a typical ThT kinetic curve, primary nucleation is represented by a lag-phase, where the signal of protein aggregation as read out with ThT fluorescence does not change. This apparent lag-phase occurs because ThT only interacts with cross-β structures in amyloid fibrils, or amyloid-like states. Protein monomers undergo structural changes to form nuclei that are susceptible to aggregation. These amyloid nuclei consist of unstable amyloid-like states that have the same probability of elongating into amyloid fibrils and reverting back to disordered monomeric states. Primary nucleation is the slowest step of amyloid formation in part due to the high free energy barrier of nuclei formation. It is the only step depending on monomeric protein[42]. Nuclei that are formed can engage in the processes of elongation and secondary nucleation. Historically it has been difficult to observe the structure or state of nuclei, in part because they are extremely short-lived due to the rapid equilibrium between monomeric states, nuclei and elongated fibril states[43,44].

Secondary nucleation

Secondary nucleation describes the step of forming nuclei on the surface of preexisting fibrils. It has been shown that this step is important in generating more fibril mass during amyloid formation for Aβ40/Aβ42. It is thought that monomers can attach to the fibril surface and undergo a conformational change into nuclei, these nuclei can dissociate from the fibril surface and then can elongate into longer fibrils. Secondary nucleation occurs after a critical concentration of fibrils has been formed and is responsible for the formation of more nuclei than primary nucleation[45,46]. The rate of secondary nucleation is also dependent on the monomer concentration in solution but can reach saturation for Aβ40. Because the rate is dependent on the rate of monomer association onto fibril surfaces rather than on dissociation of formed nuclei from the fibrils, secondary nucleation creates a positive feedback loop that drives the autocatalytic nature of amyloid formation[45,46]. The rate of secondary nucleation can be altered by screening electrostatic repulsion through salt concentration or by changing the amyloid β charge distribution through mutation, some of which are associated with early onset of AD[47].

Elongation

Elongation describes the step in which monomeric protein attaches to the fibril ends. It thus leads to the formation of long fibril structures. Elongation results in the sigmoidal growth phase during amyloid formation. Elongation rate can be influenced by protein modifiers that bind to fibril ends or change the attachment of monomers to the fibrils[48].

Fragmentation

The process of fragmentation is characterized by breakage of fibrils, this mostly occurs through external force and leads to the production of new fibril ends that are available for elongation[49]. By using constant shaking as an external force, fragmentation can be induced, and this results in an acceleration of amyloid formation[50]. Amyloid formation for α-synuclein in vitro occurs on a slow timescale (e.g. 5 to 7 days) under quiescent conditions[51]. The artificial introduction of a fragmentation step allows one to study of amyloid formation on a more experimentally reasonable time-scale (< 3 days). Unfortunately, under fragmentation inducing conditions, e.g. during constant shaking, the different contributions of the other microscopy steps like secondary nucleation processes are obscured by this artificially induced fragmentation step.

Mechanism of α-synuclein amyloid formation

In contrast to the detailed study of the microscopic rate constants involved in the amyloid formation of Aβ40, the kinetics of α-synuclein are less well studied. This is due to persistent experimental limitations e.g. slow amyloid aggregation under neutral pH[51]. α-synuclein aggregation at neutral pH and under quiescent conditions, conditions comparable to the ones used for Aβ40/42, takes 5 to 7 days. In vitro it has been shown that α-synuclein amyloid formation is accelerated by high ionic strength buffers or low pH or by constant shaking. The rate of secondary nucleation is strongly accelerated if the pH of the reaction is made mildly acid (pH< 5.5), and this results in the acceleration of the rate of amyloid formation[51]. At neutral pH, α-synuclein amyloid formation is dominated by the elongation step, no significant contribution of a secondary nucleation step has been observed[52].

For α-synuclein, the elongation rate k_+, which corresponds to the addition of monomers to fibril ends, has been estimated to be 2×10^3 M^{-1} s^{-1} at 37 °C in phosphate buffered saline (PBS, pH 7.4). In comparison, the k_+ rate constant for Aβ40 under the same conditions is 3×10^5 M^{-1} s^{-1} and Aβ42 $k_+ = 3 \times 10^6$ M^{-1} s^{-1} [51,53]. The Aβ40/Aβ42 elongation rates are thus 100 to 1000-fold faster than for α-synuclein.

Monitoring early stages via ion mobility mass spectrometry (IM MS)

Thioflavin T fluorescence is not useful for monitoring the early steps in amyloid formation because they involve structural transitions that are invisible to ThT. However, a technique that can monitor early states of amyloid formation in a fast, sensitive manner is native ion mobility mass spectrometry IM-MS (Fig. 3).

The goal of native ion-mobility mass spectrometry (IM-MS) is to analyze protein and protein complexes in the gas phase while preserving protein-protein interaction and protein structures in a native-like state. Native ion mobility mass spectrometry allows one to analyze protein mass (m/z) and conformational state of proteins and protein complexes[54].
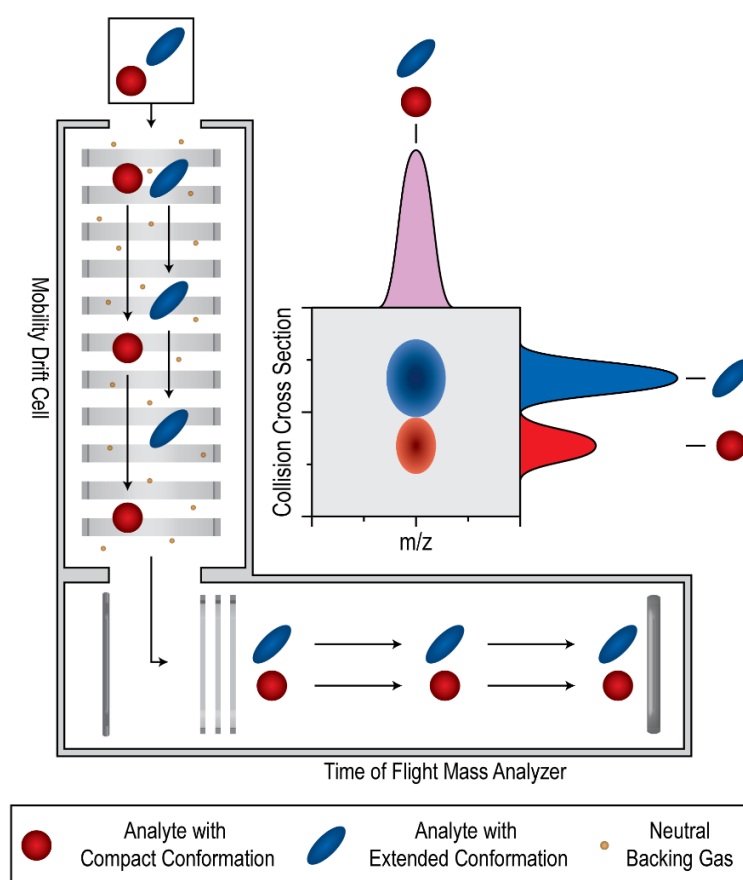
Figure 4: Diagram of an ion mobility-mass spectrometer (IM-MS).
First, proteins are ionized by nano-electrospray ionization (nESI) at the ion source. The generated ions traverse an ion guide (drift tube) filled with neutral gas molecules under the influence of a weak electric field. Ions in the drift tube migrate based on their size. Following the ion mobility separation, the ions are injected into a Time of Flight (TOF) mass analyzer to determine the mass-to-charge ratio m/z. IM-MS results in three-dimensional data output containing the ion intensity, size (collision cross section) and mass information (Figure was kindly provided by Dr. Varun V. Gadkari, University of Michigan).

To perform IM-MS, samples are ionized by nano-electrospray ionization (nESI) and separated via ion mobility (IM)[55]. In the ion mobility step, ions traverse through a neutral drift gas (e.g. argon gas) in the presence of a weak electric field. Ions are separate based on their orientationally averaged collision cross section (CCS) and charge. Each ion generated during ionization (nESI) has a unique drift time and arrival time distribution based on its transfer time through the drift tube, and its mass-to-charge ratio (m/z) based on its flight time through the time of flight mass spectrometer[56].

The collision cross section is a direct measure of physical size and shape of the separated ions. It has been established that the experimentally determined collision cross section for protein structures corresponded well with the CCSs estimated based on the published atomic structures[57–59]. An advantage of IM-MS is that it allows for the very sensitive detection of complexes on a millisecond time scale and has the ability to measure appearance and disappearance of individual species during a reaction.

Previously, native ion mobility mass spectrometry has been used to investigate the ensemble of amyloid peptides because of its ability to elucidate conformational heterogeneity of samples and because of its ability characterize protein-protein interactions[60]. IM-MS has previously been used to characterize small oligomers formed by Aβ40 and Aβ42[60]. It was found that Aβ42 can form dimer, tetramer, hexameric and dodecameric states[61]. In all cases the oligomeric species did not represent more than 10 % of the total signal, indicating that these states are all in equilibrium with each other. In contrast to Aβ42, only dimers and trimers of Aβ40 were detected.

The characterization of intrinsically disordered proteins (IDPs) is an inherently challenging problem. However, a number of studies with intrinsically disordered proteins have shown that IM-MS is capable of differentiating the conformational state of disordered proteins alone and in complex making this a promising approach to analyzing amyloid formation which is known to involve transitions from an intrinsically disordered state of an amyloid protein to a much more ordered state of the amyloid[62,63].

1.4   Molecular Chaperones are modifiers of amyloid formation

One of the goals of this thesis is to understand how host factors that alter amyloid formation affect the mechanism of amyloid formation. Disease associated mutations in Aβ40/42 or α-synuclein alter the propensity and kinetics of amyloid formation[34,47]. These intrinsic factors

have been associated to cases of early on-set AD or PD. A study of Aβ42 (e.g. E22G) mutants associated with early on-set AD found that mutants that reduce the net charge of Aβ42 accelerate the step of secondary nucleation[47]. External factors that can inhibit or modify amyloid formation are of interest in developing treatments for AD and PD and a further understanding of the process.

Molecular chaperones can affect the three steps of amyloid formation: primary nucleation, secondary nucleation, and elongation. Molecular chaperones have evolved to be promiscuous in recognizing misfolded or aggregates proteins, therefore they are well positioned to bind to different folding states that occur during amyloid formation[9]. Chaperone binding can potentially affect various microscopic steps of amyloid formation with their effect dependent on the relative affinities of the chaperone towards different species in the amyloid formation pathway[64]. The conserved chaperones Hsp70 and Hsp90 are known to inhibit early stages of Aβ42 amyloid formation[65]. Hsp70 and its co-chaperone Hsp40 interact with misfolded monomers or oligomers affecting different steps occurring during amyloid formation[65]. Hsp70 can function as a holdase, that binds to misfolded states and blocks the progression of amyloid formation. Hsp90 has been shown to interact with the amyloid-prone repeat motif in tau and thus act as a holdase in preventing amyloid aggregation[66,67].

The Hsp40 molecular chaperone DNAJB6 inhibits Aβ42 amyloid formation at sub-stoichiometric concentrations. DNAJB6 binds to small oligomeric nuclei rather than monomers and in doing so inhibits primary nucleation[68]. Members of the BRICHOS domain family have been reported to inhibit amyloid formation[69]. A recent publication studied the mechanism by which BRICHOS Bri2 inhibits Aβ42 amyloid formation in detail and found that Bri2 selectively inhibits the step of secondary nucleation[70]. The molecular chaperone Hsp104, a AAA-ATPase, is a molecular machine that can disaggregate proteins and amyloids[71,72]. Hsp104 is not present in metazoans, instead a protein-disaggregase machinery is present that consist of a complex of chaperone proteins Hsp110, Hsp70 and Hsp40[73]. Specifically, it has been shown that a complex containing Hsp70 (Hsc70) the J-protein DANJB1 and a nucleotide exchange factor Apg2 can disaggregate α-synuclein fibrils in vitro[74]. The disaggregated protein can be targeted for degradation by the proteasome.

Another class of proteins that have been found to influence amyloid formation are antibodies generated against the disordered or oligomeric state of amyloid protein[75]. A rational design approach generated antibodies effective in targeting primary or secondary nucleation of Aβ42[76]. Similarly, a protein design approach has generated a different binding protein that

targets α-synuclein aggregation[77]. The use of antibodies in clinical trials however is very challenging due to severe side effects including host immune and inflammatory responses[78]. However, the autoantibody Aducanumab, that was derived from elderly people who are cognitively normal and fit has shown some promise in clinical trials in targeting amyloid-β aggregation. Aducanumab appears to cause less severe side effects in comparison to previously tested anybodies[79].

Poly-anions including polyphosphate and heparin are another class of molecules that can modify amyloid formation. The oligomer hypothesis states that the intermediate oligomeric species are more harmful to the cell than the final insoluble amyloid fibrils[80,81]. Poly-anions seem to work by targeting oligomers, reduce them in number by accelerating amyloid kinetics and favoring the amyloid fibril state[82]. It has been demonstrated that polyphosphate can protect non-amyloid proteins from aggregation by keeping them in a β-sheet like structure[83]. Polyphosphate can accelerate the formation of multiple amyloid proteins (e.g. α-synuclein, Aβ42, tau). Polyphosphate binds to amyloid fibrils and thereby changes the morphology of the fibrils[84]. The positively charged molecule, heparin, has also been reported to accelerate the formation of amyloid fibrils[85]. This short overview shows the diversity and complexity of different modifiers of amyloid formation in vitro and in vivo. I now wish to focus on a novel modifier of amyloid formation which is the subject of my thesis namely ScSERF the *S. cerevisiae* homologue to the *C. elegans* protein MOAG-4 (modifier of amyloid aggregation-4).

1.5 SERF/MOAG-4 is a novel modifier of amyloid formation

Pharmacological attempts to target proteins involved in amyloid formation such as the molecular chaperones discussed above or additional members of the proteostatsis network have been met with very limited success[86]. Therefore, the discovery of additional modifiers of amyloid formation is urgently needed to expand the range for possible drug targets.

Genetic screens are a useful tool to discover new genes involved in disease. Overexpression of aggregation-prone disease-related proteins (e.g. polyglutamine, α-synuclein and β-amyloid) fused to fluorescent reporter like YFP or GFP (yellow- or green-fluorescent protein) lead to foci formation and toxicity in the model system *Caenorhabditis elegans*. A genetic screen in *C. elegans* identified that the deletion of MOAG-4 reduced the protein aggregation and toxicity of polyglutamine, amyloid-β and α-synuclein[87]. Figure 5 A, B shows bright puncta of YFP-

protein fused to a polyglutamine stretch in an amyloid sensor, it was found that the deletion of MOAG-4 leads to a significant decrease of aggregated protein (Fig. 5 B). MOAG-4 is a very small highly evolutionary conserved protein (Fig. 6)[88]. In the same study the authors found a similar effect in HEK293 cells, in which the human homologues SERF1a, SERF2 deletion leads to less aggregation and a reduction in cell death (Fig. 5 C).
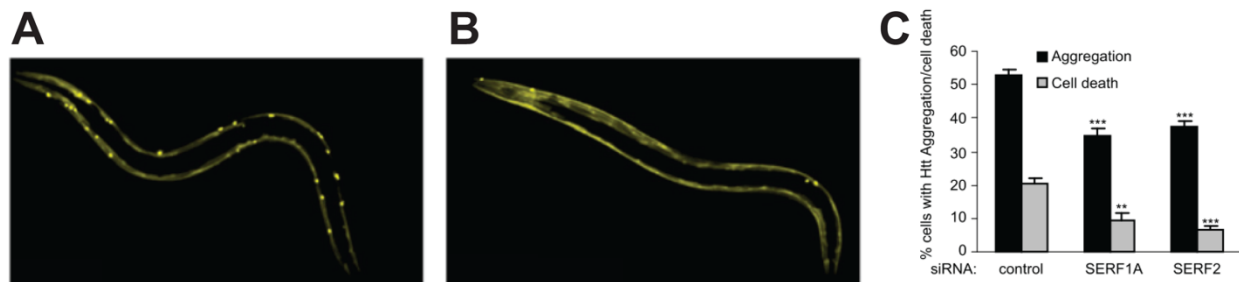
Figure 5: Genetic Screen for modifiers of amyloid formation.
(A) Confocal images of wild type *C. elegans* overexpressing YFP-Q40 protein show formation of abundant puncta. (B) Confocal images of an isogenic *C. elegans* with the gene *moag-4* deleted. (C) Overexpression of HA-tagged Huntington exon 1 with polyQ (Q74) extension, aggregation and cell death in HEK293 cells transiently transfected with siRNA targeting SERF1A or SERF2. Images modified from van Ham TJ, et al. (2010)[87].

Additionally, the overexpression of the human MOAG-4 homologue, a small EDRK-rich factor 1 (SERF1A and SERF2) increased the toxicity of polyglutamine (HTT exon 1 polyQ) expression in cell culture experiments[87].

A recent paper shows that in SH-SY5Y neuroblastoma cells where SERF1a and GFP-tagged α-synuclein were overexpressed together that SERF1a co-localizes to α-synuclein puncta, indicating a possible interaction between SERF1a and α-synuclein in vivo[89].

In vitro, the human protein SERF1a has been shown to be able to accelerate amyloid formation of a broad range of amyloidogenic proteins[90]. It has been shown that MOAG-4 is an intrinsically disordered protein in solution and that in vitro it is capable of accelerating amyloid formation of α-synuclein[91]. However, the detailed mechanism whereby MOAG-4 and its homologues accelerate amyloid formation is not yet clear. A very recent publication suggests that SERF1a is an RNA-binding and organizing protein. SERF1a can bind RNA molecules with low-micromolar affinity[92]. SERF1a sequence does not show any previously observed RNA-binding motifs, but the high isoelectric point of SERF1a (pI 10.44) is commonly observed in nucleic acid binding proteins. The function of the interaction between SERF1a and RNA is not clear[92].

In this study I am characterizing the SERF homologue from *S. cerevisiae*, YDL085C-A, hereafter termed ScSERF. A sequence alignment between members of the SERF/MOAG-

family shows the high degree of sequence conservation between ScSERF and other SERF proteins (Fig. 6). ScSERF sequence is 45 % identical to human SERF1a, and 49 % identical to *C. elegans* MOAG-4. The *S. cerevisiae* homolog was chosen not only for its sequence conservation but also due to ease of genetic manipulations and the availability of numerous genetic tools for this model organism. Future studies using the model organism yeast will help us bridge the gap between in vitro findings and in vivo questions.

Figure 6: Sequence alignment of ScSERF
Alignment of complete protein sequence of *S. cerevisiae* SERF (ScSERF) with representative homologues from a diverse selection of other eukaryotic species. The accession codes of the sequences selected from top to bottom are; Q3E7B7, Q9UTF0, O75920, P84101, Q32P76, Q9BKU8, Q9BKU8, A5JSS4, Q9VEW2, A6H8S3, A0A3Q2ULA2, P84102, F6Y2S0. (Figure from Meinen *et al.,* 2019).

1.6 Objectives of this thesis

As described in the introduction, an in-depth understanding of the mechanism and process of amyloid formation is crucial for the aim to develop intervention methods in treating devastating neurodegenerative diseases including Alzheimer's and Parkinson's.

The overall aim of this work is to characterize ScSERF, a small intrinsically disordered protein, in order to gain mechanistic and structural insights into how it accelerates amyloid formation of Aβ40 and α-synuclein. The small sizes and biophysical amenable characteristics of ScSERF, Aβ40 and α-synuclein present an excellent opportunity to study the mechanism of amyloid formation and how it is affected by this host factor in great detail.

The first aim is to characterize the structural features of ScSERF and compare them to the structural features of the previously characterized MOAG-4 and human SERF homologues.

For the second aim I set out to characterize the mechanism of Aβ40 and α-synuclein amyloid formation, this involved first establishing in our lab reproducible amyloid kinetics assays for these proteins. In the case of Aβ40, the kinetic framework developed the Knowles group [41] was utilized to analyze Aβ40 amyloid kinetics and to determine the microscopic steps that are effected by ScSERF. The amyloid kinetics of α-synuclein in the presence of ScSERF were established and were evaluated both under self-seeded and un-seeded conditions. Structural investigation of the interaction between ScSERF and the amyloid proteins will be performed by solution nuclear magnetic resonance spectroscopy (NMR) and the early kinetics of amyloid formation will be characterized using native ion mobility-mass spectrometry (IM-MS). The mechanistic insights generated from the kinetic data analysis were combined with the structural data to generate a comprehensive picture of the interaction between ScSERF and both amyloid proteins. I also set out to investigate if ScSERF exhibits any amyloid related phenotype(s) in *S. cerevisiae*. The SERF protein is highly conserved in eukaryotes, the advantage of working with ScSERF, the yeast homologue, is based on the diversity of genetic tools ability to easily manipulated *S. cerevisiae*. This will allow us to test our hypothesis derived from the in vitro characterization in vivo.

By investigating the described aspects, we will gain valuable information about the role a small intrinsically disordered protein on amyloid formation and generate knowledge that can potentially be applied towards targeting aspects of amyloid formation.

2 Materials

2.1 Chemicals, Equipment and Consumables

2.1.1 Chemicals

Chemical	Abbreviation	Supplier
1,2-dithiotherol	DTT	Sigma Aldrich, St .Louis, MO
2-Mercaptoethanol	βME	MP Biomedicals, Irvine, CA
Acetic acid, glacial		Mallinckrodt Baker, Philipsburg, NJ
Agarose		MP Biomedicals, Irvine, CA
Ammonium acetate		MP Biomedicals, Irvine, CA
Ammonium bicarbonate,	NH_4HCO_3	Sigma Aldrich, St. Louis, MO
Ammonium chloride, ^{15}N	NH_4Cl	Cambridge Isotope Laboratories, Inc. Andover, MA
Ammonium sulfate	$(NH_4)_2SO_4$	
Arabinose		MP Biomedicals, Irvine, CA
Bacto-Agar		Difco, Detroit, MI
Bromophenol blue		
Calcium chloride	$CaCl_2$	Thermo Fisher Scientific, Waltham, MA
Carbenicillin		Thermo Fisher Scientific, Waltham, MA
Chloroform		Sigma Aldrich, St. Louis, MO
Citric acid		Mallinckrodt Baker, Phillipsburg, NJ
Cobalt (II)-chloride	$CoCl_2$	Sigma Aldrich, St. Louis, MO
Coomassie Brilliant blue G250		MP Biomedicals, Irvine, CA
Coomassie Brilliant blue R250		MP Biomedicals, Irvine, CA
Copper (II)-sulfate	$CuSO_4$	Sigma Aldrich, St. Louis, MO
Dimethyl sulfoxide	DMSO	Sigma Aldrich, St. Louis, MO
Dipotassium hydrogen phosphate	K_2HPO_4	Thermo Fisher Scientific, Waltham, MA
Ethanol		Mallinckrodt Baker, Philipsburg ,NJ
Ethylenediamine tetra acetic acid	EDTA	Sigma Aldrich, St. Louis, MO
Glucose		MP Biomedicals, Irvine, CA
Glucose, ^{13}C		Cambridge Isotope Laboratories, Inc. Andover, MA
Glycerol		Thermo Fisher Scientific, Waltham, MA
Glycine		Sigma Aldrich, St. Louis, MO
Guanidinium chloride, ultra-pure	GdnHCl	Thermo Fischer Scientific, Waltham, MA
Hydrochloride acid	HCL	Thermo Fisher Scientific, Waltham, MA
Imidazole		Sigma Aldrich, St. Louis, MO
Iron (III)-chloride	$FeCl_3$	Sigma Aldrich, St. Louis, MO
Isopropanol		

Isopropyl β D-1-thiogalactopytanoside	IPTG	Research Products International, Mt. Prospect, Illinois
Magnesium chloride	$MgCl_2$	Sigma Aldrich, St. Louis, MO
Magnesium sulfate	$MgSO_4$	Sigma Aldrich, St. Louis, MO
Manganese (II) sulfate	$MnSO_4$	Sigma Aldrich, St. Louis, MO
2-(N-morpholino)ethanesulfonic acid	MES	Sigma Aldrich, St. Louis, MO
N-(2-hydroxyethyl)-piperazine-N'-2-ethan sulfonic acid	HEPES	MP Biomedicals, Irvine, CA
Nickel sulfate	$NiSO_4$	Sigma Aldrich, St. Louis, MO
Phenylmethylsulfonyl fluoride	PMSF	Sigma Aldrich, St. Louis, MO
Potassium chloride	KCl	Sigma Aldrich, St. Louis, MO
Potassium dihydrogen phosphate	KH_2PO_4	Sigma Aldrich, St. Louis, MO
Potassium hydroxide	KOH	Merck, Whitehouse Station, NNJ
Sodium chloride	NaCl	Thermo Fisher Scientific, Waltham, MA
Sodium dodecyl sulfate	SDS	Gibo, Rockville, MD
Sodium hydroxide	NaOH	Sigma Aldrich, St. Louis MO
Thiamine-hydrochloride		MP Biomedicals, Irvine CA
Thioflavin T	ThT	Sigma Aldrich, St. Louis MO
Tris-(hydroxymethyl)-aminomethan	Tris	MP Biomedicals, Irvine CA
Tris(2-carboxyethyl)phosphine	TCEP	Sigma Aldrich, St. Louis MO
Tryptone		Thermo Fisher Scientific, Waltham, MA
Urea, ultra-pure		MP Biomedicals, Irvine CA
Yeast extract		Thermo Fischer Scientific, Waltham, MA
Yeast Synthetic Drop-out Medium		Sigma Aldrich, St. Louis MO
Zinc sulfate	$ZnSO_4$	Sigma Aldrich, St. Louis MO

2.1.2 Antibiotics, markers and dyes

All antibiotics were purchased from MP Biomedicals, Irvine, CA.

Antibiotic	Solvent	Stock solution [mg/ml]	Working concentration [μg/ml]
Ampicillin	ddH_2O	200	200
Chloramphenicol	100 % Ethanol	34	34
Carbenicillin	ddH_2O	100	100
Kanamycin	ddH_2O	100	100

Marker/Dye	Company
PageRuler™ Prestained Protein Ladder	Fermentas, Burlington, Canada
QuickLoad 1kb DNA Ladder	New England Biolabs, Ipswich, MA
Bromophenol blue	MP Biomedicals, Irvine, CA
Coomassie brilliant blue R-250	MP Biomedicals, Irvine, CA
Gel Loading Dye, Blue (6x) for DNA	New England Biolabs, Ipswich, MA
SYBR Safe DNA Gel Stain	ApexBio, Houston, TX
AlexaFluor™ 532 NHS Ester (Succinimidyl Ester)	Thermo Fisher Scientific, Waltham, MA
AlexaFluor™ 532 C5 Maleimide	Thermo Fisher Scientific, Waltham, MA

2.1.3 Enzymes and Kits

All restrictions enzymes were purchased from New England Biolabs, Ipswich, MA.

Enzyme	Supplier
Benzonase nuclease	Sigma Aldrich, St.Louis, MO
Phusion High-Fidelity DNA Polymerase	New England Biolabs, Ipswich, MA.
GoTaq polymerase	Promega, Madison, WI
PfuUltra High-fidelity DNA Polymerase	Agilent Technologies, Santa Clara, CA

Kit	Supplier
QIAprep Spin Miniprep Kit	Qiagen, Valencia, CA
QIAquick Gel Extraction Kit	Qiagen, Valencia, CA
QIAquick PCR Purification Kit	Qiagen, Valencia, CA
QuickChange II Site-Directed Mutagenesis Kit	Stratagene, La Jolla, CA

2.1.4 Oligonucleotides, Plasmids and Strains

All oligonucleotides and synthetic genes were purchased from IDT, Integrated DNA technologies, Coralville, IA.

Primer	Sequence	Purpose
Forward A63C	5' GAAAAACTGGAAAAACTGAAATGTGAAAAAACCCGCCGCTAACTC 3'	ScSERF A63C
Reverse A63C	5' GAGTTAGCGGCGGGTTTTTTCACATTTCAGTTTTTCCAGTTTTTC 3'	ScSERF A63C
Forward L9W	5' CGGTAACCAGCGTGACTGGGCCCGTCAGAAAATC 3'	ScSERF L9W
Reverse L9W	5' GATTTTTCTGACGGGCCCAGTCACGCTGGTTACCG 3'	ScSERF L9W
FW YDL085C-A	5' GTCATGGATCCATGGCGCGCGGTAACCAGCG 3'	Cloning ScSERF pet28b
REV YDL085C-A	5' CATAGCTCGAGTTAACGGCGGGTTTTCTCCGCTTTC 3'	Cloning ScSERF pet28b
Forward Deletion Primer	5' ATGGCGCGCGGTAACCAGCG 3'	Deletion TCC codon for Serine in pet28b
Reverse Deletion Primer	5' TCCACCAATCTGTTCTCTGTG 3'	Deletion TCC codon in pet28b
YDL085C-A_mF1	5' AGAGCAACAAATTACGTCGCAAGACGATACATCTTTAACACGGATCCCCGGGTTAATTAA 3'	Genomic deletion in *S. cerevisiae*
YDL085C-A_mR1	5' ACTATTCATTCCAATAAAAGGACAGGTATAAAGTGTCTGCGAATTCGAGCTCGTTTAAAC 3'	Genomic deletion in *S. cerevisiae*

E. coli plasmid	Information	Reference
Pet28b-His-Sumo-ScSERF	T7, His-sumo tag	Meinen et al. (2019), this study
pFGET19_Ulp1	T7, His tag	Ming Lei, University of Michigan[93]
pETSaC-Aβ40	T7, Aβ40 overexpression	Walsh DM, et al. (2009, *FEBS J* 276(5):1266–1281.
pET7-7-α-synuclein vector	T7, α-synuclein overexpression	Jain N, et al. (2013) PLoS One 8(12):e83752

S. cerevisiae Plasmid	Information	Reference
pRS426 Gal1	Empty vector	Petroi D, et al. (2012). J Biol Chem 287(33):27567–27579.
pRS426 Gal1 alpha-Synuclein WT	Overexpression α-syn, Strong gal promoter	Petroi D, et al. (2012). J Biol Chem 287(33):27567–27579.
pRS426 Gal1 alpha-Synuclein A30P	Overexpression α-syn, Strong gal promoter	Petroi D, et al. (2012). J Biol Chem 287(33):27567–27579.
pRS426 Gal1 alpha-Synuclein E46K	Overexpression α-syn, Strong gal promoter	Petroi D, et al. (2012). J Biol Chem 287(33):27567–27579.
pRS426 Gal1 alpha-Synuclein A53T	Overexpression α-syn, Strong gal promoter	Petroi D, et al. (2012). J Biol Chem 287(33):27567–27579.
pRS426 Gal1 alpha-Synuclein WT Y125F	Overexpression α-syn, Strong gal promoter	Petroi D, et al. (2012). J Biol Chem 287(33):27567–27579.
pYES2 empty	Empty vector	Krobitsch S, Lindquist S (2000).Proc Natl Acad Sci U S A 97(4):1589–1594.
pYES2 Htt 103Q	Huntington Exon polyQ overexpression, strong gal promoter	Krobitsch S, Lindquist S (2000).Proc Natl Acad Sci U S A 97(4):1589–1594
pYES2 Htt 25QP	Huntington Exon polyQ overexpression, strong gal promoter	Krobitsch S, Lindquist S (2000).Proc Natl Acad Sci U S A 97(4):1589–1594

E. coli strains

Strain	Genotype	Reference / Supplier
E. coli K12 MG1655	*F- λ- ilvG rfb-50 rph-1*	Blattner, Plunkett, et. al.1997[94]
E. coli K12 NEB 10-beta	*Δ(ara-leu) 7697 araD139 fhuA ΔlacX74 galK16 galE15 e14- Φ80dlacZΔM15 recA1 relA1 endA1 nupG rpsL (StrR) rph spoT1 Δ(mrr-hsdRMS-mcrBC)*	New England Biolabs, Ipswich, MA
E. coli BL21 DE3	B F⁻ *ompT gal dcm lon hsdS_B(r_B⁻ m_B⁻)* λ(DE3 [*lacI lacUV5-T7p07 ind1 sam7 nin5*]) [*malB*⁺]_{K-12}(λ^S)	Merck&Co, Kenilworth, NJ

S. cerevisiae strains

Strain	Genotype	Reference
BY4742 S. cerevisiae	MATα *his3Δ1 leu2Δ0 lys2Δ0 ura3Δ0 trpΔ:HIS*	Baker, Brachmann C, et al. (1998) Yeast 14(2):115–132.
BY4742 S. cerevisiae Δydl085c-a	MATα *his3Δ1 leu2Δ0 lys2Δ0 ura3Δ0 trpΔ:HIS Δydl085c-a::KAN*	This study

2.1.5 Equipment

Equipment	Supplier
Chromatography	
AKTA*pure*^{TM}	GE Healthcare, Chicago, IL
Fraction Collector Frac 950	GE Healthcare, Chicago, IL
P1 Pump	GE Healthcare, Chicago, IL
HisTrap HP, 5ml CV	GE Healthcare, Chicago, IL
HiTrap SP, 5ml CV	GE Healthcare, #17115201, Chicago, IL
HiTrap Q HP, 5ml CV	GE Healthcare, #17115401, Chicago, IL
DEAE cellulose resin	GE Healthcare, Chicago, IL
Superdex S75 10/300 GL	GE Healthcare, #17517401, Chicago, IL
HiLoad 16/60 Superdex S75	GE Healthcare, #17106801, Chicago, IL
PD10 desalting column	GE Healthcare, Chicago, IL
Gelelectrophorese	
Electrophoresis Power Supply EPS 301	Amersham Pharamcia Biotech
Agarose Gel Chamber FB-SB-71	Amersham Pharamcia Biotech
XCell SureLock Mini-Cell	Thermo Fischer Scientific, Waltham, MA
Scanner, EPSON Expression 1680	Epson, Long Beach, Ca
ChemiDoc^{TM} MP Imaging system	BioRad, Hercules, CA
Molecular biology	
Venti 96-well Thermo Cycler	Applied BioSystems
New Brunswick^{TM} Innova 44 Incubator shaker	Eppendorf, Hamburg, Germany
New Brunswick^{TM} Innova 4230 Incubator shaker	Eppendorf, Hamburg, Germany
New Brunswick^{TM} Roller drum TC-7	Eppendorf, Hamburg, Germany
Eppendorf Thermomixer comfort	Eppendorf, Hamburg, Germany
Plate reader	
Tecan Infinite M200 pro Microplate reader	Tecan, Maennedorf, Switzerland
Tecan Infinite M1000 Microplate reader	Tecan, Maennedorf, Switzerland
Synergy HTX Multi-Mode Microplte reader	Agilent Technologies, Santa Clara, CA
Spectroscopy	
UV/Vis Spectrometer UV-1900	Shimaduz, Kyoto, Japan
Cary 100 UV-Visible Spectrophotometer	Agilent Technologies, Santa Clara, CA
Cary Eclipse Fluorescence Spectrophotometer	Agilent Technologies, Santa Clara, CA
J-1500 CD Spectrometer	JASCO Inc.
Genesis 10vis	Thermo Scientific, Waltham, MA
Mass Spectrometry	
Synapt G2 mass spectrophotometer	Waters, Milford, MA
NMR Spectroscopy	
Bruker AVANCE^{TM} 900 Mhz	Bruker, Billerica, MA
Bruker Ascend^{TM} 800 Mhz	Bruker, Billerica, MA
Centrifugation	

Avanti J26XPI	Beckman Coulter, Brea, CA
ProteomeLab^{TM} XL-1	Beckman Coulter, Brea, CA
Beckman Coulter Microfuge 20R	Beckman Coulter, Brea, CA
Eppendorf centrifuge 5415R	Eppendorf, Hamburg, Germany
Eppendorf centrifuge 5424	Eppendorf, Hamburg, Germany
Eppendorf centrifuge 5810 R	Eppendorf, Hamburg, Germany
Others	
Sonication bath, , #1510	Branson Ultrasonics, Danbury, CT
Mettler Toledo Classic Light	Mettler Toledo, Columbus, OH
Mettler Toledo Eccellence	Mettler Toledo, Columbus, OH
pH Meter Fischer Scientific XL15	Thermo Fischer Scientific, Waltham, MA
Multichannel pipette 10, 200, 1000	Eppendorf, Hamburg, Germany
Pipettes, Research, 2,10,100, 200, 1000 µl	Eppendorf, Gilson
Vortex mixer	Thermo Fischer Scientific, Waltham, MA
Vortex Genie2	Scientific Industries
Water purification system MilliQ	MilliporeSigma, Burlington, MA
Thermo Mixer	Eppendorf, Hamburg, Germany
Heating Block, IsoTherm	Fisher Scientific, Waltham, MA
Stir plate PC-353	Corning Life Sciences, Lowell, MA
Stir plate PC-420D	Corning Life Sciences, Lowell, MA

2.1.6 Consumables

Consumable	Supplier
Adhesive sealing sheet #125434	Thermo Scientific, Waltham, MA
Amicon® Ultra, 2 ml,4 ml,15ml	Millipore, Billerica, MA
Corstar 3370 Clear Polystrene 96-well plate	Corning Life Sciences, Lowell, MA
Corstar 3631 black, clear bottom 96-well	Corning Life Sciences, Lowell, MA
Corstar 3881 half-well, clear bottom 96-well	Corning Life Sciences, Lowell, MA
Culture tubes 18 x 150 mm	Thermo Fischer Scientific, Waltham, MA
Dialysis membrane	Spectrum Laboratories Inc
Disposable plastic cuvettes	Thermo Fisher Scientific, Waltham, MA
Electrode Buffer Solutions pH 4.0, 7.0, 10.0	Thermo Fisher Scientific, Waltham, MA
Eppendorf® LoBind microcentrifuge tubes,	Eppendorf, Hamburg, Germany
Falcon, Polypropylene tube 15 ml & 50 ml	Thermo Fisher Scientific, Waltham, MA
Genepulser cuvettes	BioRad, Hercules, CA
Microfuge tube 1.5 ml & 2 ml	Thermo Fischer Scientific, Waltham, MA
NuPAGE^{TM} 16%Tricine	Invitrogen, Carlsbad, CA
NuPAGE^{TM} 4-12% Bis Tris Gel	Invitrogen, Carlsbad, CA
Petri dishes	Thermo Fisher Scientific, Waltham, MA
Syringe filters, sterile, 0.22 µm, 0,4 µm	Millipore, Billerica, MA
Thermowell PCR tube	Corning Life Sciences, Lowell, MA

2.1.7 Software

Software	Source
Molecular biology	PrimerX (Bioinformatics.org), SerialCloner (SerialBasic)
Plotting and graphing	Origin Pro (Origin Lab), KaleidaGraph (Synergy), GraphPad (GraphPad Software, Inc), Adobe Illustrator, Adobe Photoshop
Analytical Ultracentrifugation	UltraScanIII, SedFit
NMR Spectroscopy	TopSpin, NMRPipe, Sparky, Pymol, CSRossetta
IM-MS	MassLynx (Waters), TWIMExtract [95], CIUSuite2 [96].
Amyloid kinetics, simulation	AmyloFit, BerkleyMadonna

2.2 Culture media

Solid media was prepared by adding 1.5 % (w/v) agar to the liquid media prior to autoclaving. Culture plates were poured and cooled at room temperature. The solidified plates were stored at 4 °C.

Media	Composition
Lysogenic broth (LB) Media	10 g/l Tryptone, 5 g/l Yeast extract, 5 g/l NaCl
PEM media	12 g/l Tryptone, 2.5 g/l Yeast extract, 4 ml/l Glycerol, 0.017 M KH_2PO_4, 0.072 M K_2HPO_4
SOC medium	10 g/l Tryptone, 2.5 g/l Yeast extract, 10 mM NaCl, 2.5 mM KCl, 10 mM $MgCl_2$, 10 mM $MgSO_4$, 20 mM Glucose
YPD Media	10 g/l Bacto-yeast extract, 20 g/l Bacto-peptone, 20 g/l Glucose
SC drop out media	Bacto-yeast nitrogen base without amino acids 6.7 g/l, Glucose 20 g/l, Dropout media 2 g/l
Synthetic Dextrose media (SD)	Bacto-yeast nitrogen base without amino acids 6.7 g/l, Glucose 20 g/l
M9-Minimal Media for NMR	Na_2HPO_4 (dibasic) 6g/l, KH_2PO_4 (Monobasic) 3 g/l, ^{13}C Glucose 4 g/l, ^{15}N NH_4Cl 1 g/l, 4 mM $MgSO_4$, vitamin mix (1000x), trace elements (100x)
Trace elements (100x)	EDTA 5g/l, $MnCl_2$ 1,6 g/l, FeCl3 0.8 g/l, $ZnCl_2$ 0.05 g/l, $CuCl_2$,0.01 g/l,$CoCl_2$ 0.01 g/l, H_3BO_3 0.01 g/l, Ni_2SO_4 0.01g/l, Sodium molybdate 0.01 g/l, pH 7.0 with NaOH
Vitamin mix (1000x)	Riboflavin 1g/l, Niacinamide 1g/l, Pyridoxine monohydrate 1g/l, Thiamine 1g/l

2.3 Buffers

Here listed are standard buffers used for routine techniques. Solutions used for other experiments are specified in the corresponding method section.

Buffer	Composition
Agarose electrophoresis	
TAE Buffer	Tris-HCl 24.2 g/l, Acetic acid 5.7 ml/l, 0.5 mM EDTA, pH 7.5
Agarose gel	1 % Agarose, 0.05 µl/ml SYBR-safe dye, in TAE Buffer
SDS- Polyacrylamide-Gel Electrophoresis	
5 x reducing SDS loading dye:	Sodium dodecyl sulfate 5g Glycerol 30.5 g Tris (1M), pH 7.0 15 ml bromophenol blue 0.025 g β-mercaptoethanol 2.5 ml ddH$_2$O add 50 ml
SDS-MES Buffer	50 mM MES, 50 mM Tris-HCl, 0.1 % SDS, 1 mM EDTA, pH 7.3
Tris-Tricine-SDS-Buffers: Anode Buffer (10x)	1 M Tris-HCl, pH 9.0
Cathode Buffer (10x)	1 M Tris-HCl, 1 M Tricine, 1 % SDS, pH 9.25
Yeast Transformation Buffer	
LioAC Buffer	0.1 M LioAC, 0.2 M Tris-HCl pH 8, 1 mM EDTA
TE Buffer (10x)	10 mM EDTA, 0.1 M Tris-HCl pH 8
PEG solution	50 g/ml PEG 3350, 1x TE buffer, 0.1 M LioAC
Solution for Coomassie staining	
Fairbanks solution A	25 % (v/v) Isopropanol, 10 % (v/v) Acetic acid, 0.05 % Coomassie R 250
Fairbanks solution B	10 % (v/v) Isopropanol, 10 % (v/v) Acetic acid, 0.005 % Coomassie R 250
Fairbanks solution C	10 % (v/v) Acetic acid, 0.002 % Coomassie R 250
Fairbanks solution D	10 % (v/v) Acetic acid

3   Methods

Some aspects of the method section have been previously published in Meinen et al. (2019)[97]. Standard solutions are listed in the material section. All other buffers and material are described in the respective methods.

3.1   Microbiology

3.1.1   Preparation and transformation of chemically competent *E. coli*

Chemically competent *E. coli* cells were prepared following the calcium-phosphate precipitation protocol by Nakta et al.[98] . In brief, a single colony of the desired *E .coli* strain was grown overnight in 5 ml LB media and diluted in 50 ml of LB media to a starting OD_{600} of 0.1. The cells were grown till mid-log phase at 37 °C (typically 3-4 h). The cells were harvested by centrifugation at 2,500 x g, 4 °C for 10 min. The bacteria pellet was solubilized in 5 ml ice-cold 0.1 M $CaCl_2$ solution and incubated for 30 min on ice. Cells were pelleted at 2,500 x g, 4 °C for 10 min and the pellet resuspend in 0.1M $CaCl_2$, 10% (v/v) glycerol solution. Aliquots of 50 μl of the suspension were flash frozen in liquid nitrogen and stored a -80 °C. For transformation a cell aliquot was thawed on ice and 0.5-3 ng of plasmid DNA was added and incubated on ice for 30 min. DNA uptake was facilitated by heat shock for 90 seconds in a 42 °C water bath. The cells were chilled on ice for 5 min and 900 μl of SOC medium was added to the cells. The cells were incubated at 37 °C for 1 h and plated in appropriate dilutions on selective media.

3.1.2   High-Efficiency Yeast Transformation

Yeast strains and plasmids used in this study are listed in above (Materials 2.1.4). Yeast transformation were performed following the standard lithium acetate method[99]. In brief, 5 ml YPD media or selective SD media was inoculated with a single colony and cultured overnight at 30 °C. 50 ml of media was inoculated with a starting OD_{600} of 0.1 from the overnight culture and grown till the OD_{600} 0.4-0.6 at 30 °C. The cells were pelleted at 2500 x g. Cells were resuspended in 10 ml of 1 x LiOAC buffer and centrifuged again at 3000 x g for 3 min. The pelleted cells were resuspended in 1 ml of 1 x LiOAC buffer. In a 1.5 ml tube 10 μl of 10 mg/ml salmon sperm DNA, 100 μl of cells and 1-5 μg of plasmid DNA (usually 5 μl) were mixed. 280 μl of PEG solution was added and vortexed. The mixture was incubated for 45 min at room temperature, 43 μl of DMSO was added and mixed. The cells were incubated for 10 min in a water bath at 42 °C and immediately chilled on ice. The cells were centrifuged for 2 min at

5000 rpm in microcentrifuge (Eppendorf) and the liquid was taken off. The pellet was resuspended in 100 μl of YPD and cells were plated onto appropriate selective plates. Plates were incubated for 2-3 days at 30 °C.

3.1.3 Isolation of DNA from *E. coli* cells and DNA concentration determination

Plasmid DNA from overnight cultures was isolated following the manufacturer's instructions for the used QIAprep Spin Miniprep Kit. Plasmid DNA was eluted in ddH$_2$O. To determine DNA concentration the absorbance was measured at 260 nm and concentration was calculated using Lambert-Beer law. Absorbance was measured using a NanoDrop™ ND-1000 Spectrophotometer (Thermo Fischer Scientific). DNA and Plasmids were stored at -20 °C.

3.1.4 Yeast survival assay

Spot titers test were performed to determine the survival of *Saccharomyces cerevisiae* that overexpress polyQ or α-synuclein. The overexpression of theses amyloid proteins leads to cytotoxic aggregation, that can be monitored by cell death on solid media. The α-synuclein assay has been described here [100], and the polyQ assay was shown here [101]. In brief, S. cerevisiae was grown in SC-Ura media containing 2 % raffinose and 0.1 % glucose till mid log phase and normalized to equal densities. The cells were serially diluted with a starting OD$_{600}$ of 5 and spotted on SC-Ura plates containing either 2 % glucose or 2 % galactose and incubated at 30 °C. Images of the plates were taken after 3 days of incubation time.

3.2 Molecular Biology

3.2.1 ScSERF plasmid construction

The amino acid sequence of the *S. cerevisiae* SERF protein (ScSERF), previously known as YDL085C-A (Uniref Q3E7B7), was codon optimized for protein expression in *Escherichia coli*, and the corresponding DNA sequence was synthesized using the tool and service provided by Integrated DNA Technologies. The synthesized DNA was cloned into a derivative of the pET28 vector (provided by the Ming Lei lab at the University of Michigan) using the restriction enzymes BamHI and XhoI[93].

The SUMO protease ULP1 recognizes the tertiary structure of the SUMO domain and cleaves the in the C-terminal motif X-G-G-X after the second glycine. After cloning the serine

following the second glycine in X-G-G-S was deleted by site-directed mutagenesis, resulting in X-G-G-M. This step made sure that the purified protein contains no additional residues. The pET28 vector contains a N-terminus 6-His-SUMO tag fusion[93]. This vector was constructed to enable the simple and scar less removal of the His-SUMO tag by ubiquitin-like-specific protease 1 (ULP1).

3.2.2 Polymerase chain reaction techniques (PCR)

PCR was used to amplify DNA sequences of interest. A thermostable DNA polymerase (Phusion, Pfu Turbo polymerase, Taq polymerase) in the presence of dNTPS and site-specific primers is used to amplify the desired DNA fragment.

Typical 50 µl reaction set up for Pfu Turbo polymerase:
Buffer, 10x	5 µl
Template DNA	5-50 ng
dNTPS	100 µM
Primers	0.5 µM
Pfu Turbo Polymerase	2.5 – 5 Units
ddH$_2$O	add 50 µl

Typical PCR protocol for Pfu Turbo polymerase:

Cycle step	Temperature	Time	Number of cycles
Initial denaturation	98 °C	30 s	1
Denaturation	98 °C	30 s	
Annealing	Various °C	1 min	25-35
Extension	72 °C	30 s/kb	
Final extension	72 °C	10 min	1

3.2.3 Colony PCR

Colony PCR was performed to identify correct colonies obtained after ligation and transformation. Colony PCR was performed using GoTaq polymerase (GoTaq, Promega M7123). *E. coli* colonies were picked and added to the reaction. *S. cerevisiae* gDNA was prepared using the Wizard Genomic Purification Kit (Promega), following the manufacture instructions.

Typical reaction set up for 30 µl reaction:

GoTaq Green. Master Mix, 2x	15 µl
Forward primer, 10 µM	3 µl
Reverse primer, 10 µM	3 µl
DNA-template	1x colony or 1 µl gDNA
ddH$_2$O	add 30 µl

PCR program for GoTaq

Cycle step	Temperature	Time	Number of cycles
Initial denaturation	95 °C	10 min	1
Denaturation	95 °C	45 s	
Annealing	58 °C	1 min	30
Extension	68 °C	1 min/kb	
Final extension	68 °C	10 min	1

3.2.4 Site-directed mutagenesis PCR

Site-directed mutagenesis was used to introduce point mutations in ScSERF using site-directed mutagenesis with a QuickChange Kit (Agilent). Overlapping primers introducing the desired change to the plasmid (e.g. mutation, insertion or deletion) were designed and used to amplify the plasmid by PCR. The PCR product is a doubly-nicked plasmid. The non-mutated starting plasmid is methylated and can be digested with DpnI, an endonuclease targeting only methylated DNA. The doubly-nicked mutated plasmid is transformed into *E. coli.*

Primers were designed using PrimerX (https://www.bioinformatics.org/primerx/cgi-bin/DNA_1.cgi). The primers of a desired length N are built to follow the following formula:

$T_m = 81.5 + 0.41(\%GC) - (675/N) - \%\text{mismatch}$

Where T_m is the melting temperature, N= length of the primer.

A typical 50 µl reaction was set up like this:

Reaction buffer, 10x	5 µl
dsDNA template	5-50 ng
Primer 1	125 ng
Primer 2	125 ng
dNTP mix	1 µl
NEB Phusion polymerase	0.5 µl

The PCR program was the following:

Cycle step	Temperature	Time	Number of cycles
Initial denaturation	98 °C	30 s	1
Denaturation	98 °C	30 s	
Annealing	55 °C	1 min	15
Extension	72 °C	1 min/kb	
Final extension	72 °C	10 min	1

3.2.5 Construction of *S. cerevisiae* ΔYDL085C-A strain

To delete the open-reading frame of YDL085C-A primers encoding homologous regions homologous to the start and end of the ORF and regions annealing to the KAN antibiotic cassette, that will replace the gene, were designed. The KAN cassette was amplified from the vector pFA6a KAN MX6 (provided by Amy Chang at the University of Michigan) by PCR. The linear PCR fragment was purified from an agarose gel and transformed into yeast following the high-efficiency yeast transformation described[99]. Colonies were picked and analyzed by colony PCR.

3.2.6 Agarose gel electrophoresis

DNA from restriction digestion or linearized DNA fragments from PCR were analyzed via agarose gel electrophoresis. 1 g of agarose was dissolved in 100 ml TAE buffer. 10 µl of SYBR Safe DNA Gel Stain (ApexBio #A8743) were added and the solution was poured into a running chamber and cooled till the agar solidified. DNA samples were mixed with 5 x fold DNA loading dye and loaded onto the agarose gel. Agarose gel electrophoresis was performed at 120 V in TAE buffer. The gels were visualized under ultra violet (UV) light using a ChemiDoc® Imaging system (BioRAD).

3.2.7 DNA sequencing

Constructed strains and plasmids were sequenced using GenScript or Genwiz services. DNA for sequencing was aliquoted at 10 µl and submitted. In some case samples were sent along with specific primers in other cases primers available in the standard library were used. Sequencing results were checked for desired sequence and unintended mutations.

3.3 Protein biochemistry

3.3.1 SDS-Polyacrylamide gel electrophoresis (SDS-PAGE) and staining

Protein separation based on their molecular weight can be achieved by sodium dodecyl sulfate-polyacrylamide gel electrophoresis. Therefore, proteins are denatured by high heat in SDS-detergent containing buffer. 5-fold reducing SDS loading buffer was added to protein samples and the samples were boiled at 95 °C for 5 min.

For small proteins Novex™ 16% Tricine protein gels (Thermo Fisher #EC66955) and for larger proteins and cell extract 4-12% NuPage™ Bis-Tris gels (Thermo Fischer #NP0324BOX) were used. Gel electrophoresis was performed in gel chambers (Thermo Fischer #A25977). Bis-Tris gels were run in SDS-MES Buffer. Tricine PAGE was run using cathode buffer in the upper tank and anode buffer in the lower tank. Gel chambers were placed in a box filled with ice to avoid overheating. Pages were run between 125 – 200 V for 45 min to 3 h, depending on the gel.

Fairbanks staining method was used to fix and stain protein on the SDS-PAGE[102]. The PAGE was stained in Fairbanks A by first microwaving for 30-60 s and staining for 30 min. The destaining process took place in Fairbanks C for 1 h and Fairbanks D for 2–16 h until the PAGE was completely destained. The PAGE was imaged with the BioRAD (ChemiDoc Imaging system).

3.3.2 Separation of insoluble amyloid fibrils form soluble protein

The soluble and insoluble fractions were separated by 60 min centrifugation at 20,000 x g using a Beckmann Microfuge 20R. The insoluble fraction was washed once in assay buffer.

5 x reducing SDS loading was added to all samples. 10 μl samples were then run on an Invitrogen Novex 16% Tricine Protein Gel followed by Fairbanks Coomassie blue staining

3.3.3 Determination of protein concentration

Protein concentrations were determined spectroscopically using a UV/Vis Spectrophotometer. The spectra were buffer-corrected. The extinction coefficient were determined as described here[103] and matched the ones used in the literature[51,104,105]. The concentration was calculated using Lambert-Beer's law.

$$E_\lambda = -\log\left(\frac{I_1}{I_0}\right) = \varepsilon\, c\, d$$

E_λ is the extinction at the wavelength λ, I_0 is the intensity of incoming light and I_1 is the intensity of the transmitted light, ε is the molar extinction coefficient (M^{-1} cm^{-1}), d is the optical path length (cm) and c is the concentration of the attenuating species.

The used absorption coefficients for proteins in this study:

Protein	Extinction coefficient ($M^{-1}cm^{-1}$) at 280 nm
ScSERF L9W	5500
Aβ40	1490
α-synuclein	5960

ScSERF's protein sequence contains no aromatic protein residues and therefore has no signal at 280 nm. The concentration was determinate by BCA-Assay using the tryptophan mutant ScSERF L9W.

3.3.4   Concentration determination using BCA-Assay

Pierce^{TM} BCA (Bicinchoninic acid) protein assay (Thermo Scientific # 23225) to determine ScSERF concentration was used according to manufacturer's instruction (Thermo Scientific). BCA assay is based on the Biuret reaction, the reduction of Cu^{+2} to Cu^{+1} by protein in alkaline medium. The purple colored reaction product is formed by two molecules of BCA chelating one cuprous ion. The soluble reaction product absorbs strongly at 562 nm.

The protein concentration of ScSERF L9W was determined as described above. A standard curve in the range of 20 to 2000 μg/ml ScSERF was prepared. Multiple dilutions of ScSERF were made. 25 μl of sample was added to 200 μl of BCA working reagent (WR) in a microtiter plate (Corning 96 Well Clear Flat Bottom #3370). The plate was incubated at 37 °C for 30 min and cooled to RT for 10 min, the absorbance was measured at 562 nm using a Tecan M200 pro plate reader. The ScSERF L9W samples were blank corrected and plotted resulting in a standard curve (Fig. 7). The curve was fitted to a linear regression (y = a + bX) and the concentration of ScSERF was determined by using the dilutions in the linear range of the standard curve.
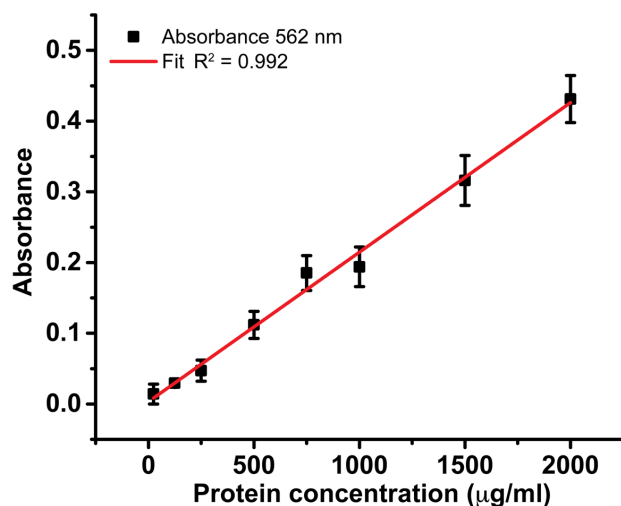
Figure 7: Calibration curve used to determine protein concentration via BCA assay.
Example of calibration curve, plotted is the absorbance of three technical replicates at λ = 562 nm. The calibration curve was fitted with a linear equation y = a + bX.

3.3.5 Protein concentration by ultra-centrifuge filters

Protein was concentrated using Amicon® Ultra centrifugal filters (Millipore) a cutoff of MWCO 3,500 Da was used, different sizes of Amicon® Ultra from 0.4 ml to 15 ml were used depending on the volume, that was concentrated. The membrane was washed with one volume of ddH$_2$O and equilibrated with the desired sample buffer before loading the diluted protein sample. Centrifugation was performed at 3000 x g in a pre-cooled 4 °C benchtop centrifuge (Eppendorf 5415R).

3.3.6 Protein production in M9 minimal media

The production of isotopic labeled ScSERF and Aβ40 protein for NMR spectroscopy was achieved by growing the *E. coli* strain containing the expression plasmids in minimal media containing ^{15}N NH$_4$Cl as the only nitrogen source and ^{13}C Glucose as the only carbon source. Single colonies were picked form a LB-Agar plate and were grown overnight in 5 ml LB-Media and the appropriate antibiotic. The culture was diluted at an OD$_{600}$ 0.1 into 5 ml M9 minimal media grown for 8 h. Cells were transferred into 25 ml M9 minimal media cultures and grown overnight. This overnight culture was used to inoculate 1 l culture flasks containing M9 media with the relevant isotopic labeled ^{15}N nitrogen and or ^{13}C carbon sources.

3.3.7   ULP 1 purification

The ULP1 containing vector pFGET19_Ulp1-Vector was transformed into *E. coli* BL21 cells. A single colony was picked and 10 ml of overnight culture was started and then it was used to inoculate 6 x 1 l PEM media. The cultures were grown till mid-log phase and shifted to 24 °C. Protein production was induced by addition of a final concentration of 0.1 mM isopropyl-β-D-1-thiogalactopyranoside (IPTG). The cells were harvested the next morning. Cells were pelleted by centrifugation 5000 x g, 20 min, 4 °C. The cell pellet was resuspended in lysis buffer (40 mM Tris, 10 mM NaH_2PO_4, 10% Glycerol, 10 mM Imidazole, pH 8) with 2 tablets of protease inhibitor cocktail (complete mini EDTA-free, Roche #5056489001), 10 μl Benzonase and 100 μl $MgCl_2$ (1 M stock solution). Cells were lysate by french press in two cycles at 1300 psi. The lysate was centrifuged for 30 min at 36,000 x g (4 °C). The lysate was filtered and loaded on a 5 ml HisTrap (GE healthcare #17-5248-02) column. The column was washed with 10 CV of lysis buffer containing 20 mM imidazole. The protein was eluted with lysis buffer containing 500 mM imidazole. Elution fractions were analyzed by SDS-PAGE and the pure elution fractions were pooled concentrated, aliquoted and stored at -80 °C.

3.3.8   Purification of ScSERF

The pET28b-ScSERF plasmid constructed as described before was transformed into *E. coli* BL21 (DE3) cells for protein expression. Cells were grown with shaking at 180 rpm at 37 °C to early log phase in PEM media, that contained 100 μg/ml kanamycin and then shifted to 20 °C. ScSERF expression was then induced by addition of 0.1 mM IPTG. After 16 h of expression, cells were pelleted by centrifugation (20 min, 3000 x g , 4 °C) and resuspended in lysis buffer containing 40 mM Tris, 10 mM NaH_2PO_4, 10% glycerol, pH. 8.0; 2 tablets of protease inhibitor cocktail were then added (complete mini EDTA-free, Roche #5056489001). Cells were lysed using a french press for 3 cycles at 1300 psi. After centrifugation for 30 min at 37,500 x g, the supernatant was recentrifuged using the same protocol and filtered with a 0.25 μm filter. The filtered cell lysate was loaded on a 5 ml NiNTA pre-packed column (GE Healthcare, #17524802), and the column was washed with 50 ml of lysis buffer containing 10 mM imidazole. The His-SUMO-ScSERF fusion protein was eluted with 20 mM of lysis buffer supplemented with 500 mM imidazole. ULP1 and 10 μl β-mercaptoethanol were added to the eluted material and dialyzed against 40 mM Tris, 300 mM NaCl (pH 8) overnight at 4 °C for cleavage and buffer exchange.

The cleaved His-SUMO tag was removed by a second NiNTA column equilibrated with dialysis buffer, and the tag-free cleaved ScSERF product was collected in the column flow-through. The flow-through was concentrated by a 3 K cutoff device (Amicon®, #UF900396) and diluted with anion exchange buffer (50 mM NaH_2PO_4, 125 mM NaCl, pH 6). The protein was passed over a 5 ml anion exchange column (HiTrap SP; GE Healthcare, #17115201). The proteins were eluted with a linear gradient of 20 CV with ion exchange buffer supplemented with 1 M NaCl. The elution fractions from the HiTrap column that contained ScSERF as determined by SDS-PAGE were combined, concentrated, and loaded on a 120 ml gel filtration column (HiLoad 16/60 Superdex S75; GE Healthcare, #17106801), followed by elution with 40 mM HEPES, 300 mM NaCl (pH 7.5). Fractions containing ScSERF were pooled, and the ScSERF concentration was determined with the Pierce BCA (Bicinchoninic acid) protein assay (Thermo Scientific). Samples were aliquoted and stored at - 80 °C.

ScSERF mutants A63C, L9W were purified following the same protocol. [15]N ScSERF and [15]N-[13]C ScSERF were expressed using M9 minimal-media supplemented with ^{15}N NH_4Cl and [13]C Glucose following the same purification protocol. To break off and avoid the formation of intermolecular disulfides in ScSERF A63C dithiothreitol (DTT) was added after the second NiNTA column, only monomeric protein was eluted from the SEC step.

3.3.9 Purification of M-Aβ40

M-Aβ40 (MDAEFRHDSGYEVHHQKLVFFAEDVGSNKGAIIGLMVGGVV) with an additional N-terminal methionine was purified as previously described[104]. The Aβ40 expression vector pETSaC-Aβ40 was kindly provided by Dr. Sheena Radford, University of Leeds[104]. For optimal protein expression we found it to be essential to freshly transform the expression plasmid before every purification. This plasmid was transformed into *E. coli* BL21 (DE3) cells. A single colony was used to inoculate a 5 ml LB media (100 μg/ml carbenicillin) culture for 6-10 h at 37 °C. The culture was used to inoculate a 50 ml LB Media overnight culture. A 1 l LB culture was inoculated with a starting OD_{600} of 0.1 from the overnight culture. At mid-log phase OD_{600} of 0.5 (2-4 h) expression was induced by 1 mM IPTG for 4 h at 37 °C in LB media containing 100 μg/ml carbenicillin. Cells were pelleted at 3000 x g for 20 min at 4 °C. The pellet was resuspended in 15 ml Buffer A per liter culture (10 mM Tris, 10 mM EDTA, pH 8.5) additionally 2 tablets of protease inhibitor cocktail were added (complete mini EDTA-free, Roche #5056489001). The homogenized protein sample was sonicated for

2 cycles at 30 s with 90 s pause (amplitude 10 μm, Fischer Scientific Qsonica Q500). The homogenized sample was centrifuged at 18 000 x g at 4 °C for 20 min. The supernatant was discarded and the pellet resuspended in Buffer A and stirred in the cold room for 1-2 h. The sample was sonicated again 2 cycles at 30 s with 90 s pause and centrifuged at 18 000 x g at 4 °C for 20 min. The pellet containing the Aβ40 protein in inclusion bodies was resuspended in Buffer A containing 8 M urea and stirred for 1 h in the cold room, sonicated and the suspension was centrifuged at 18 000 x g at 4 °C for 20 min. The supernatant was diluted 1 to 4 (v/v) in Buffer A and loaded on free DEAE cellulose resin (GE Healthcare # 57407-08-6). The DEAE resin was equilibrated with Buffer A prior to addition of the protein solution. The loaded DEAE resin was stirred for 30 min at 4 °C.

A Buchner funnel with filter paper (Whatman®, grade 3, #1003110), that sat on a glass flask and is connected to a vacuum line was used for the wash and elution steps. The DEAE resin was poured into the funnel and settled for 5 min, by turning on the vacuum line the liquid went through the DEAE resin and filter into the collection flask. Buffer A was added to wash. Each step was collected and transferred to a separated flask or colonial tube. Aβ40 was eluted with 4 x 50 ml volumes of Buffer A containing 125 mM NaCl and 1 x 50 ml Buffer A containing 300 mM NaCl.

The elution fractions containing Aβ40 were pooled, dialyzed against 50 mM ammonium bicarbonate buffer (pH 7.8) in 100-500 MW cutoff dialysis membranes (S/P CE 100-500 MWCO, Spectrum Laboratories #131060). The dialyzed protein was flash frozen in liquid nitrogen and lyophilized. The samples were then resuspended in 7 M guanidinium chloride (GdnHCl), 50 mM Tris (pH 8) buffer, and aggregates were removed by gel filtration on a preparative S75 column Superdex S75 HiLoad 16/60 followed by another lyophilizing and a polishing step on an analytical Superdex S75 10/300 GL (GE Healthcare, #17517401). This process yields pure and monomeric Aβ40 peptide (Appendix Fig. 29) Aβ40 was stored lyophilized at -80 °C. ^{15}N-labled Aβ40 was purified following the same protocol. The protein was expressed in M9 minimal-media supplemented with ^{15}N NH$_4$Cl.

3.3.10 Purification of α-synuclein.

The purification of α-synuclein was done as described previously[106]. α-synuclein was expressed from a pET7-7 vector plasmid transformed into *E. coli* strain BL21 (DE3). A single colony was picked and used to inoculated a 25 ml LB media (with 100 μg/ml ampicillin)

overnight culture (37 °C). The overnight culture was used to inoculate multiple 1 l LB media cultures with a starting OD_{600} of 0.1 and grown till OD_{600} 0.6 protein expression was induced with 1 mM IPTG for 4 h at 37 °C. The cultures were pelleted at 4,000 rpm (20 min, 4 °C) and resuspended in lysis buffer (10 mM Tris, 1 mM EDTA, pH 8). The homogenized cells were then boiled at 95 °C for 15–20 min and centrifuged at 11,000 rpm for 20 min. Most proteins aggregated during the heat treatment and can be sedimented during centrifugation only α-synuclein and a few other proteins stay in the supernatant after boiling the cell lysate. The supernatant was mixed with 10% (w/v) streptomycin sulphate solution (136 μl/ml) and glacial acetic acid (228 μl/ml), and nucleic acids in the pellet were removed by centrifugation at 13,500 x g for 30 min at 4 °C. An equal volume of saturated ammonium sulphate solution was added to the supernatant and incubated at 4 °C for 1 h with intermittent mixing. The precipitated protein was separated by centrifuging it at 13,500 x g for 30 min.

The pellet was resuspended in 10 mM Tris-HCl, pH 7.5, and NaOH was used to readjust the pH of the suspension to 7.5. The solution was then dialyzed against 5 L dialysis buffer (10 mM Tris-HCl pH 7.5, 50 mM NaCl) overnight at 4 °C. The protein solution was filtered and loaded onto two attached to each other 5 ml HiTrap Q HP columns (GE Healthcare, #17115401). The columns were washed with 15 column volumes of 10 mM Tris-HCl, pH 7.5, 50 mM NaCl, and the protein was eluted using a linear gradient to 500 mM NaCl. Elution fractions were analyzed by SDS-PAGE and α-synuclein-containing fractions were pooled and concentrated. To separated higher oligomeric species, form monomeric α-synuclein the protein was run over a preparative S75 column Superdex S75 HiLoad 16/60 in buffer containing 20 mM KH_2PO_4 pH 7.5. The protocol yielded pure monomeric α-synuclein protein (Appendix Fig. 30). The monomeric α-synuclein fractions were pooled, concentration and aliquots of the protein were prepared, flash frozen, lyophilized, and stored at - 80 °C.

3.3.11 Protein labeling with fluorescent dye

The labeling of the primary amines present in Aβ40 was done with Alexa Fluor 532 N-hydroxysuccinimide (NHS) ester as described by the manufacturer (Thermo Scientific #A20101MP). In brief, lyophilized monomeric Aβ40 was resuspended in 50 mM sodium bicarbonate buffer (pH 8.3) and the NHS ester dye was resuspended in 100% DMSO. The dye was added to Aβ40 at a 10-fold molar excess and incubated for 1 h in the dark at room temperature. Free dye was removed by performing gel filtration on a 24 ml (Superdex S75

10/300 Gl column (GE Healthcare, #17517401) in 50 mM ammonium bicarbonate buffer (pH 7.8). The labeled-monomeric Aβ40 fraction was pooled, aliquoted and lyophilized.

Labeling of ScSERF (A63C) was performed by first reducing any intermolecular disulfides that had formed between Cys63 residues by incubating in 20 mM Tris buffer pH 8.0, 10 mM DTT for 1 h on ice. Excess DTT was removed by gel filtration on a PD10 desalting column (GE Healthcare) into 50 mM Tris, 50 mM NaCl (pH 8.0) with a final elution volume of 3.5 ml protein. ScSERF-A63C was then incubated with 10-fold molar excess of Alexa Fluor 532 (AF532:C-5 maleimide) dye in 50 mM Tris, 50 mM NaCl (pH 8.0). The excess dye was removed by applying the sample to 24 ml size exclusion chromatography (Superdex S75 10/300 GL, GE Healthcare, #17517401). The fractions containing the labeled ScSERF were pooled together and concentrated. ScSERF has no aromatic residues to facilitate concentration determination by UV absorption. Therefore, the labeling efficiency was estimated by comparing the protein concentration as determined by BCA with the label content as determined by examining the extinction coefficient of the label ε 528 = 78,000 M^{-1}cm^{-1}. By these means, we could estimate the label to protein ratio to be ~0.9 for ScSERF A63C.

3.4   Functional and Biophysical Characterization

3.4.1   Aβ40 amyloid kinetics

To achieve reproducible Aβ40 kinetics, it is crucial to start with pure monomeric Aβ40. Thus, kinetic experiments were always proceeded with size exclusion chromatography to remove aggregates that are formed during freezing and lyophilization steps. This has been shown to be critical for reproducible amyloid assays[41]. The collected monomer fraction is kept on ice for less than 1 hour until the kinetic experiment is started.

The amyloid assay was conducted as previously described[41]. Monomeric Aβ40 was dissolved in 7 M GdnHCl, 50 mM Tris (pH 8) buffer and loaded on to an analytical 24 ml Superdex S75 10/300 column (GE Healthcare, #17517401). The center fractions of the monomer peak (13.5 ml elution volume) were collected and iced. The protein concentration was determined by using an extinction coefficient ε 280 = 1490 M^{-1}cm^{-1}. The Aβ40 protein typically had a concentration of 80–160 μM at this step. To determine the reaction mechanism Aβ40 was serial diluted in a concentration from 40 μM to 3 μM in the presence or absence of a constant ScSERF concentration.

ScSERF (YDL085C-A) was buffer exchanged into the assay buffer (20 mM NaH_2PO_4, 200 μM EDTA, pH 7.4) via a PD10 desalting column (GE Healthcare). Samples were prepared in low-binding Eppendorf tubes (Eppendorf, #Z666505) on ice, using careful pipetting to avoid air bubbles. Thioflavin T (ThT) was added to a final concentration of 25 μM (100 μM) from a 1 mM ThT stock. Each sample was then pipetted into multiple wells in 3–4 technical replicates into a 96-well plate that featured low-binding PEG coating (Corning, #3881), 90 μl per well. The plate was sealed with an adhesive sealing sheet (Thermo Scientific, #125434).

Aβ40 amyloid formation assays were initiated by placing the 96-well plate at the specified temperature of 37 °C in a Tecan Infinite M200 plate reader while reading the ThT fluorescence from the bottom using an excitation wavelength of 440 nm and an emission wavelength of 482 nm. Measurements were taken every 5 min under quiescent conditions, and shaking only occurred for 10 seconds before the fluorescence reading took place. The formation of fibrils was confirmed by transmission electron microscopy (TEM).

3.4.2 α-synuclein amyloid kinetics

Immediately prior to performing α-synuclein amyloid formation assays, preexisting aggregates/amyloids and multimers were removed from the α -synuclein preparation by first resuspending the lyophilized α-synuclein in 7 M GdnHCl, 50 mM Tris (pH 8) buffer and loading the dissolved α-synuclein onto a 24 ml analytical Superdex S75 10/300 GL column (GE Healthcare, #17517401). α-synuclein was eluted using assay buffer (20 mM NaH_2PO_4, 50 mM NaCl, 200 μM EDTA, pH 7.4); monomeric α-synuclein was collected, and its concentration was determined by using an extinction coefficient $\varepsilon\ 280 = 5960\ M^{-1}cm^{-1}$.

α-synuclein aggregation assays were performed with 100 μM monomeric α-synuclein in assay buffer (20 mM NaH_2PO_4, 50 mM NaCl, 200 μM EDTA, pH 7.4) in low-binding Eppendorf tubes on ice; ThT was added to 25 μM final concentration, and different ScSERF concentrations were added. 100 μl technical replicates were pipetted into multiple wells of a 96-well microtiter plate with a clear bottom (Corning, #3631).

Two glass beads (2-mm borosilicate glass beads) were added per reaction well to accelerate the amyloid formation. The glass beads accelerate the reaction by providing more surface area for α-synuclein to form nuclei on, and also lead to more fragmentation, which leads faster aggregation kinetics. The plate was sealed with an adhesive sealing sheet (Thermo Scientific, #125434). Assays were initiated by placing the 96-well plate at 37 °C in a Tecan Infinite M200

plate reader while reading the ThT fluorescence from the bottom using an excitation wavelength of 440 nm and an emission wavelength of 482 nm. Measurements were taken every 10 min under constant shaking in orbital mode at 300 rpm. The constant shaking results in more fibril fragmentation, which can lead to faster amyloid aggregation.

3.4.3 Self-seeded amyloid kinetics

The preparation of Aβ40 seeds and α-synuclein seeds start with the preparation of mature fibrils. Monomeric Aβ40 was prepared as described above. Aβ40 fibrils were formed in in 96-well plates with low-binding PEG coating (Corning, #3881) for at least 48 h at 37 °C under quiescent conditions. Thioflavin T was added to one sample and the ThT fluorescence signal was monitored to assure the plateau fluorescence was reached in the other ThT-free wells. The Aβ40 fibrils from these ThT-free wells were used directly for the fibril interaction anisotropy experiments.

To generate Aβ40 seeds for the kinetic experiments shown for kinetic assays described below, the solution with the pre-formed Aβ40 fibrils were sonicated for 10 min in a sonication bath (Branson, #1510). The concentration of seeds was estimated on the initial monomeric concentration used, with the assumption that all monomeric protein has been converted into fibrils and is present as seeds in the solution of sonicated Aβ40 fibrils.

Seeded ThT kinetics experiments were prepared set up as described above. The reaction mixtures were kept on ice and the generated amyloid seeds were added, in different concentrations, as the last reaction component before pipetting technical replicates into the 96-well plate (Corning, #3881) and immediately monitoring the reaction at 37 °C in a Tecan Infinite M200 plate reader while reading the ThT fluorescence from the bottom using an excitation wavelength of 440 nm and an emission wavelength of 482 nm. Measurements were taken every 5 min under quiescent conditions.

The formation of α-synuclein seeds followed a similar protocol. Monomeric α-synuclein solution with a concentration range of 300–800 μM was incubated in a Thermal mixer (Eppendorf) for 3-4 days at 40 °C with 500 rpm shaking in a low-binding Eppendorf tube. The formed fibrils generate this way were used for the anisotropy experiment.

The formed α-synuclein fibrils were then converted into seeds by sonicating them for 10 min in a sonication bath (Branson, #1510).

Seeded ThT kinetics experiments were performed as described for the non-seeded reactions. Again, seeds were the last component added to the reaction mixture. The reaction was

performed in a 96-well plate (Corning #3881) at 37 °C under quiescent conditions. Thioflavin T fluorescence was monitored in a Tecan Infinite M200 plate reader while reading from the bottom using an excitation wavelength of 440 nm and an emission wavelength of 482 nm.

3.4.4 Amyloid data analysis and fitting

3.4.4.1 Estimation of aggregation halftime

To determine the half-time of the amyloid reactions the experimental data for each curve individually were normalized so that the relative mass concentration of aggregates was 0 at time 0 and 1 at the completion of the aggregation (plateau). Kinetic data were normalized and fitted using the platform on AmyloFit (https://www.amylofit.ch.cam.ac.uk/login)[41]. The formula for normalizing the data was:

$$y_{norm,i} = \left(1 - M_{0,\text{frac}}\right)\frac{y_i - y_{\text{baseline}}}{y_{\text{plateau}} - y_{\text{baseline}}} + M_{0,\text{frac}}$$

where y_i is the signal at any time point, y_{baseline} is the average baseline fluorescence signal, y_{plateau} is the average fluorescence value of the data point after the plateau is reached, and $M_{0,\text{frac}}$ is the relative initial concentration of aggregates between time point 0 and the completion of the aggregation in the original data. The halftime is the point where the fluorescence signal has reached half of the plateau value. The halftimes were determined by fitting a straight line to the fluorescent data points that lie between 0.3 and 0.7 fraction where 0 is baseline and 1.0 is the plateau fluorescence. The point at which this line crosses the value of 0.5 is taken as the halftime.

3.4.4.2 Evaluation of reaction mechanism

To determine the reaction mechanism of Aβ40 in the absence and presence of ScSERF the serial dilution data was normalized utilizing the webserver amylofit (https://www.amylofit.ch.cam.ac.uk/login). As described previously by Meisl et. al.[41], a double-logarithmic plot of the reaction halftime against the Aβ40 monomer concentration can be used to diagnose the reaction mechanism. In both cases, a double logarithmic plot showed a slight positive curvature as previously described for Aβ40, indicating a multi-step secondary nucleation model [53,41].

3.4.4.3 Fitting of Aβ40 kinetic data

Aggregation traces of 25 μM Aβ40 with different concentrations of ScSERF in molar ratios of 0 to 100% were analyzed by the previous determined kinetic mechanism that is defined by a set of microscopic rate constants, one for primary nucleation (k_n), one for secondary nucleation (k_2), and one for fibril elongation (k_+) [45,53] In the case of unseeded aggregation, the system depends only on the combination of the rate constants for primary nucleation k_+k_n and secondary nucleation k_2k_+, not on the individual rate constants.

The kinetics were fitted by keeping the reaction orders for primary and secondary nucleation at the Aβ40 values $n_c = n_2 = 2$. The combined rate constants for primary nucleation and secondary nucleation were the only free fitting parameters. The web tool (AmyloFit) defines the multi-step secondary nucleation mechanism as follows [40]:

$$\frac{dP}{dt} = k_2 M(t) \frac{m(t)^{n2}}{1 - \frac{m(t)^{n2}}{K_M}} + k_n m(t)^{n_c}$$

$$\frac{dM}{dt} = 2\big(k_+ m(t) - k_{off}\big)P(t)$$

where $k_2 = \frac{\overline{k_2}}{K_M}$ and $K_M = \frac{k_b + \overline{k_2}}{k_f}$. Here, m_0 is the initial monomer concentration, M_0 is the initial fibril mass concentration, P_0 is the initial fibril number concentration, k_n is the primary nucleation rate constant, n_c is the critical nucleus size for primary nucleation ($=2$), n_2 is the critical nucleus size for secondary nucleation ($=2$), K_M is the Michaelis-Menten constant, which determines the monomer concentration at which secondary nucleation begins to saturate, and k_+ is the elongation rate constant. The integrated rate law for the normalized aggregate mass concentration was determined by amylofit as

$$\frac{[M]}{[M]_\infty} = 1 - \left(1 - \frac{[M]_0}{[M]_\infty}\right) e^{-k_\infty t} * \left(\frac{B_- + C_+ e^{kt}}{B_+ + C_+ e^{kt}} * \frac{B_+ C_+}{B_- C_+}\right)^{\frac{k_\infty}{\kappa k_\infty}}$$

where the definitions of the parameters are

$$\kappa = \sqrt{2[m]_0 k_+ \frac{[m]_0^{n2} k_2}{1 + [m]_0^{n2}/K_M}}$$

$$\lambda = \sqrt{2k_+ k_n [m]_0^{n_c}}$$

$$C_\pm = \frac{k_+ [P]_0}{k} \pm \frac{k_+ [M]_0}{2[m]_0 k_+} \pm \frac{\lambda^2}{2\kappa^2}$$

$$k_\infty = 2k_+ [P]_\infty$$

$$\bar{k}_\infty = \sqrt{k_\infty^2 - 2C_+ C_- k^2}$$

$$k_\infty = \sqrt{(2k_+ P(0))^2 - 2A - 4k_+ k_2 m_{tot} K_M \frac{\log[K_M]}{n_2}}$$

$$A = \frac{2k_+ k_n m_0^{n_c}}{n_c} - 2\, k_+ k_2 m_{tot} K_M \frac{\log[K_M]}{n_2} - 2k_+ k_2 K_M m_0 (_2F_1\left[\frac{1}{n_2}, 1, 1 + \frac{1}{n_2}, -\frac{m_0^{n_2}}{K_M}\right] - 1)$$

$$B_\pm = \frac{k_{\infty\pm}\bar{k}_\infty}{2\kappa}$$

3.4.5 Simulation of kinetic data

The integrated rate laws based on the mechanism described by the Knowles group [64] above can be simulated to gain insight a change in parameters can have on the observed kinetic traces. Aβ40 amyloid kinetics were simulated using kinetic simulation software Berkley Madonna (https://berkeley-madonna.myshopify.com/). The initial rate constants used for Aβ40 were: primary nucleation rate (k_2) = 2×10^{-6}, elongation rate (k_4) = 3×10^5, and secondary nucleation rate (k_3) = 3×10^3. The following integrated rate laws and parameters were used for the sumulation[64]:

$$\frac{dP(t)}{dt} = k_1(M(t) - (2n_c - 1) * P(t)) + k_2 x(t)^{nc} + k_3 M(t) m(t)^{n2}$$

$$\frac{dM(t)}{dt} = (k_4 x - n_c(n_c - 1)\frac{k_1}{2})P(t) + n_c k_2 x(t)^{nc} + n_2 k_2 M x(t)^{n2}$$

$$\frac{d(x)}{dt} = -n_c k_2 x^{nc} - n2 k_3 M x^{n2} - 2k_4 x P(t)$$

where $n = 2$, $n_c = 2$, $x = 25$ μM Aβ, $M(t)$ = Fibrils mass fraction, $P(t)$ = Total fibril number

The rate constants were varied and the change in the kinetic traces was observed.

3.4.6 Monomer binding by fluorescence anisotropy

To determine the equilibrium dissociation constant K_d for monomeric Aβ40, α-synuclein and ScSERF, fluorescence anisotropy was performed. Prior to the experiment both amyloid proteins were loaded on to an analytical 24 ml Superdex S75 10/300 column (GE Healthcare, #17517401.

In a 1 ml cuvette at 25 °C, 200 nM AF532-labeled Aβ40 in 20 mM ammonium acetate, pH 7.4, was titrated with a stock of ScSERF (2.2 mM) also in 20 mM ammonium acetate, pH 7.4.

The binding between monomeric AF532-labeled ScSERFA63C and unlabeled monomeric α-synuclein was monitored by fluorescence anisotropy conducted in a similar manner by titrating α-synuclein into 500 nM AF532-labled ScSERFA63C (20 mM ammonium acetate, pH 7.4) at 25 °C. The proteins used in the binding experiments were subsequently analyzed by analytical ultracentrifugation to confirm that no oligomeric species was present.

Anisotropy was calculated according to the following equations:

$$G = \frac{I_{hv}}{I_{hh}}$$

$$r = \frac{I_{vv} - GI_{vh}}{I_{vv} + 2GI_{vh}}$$

where G is the instrument correction factor, r is anisotropy, and I is the fluorescence intensity measured with polarizers in the orientations indicated in the subscripts (v is vertical and h is horizontal). Anisotropy was recorded with a Cary Eclipse Spectrofluorometer (Agilent) using λex = 532 nm (5 nm bandpass) and λem = 552 (10 nm bandpass). The titration data was fitted to the following binding isotherm

$$f_a = \frac{\Delta f_a \left[Ligand_{(ScSERF\ or\ \alpha Syn)} \right]}{(K_d + \left[Ligand_{(ScSERF\ or\ \alpha Syn)} \right])} + f_{a,0}$$

where f_a is the fluorescence anisotropy signal, Δf_a is the total signal change, $f_{a,0}$ is the y axis intercept, K_d is the dissociation constant.

3.4.7   Fibril binding by fluorescence anisotropy

To test whether ScSERF can bind to preformed amyloid fibrils. Amyloid fibrils were prepared as described above, in assay buffer 20 mM NaH_2PO_4, 200 μM EDTA, pH 7.4. The fluorescence anisotropy of 500 nM AF532-labeled ScSERFA63C was measured in Cary Eclipse Spectrofluorometer (Agilent) and anisotropy was calculated as described above.

Pre-formed amyloid fibrils of Aβ40 or α-synuclein were added to AF532-labeled ScSERFA63C. The fibril concentration was estimated based on the starting monomer concentration with the assumption that all of the monomeric amyloid protein was converted into amyloid fibrils. To test if ScSERF can integrate into amyloid fibrils. Fibrils were formed in the presence of AF532-labeled ScSERFA63C and later competed with unlabeled ScSERF.

3.4.8 Circular dichroism spectroscopy

Circular dichroism (CD) spectroscopy relies on the differential absorption of circularly polarized light containing a counter-clockwise (L) and clockwise (R) rotating component. Secondary structure elements in proteins like α-helices or β-sheets show characteristic signal in CD spectra, and therefore can be used to study the secondary structure content of proteins. To monitor changes in the secondary structure of ScSERF, ScSERF was diluted into 20 mM NaH$_2$PO$_4$ pH 7.4, 25 mM NaCl to a final concentration of 0.2 mg/ml. Far-UV CD spectra were taken by scanning from 190 nm to 250 nm in a J-1500 spectrophotometer (Jasco) at the indicated temperatures. The mean residue ellipticity $[\theta]_{mrw,\lambda}$ was calculated as follows[107]:

$$[\theta]_{mrw,\lambda} = MRW\ [\theta_\lambda]/10\ d\ c$$

where MRW is the mean residue weight, θ_λ is the observed ellipticity (degrees) at wavelength λ, d is the path length (0.1 cm), and c is the concentration in mg/ml.

3.4.9 Monitoring amyloid fibrils by transmission electron microscopy (TEM)

After completion of amyloid formation, the samples were analyzed by transmission electron microscopy (TEM microscopy).

Negative staining is a method to contrast the sample. The background is stained, while leaving the fibrils visible. The samples were stained with 1.5% uranyl formate solution on formvar grid with a carbon film. The protocol was outlined here [108]. In brief, 5 μl of fibril sample was spotted on a formvar grid with a carbon film and blotted for 5 min and removed with a Whatman filter paper. The grid was subsequently stained for 1 min with 5 μl of a 1.5% uranyl formate solution. The solution was removed by a Whatman filter paper. The fixed and stained grids were stored and imaged at room temperature. The samples were imaged using either a Tecnai T12 or JEOL JEM-1400 (Plus) TEM. Negatively staining and imaging was conducted in collaboration with Dr. Tony Ludlam and Dr. Michael Cianfrocco at the University of Michigan.

3.4.10 Sedimentation Velocity Analytical Ultracentrifugation experiment (SV-AUC)

Analytical Ultracentrifugation was used to determine the oligomeric state of ScSERF, Aβ40 and α-synuclein. Sedimentation velocity experiments can inform on the oligomeric state and the hydrodynamic shape of a protein. AF532-labeled Aβ40 at an OD of 0.2 at 532 nm was used to determine the oligomeric state of the AF532-labeled Aβ40 used for binding assays in solution. Sedimentation of AF532-labeled Aβ40 was monitored by absorbance at 532 nm at 59 krpm. ScSERF proteins and variants were monitored at different wavelength. ScSERF WT was monitored at 230 nm, ScSERFL9W was monitored at 280 nm. ScSERF was sedimented at 58 krpm at 22°C. α-synuclein was monitored at 280 nm and sedimented at 58 krpm at 15°C. Samples were measured in anisotropy binding buffer (20 mM ammonium acetate, pH 7.4) with the addition 50 mM NaCl to avoid the possibility of nonideality. SV-AUC was carried out using 400 µl loaded into two-sector titanium centerpieces with 1.2 cm path-length in an An60Ti rotor in a Beckman Optima Xl-I analytical ultracentrifuge. Measurement was completed in intensity mode.

All SV-AUC data were analyzed using UltraScan 4 software, version 4.0 and fitting procedures were completed on XSEDE clusters at the Texas Advanced Computing Center (Lonestar, Stampede) through the UltraScan Science Gateway (https://www.xsede.org/web/guest/gateways-listing)[109]. The partial specific volume (vbar) of Aβ40, α-synuclein and ScSERF was estimated within UltraScan III based on the protein sequence[110]. Raw intensity data were converted to pseudo-absorbance by using the intensity of the air above the meniscus as a reference and edited. Next, 2-dimensional sedimentation spectrum analysis (2DSA) was performed to subtract time-invariant noise and the meniscus was fit using ten points in a 0.05-cm range[111]. First arrays with a broad S range were fitted to account for possible large oligomeric states. Final arrays were fit using an S range 0.2-3, an f/f0 range of 1–4 with 64 grid points for each, 10 uniform grid repetitions and 400 simulation points. 2DSA was then repeated at the determined meniscus to fit radially invariant and time-invariant noise together using ten iterations. The 2DSA solution was refined by a genetic algorithm (GA), which uses an evolutionary based approach using random cross-over, mutations and deletion operations to alter the solute characteristics of the 2DSA solutes to eliminate false positive solutions[112]. The results from the genetic algorithm were evaluated using a Monte Carlo algorithm.

3.4.11 Structural characterization of ScSERF by NMR spectroscopy

Nuclear magnetic resonance (NMR) spectroscopy experiments were performed in collaboration with Dr. Debashish Sahu, at the BioNMR Core and Dr. Joshua Damron from the Ramamoorthy lab at the University of Michigan. NMR spectroscopy in comparison to other spectroscopic methods has the ability to detect changes on an atomic level.

Isotopic labeled ScSERF was used to collect two-dimensional ^{1}H-^{15}N HSQC (Heteronuclear Single Quantum Coherence) spectra, that shows all N-H correlation e.g. signals from all backbone amide groups expected for prolines and certain sidechain signals (Arg, Trp, Asn, Gln).

The amide chemical shifts are influenced by the local environment making it possible to track changes in the chemical shift due to changing conditions like temperature, pH or due to addition of a binding partner. All spectra used for sequence-specific resonance assignments were collected at 4 °C in 20 mM NaH_2PO_4 pH 7.0 buffer at 900 Mhz Bruker AVANCE™ at Michigan State University. ^{15}N,^{13}C-labeled ScSERF was desalted via PD10 (GE healthcare) column into assay buffer (20 mM NaH_2PO_4 pH 7.0) and 10% D_2O was added to the sample, final ScSERF concentration was 1.6 mM estimated by BCA assay.

Sequence-specific resonance assignments of ScSERF ^{1}H-^{15}N HSQC spectra was obtained by collecting a set of triple resonance data. The three-dimensional experiments HNCαCβ, HN(CO)CαCβ, and HNCα were collected with 2048 (^{1}H) x 60 (^{15}N) x 142 (^{13}C) points at a 900 MHz NMR Bruker (MSU, Lansing). The HNCαCβ spectra correlate each NH group with the Cα and Cβ chemical shift of its own residue (strong signals) and the preceding NH$_{i-1}$ residue (weaker signals). The HN(CO)CαCβ only contains the signal of the NH$_{i-1}$ residue. These correlations and the characteristic Cα and Cβ shift for amino acids can be used to assign the signals detected in the ^{1}H-^{15}N HSQC spectra. All spectra were processed using NMRPipe and analyzed with Sparky.

Initially peaks were picked in Sparky and a probability assignment was generated using PINE (http://i-pine.nmrfam.wisc.edu/). The automatic assignment was validated by manually following the sequential resonance assignment.

CS-Rosetta webserver (https://csrosetta.bmrb.wisc.edu/csrosetta/submit) was used to calculate the structural model for ScSERF based on the backbone assignment. TALOS was used to predict the backbone dihedral angles based on the backbone assignments[113]. For MOAG-4 the BMRB entry #27058 was used to generate a CS-Rosetta model to compare to our ScSERF model.

NMR spectroscopy was used to characterize the interaction between ScSERF and isotopic labeled ^{15}N-Aβ40. Lyophilized ^{15}N-Aβ40 was resuspended in 7 M GdnHCl, 50 mM Tris (pH 8) buffer and loaded on to an analytical 24 ml Size-exclusion column Superdex S75 10/300 column (GE Healthcare, #17517401) and eluted in assay buffer (20 mM NaH$_2$PO$_4$, 200 μM EDTA, pH 7.4). The center fractions of the monomer peak (13.5 ml elution volume) were collected and concentration was determined. The final sample contained 116 μM ^{15}N-Aβ40 and 10 % D$_2$O were added. The ^{15}N-Aβ40 HSQC spectra was collected at Bruker Ascend^{TM} 800 MHz at the University of Michigan at 4 °C. ScSERF was buffer exchanged into the same buffer used for size-exclusion column and concentrated to exclude any chemical shift changes due to pH or buffer changes. ScSERF was titrated into the sample of ^{15}N-Aβ40 in equimolar and 3-fold molar excess ratio respectively and HSQC experiments were performed. The spectra were processed using NMRPipe and Sparky. The decrease in signal intensity of ScSERF addition was corrected for dilution and plotted as a relative change of intensity. A small shift in peaks was observed and the relative average chemical shift change Δδ was calculated as shown below[114]:

$$\Delta\delta[ppm] = \sqrt{\frac{\Delta\delta\,(^1H)^2 + \frac{1}{25}\Delta\delta(^{15}N)^2}{2}}$$

3.4.12 Native Ion-mobility Mass spectrometry measurements

An overview of the basic of Native IM-MS is described in the introduction. After sample preparation the measurements and data analysis were performed in collaboration with Dr. Varun Gadkari from the Ruotolo lab at the University of Michigan.

Native IM-MS experiments were carried out on a Synapt G2 traveling wave ion mobility-mass spectrometer (Waters). Aqueous samples were introduced into the gas phase by a nanoelectrospray ionization (nESI) source operated in positive ion mode. Ions were generated using a capillary voltage of 1100-1200 V and sample cone voltage of 10 V. The instrument was operated with a backing pressure of 2.63 mbar, source pressure of 7.38×10^{-3} mbar, trap pressure of 3.34×10^{-2} mbar, IM pressure of 3.47 mbar, transfer pressure of 1.00×10^{-6} mbar, and time-of-flight (ToF) pressure of 1.44×10^{-6} mbar. The IM wave height was 30 V and the IM wave velocity was 600 m/s.

ScSERF was co-incubated with Aβ40 or α-synuclein to a final concentration of 25 μM each in 20 mM ammonium acetate, pH 7.4. A ThT assay was carried out in these buffer conditions to verify that the aggregation kinetics of Aβ40 was not changed due to the change in reaction buffer. Samples were incubated at 37 ℃. Time course experiments were conducted by setting up separate reactions that were removed from 37 ℃ at the indicated times for IM-MS analysis. All reactions were diluted 2.5-fold to final concentrations of 10 μM prior to IM-MS analysis to prevent nonspecific interactions due to nESI. Although, various sub-stoichiometric ratios of ScSERF to Aβ40/α-synuclein were screened by other methods, a 1:1 ratio was chosen for the IM-MS experiments to ensure that ScSERF bound complexes were sufficiently abundant to be observed. The 1:1 ratio was the highest ratio of ScSERF to Aβ40/α-synuclein where ScSERF was still observed to accelerate aggregation. Thus, we anticipate that the complexes observed at this ratio are representative of those present at sub-stoichiometric ratios.

ATDs were fit to a minimal number of Gaussian functions, and the peak centers of the Gaussian functions were converted to CCSs using a previously described protocol [115]. CCS measurements were calibrated using native β-lactoglobulin, ubiquitin, cytochrome C, insulin, melittin, and denatured ubiquitin. Calibration was conducted using a database of known values in helium, and all CCS values reported are an average of at least 3 replicates. The associated least square error with each average CCS combines inherent calibrant error from drift tube measurements (3%), the calibration curve error (R^2), and two times the replicate standard deviation error as per a previously published protocol [116].

The dissociation constant of ScSERF binding to Aβ40 monomer was determined by preparing samples containing 2 μM ScSERF, and 5, 10, 40, and 60 μM of Aβ40 in 20 mM ammonium acetate buffer (pH 7.4). Titration of Aβ40 beyond a final concentration of 60 μM resulted in Aβ40 aggregation, which interfered with the K_d measurement. Each sample was analyzed three times by three separate nESI needles. The three analyses were treated as three technical replicates and plotted separately. The mass spectra were integrated to determine total abundances of free and bound ScSERF.

Since the ionization efficiencies of ScSERF and ScSERF:Aβ40 vary significantly, we utilized the response factor R as described previously:

$$R = \frac{PL}{P}$$

where PL is the total signal abundance of ScSERF: Aβ40, and P is the abundance of unbound ScSERF. To account for the difference in ionization efficiency the response factor relationship (R/R+1) was plotted against the corresponding concentration of Aβ40 for all three replicates, and all points were fit to the following nonlinear equation adapted from Ishii et al. [117]:

$$\frac{R}{R+1} = 0.5 * \frac{K_d}{[ScSERF]0} * \left[1 + \frac{[ScSERF]_0}{K_d} + \frac{[A\beta40]_0}{K_d} - \sqrt{\left(1 + \frac{[ScSERF]_0}{K_d} - \frac{[A\beta40]_0}{K_d}\right)^2 + \frac{4[A\beta40]_0}{K_d}} \right]$$

where $[ScSERF]_0$ and $[A\beta40]_0$ are the initial concentrations of the respective species, and K_d is the dissociation constant.

Raw data was analyzed using MassLynx (Waters). ATDs for all CCS calibrants as well as ScSERF complex samples were extracted from raw data using TWIMExtract[95], and ion mobility ATDs were fit to Gaussian functions using CIUSuite2[96].

4   Results[1]

4.1   Structural characterization of ScSERF

MOAG-4/SERF protein family is highly conserved proteins in eukaryotes (Fig. 6). The yeast homologue YDL0850C-A (ScSERF) hadn't been studied. The collection of structural information is important if one wants to understand the structural basis behind protein function and mechanism. The structural information we obtained here was compared to the recently published information on the *C. elegans* homologue MOAG-4[91]. ScSERF was codon-optimized for expression in *E. coli* and cloned into a pET28-His-Sumo vector, the His-SUMO-ScSERF protein purified and elutes as a monomeric protein (Appendix Fig. 28).

To evaluate the secondary structure content of ScSERF, circular dichroism (CD) spectra were taken over a range of temperatures (Fig. 8 A). ScSERF shows that an α-helical signal is present at low temperatures, with increasing temperatures ScSERF's α-helical content decreases from 24 % at 4 °C to 4 % at 40 °C, as estimated by deconvolution of the CD-spectra[118].

The Heteronuclear Single Quantum Coherence (HSQC) spectra of ScSERF collected at 4 °C shows a more dispersed peak distribution in comparison to HSQC spectra collected at 30 °C (Fig. 8 B), indicating a more structured conformation at low temperatures, consistent with the CD secondary structure analysis. The HSQC spectra at 4 °C was assigned by collecting triple resonance experiments. The chemical shifts determined from the backbone assignment of ScSERF can be used to predict the torsion angles of the peptide backbone, which can be used to predict secondary structure elements in the protein sequence. The program TALOS was used to predict ScSERF secondary structure[119]. The C-terminal residues from residue 45 to 65 are predicted to be in an α-helical structure. Furthermore, the NMR assignments and TALOS calculations can be used to model ScSERF structures. The web server CS-Rosetta converged on low energy structures based on the NMR data input[120].
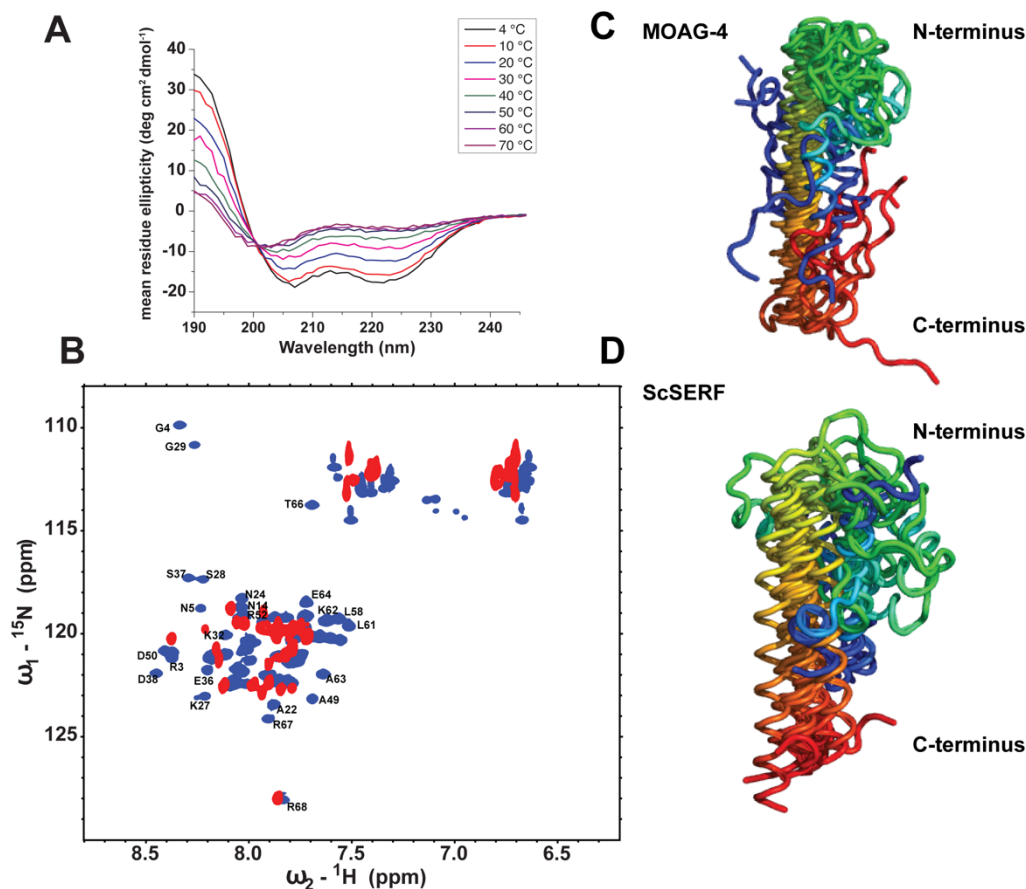
Figure 8: Structural characterization ScSERF.
(A) Temperature dependency of ScSERF secondary structure. CD signal of 0.2 mg/ml ScSERF plotted as mean residue ellipticity collected at increasing temperatures. (B) HSQC [15]N ScSERF at 277 K (4°C) blue spectra with some of the made residue assignments and at 303 K (30°C) red spectra. (C) CS-Rosetta structure model for MOAG-4 based on bmrb entry ID 27058 from Yoshimura et al.[91].Overlay of ten lowest energy structures (D) CS-Rosetta structure model based on backbone assignments for ScSERF. Overlay of ten lowest energy structures generated by CS-Rosetta (https://csrosetta.bmrb.wisc.edu/csrosetta/)[120–122].

The ensemble of the ten lowest energy structures is consistent with the TALOS prediction and shows the propensity to form a α-helix from residues 45-68 and a disordered N-Terminal sequence (Fig. 8 D). It is interesting to point out that the N-Terminal region in ScSERF is highly conserved across all eukaryotic species (Fig. 6), but is disordered in ScSERF and MOAG-4 (Fig. 8 C, D). This is different from many intrinsically disordered proteins which tend to show a much lower degree of sequence conservation[123]. We generated a CS-Rosetta ensemble for MOAG-4 based on the published NMR assignments (BMRB #27058)[91], to

compare our model with a model for MOAG-4. In comparison our NMR informed computational model for ScSERF agrees quite well with the NMR structure ensemble published for the homologue MOAG-4 (Fig. 8 C)[91].

4.2 ScSERF as a modifier of amyloid formation

Falsone et al. showed that SERF1a the human homologue to ScSERF accelerates the amyloid formation of multiple amyloidogenic proteins including α-synuclein, Aβ40, polyQ and PrP prion protein[90]. Nevertheless, the mechanism by which SERF leads to amyloid acceleration has not been elucidated. In this section we used the advances made in studying Aβ40 amyloid formation to characterize the mechanism by which ScSERF affects Aβ40 amyloid formation.

4.2.1 Establishing Aβ40 amyloid aggregation assay

Recently, the Knowles group developed a framework to quantify and analyze amyloid-β amyloid kinetics [41]. The first crucial step is to generate pure and monomeric Aβ40 peptide, this first involves the purification of recombinant Aβ40 from inclusion bodies (Appendix Fig. 29). The purified and lyophilized Aβ40 was applied to an analytical size-exclusion column (S75). The center of the monomer peak was collected and used immediately to start the amyloid aggregation (Fig. 9 A). The use of freshly purified monomeric Aβ40 has been shown to be essential for reproducible amyloid kinetic assays as the spontaneous stochastic formation of oligomeric amyloid nuclei greatly decreases reproducibility. The amyloid kinetics can be followed by monitoring Thioflavin T (ThT) fluorescence over time. The fluorescence of ThT increases when this fluorophore binds to the cross-β structure of amyloid fibrils, typically a sigmoidal curve for amyloid aggregation results[124]. The amyloid kinetics determined for Aβ40 by ThT fluorescence follow the published pattern and could be fitted to the published mechanism of multistep secondary nucleation for Aβ40 aggregation (Fig. 9 B)[53].
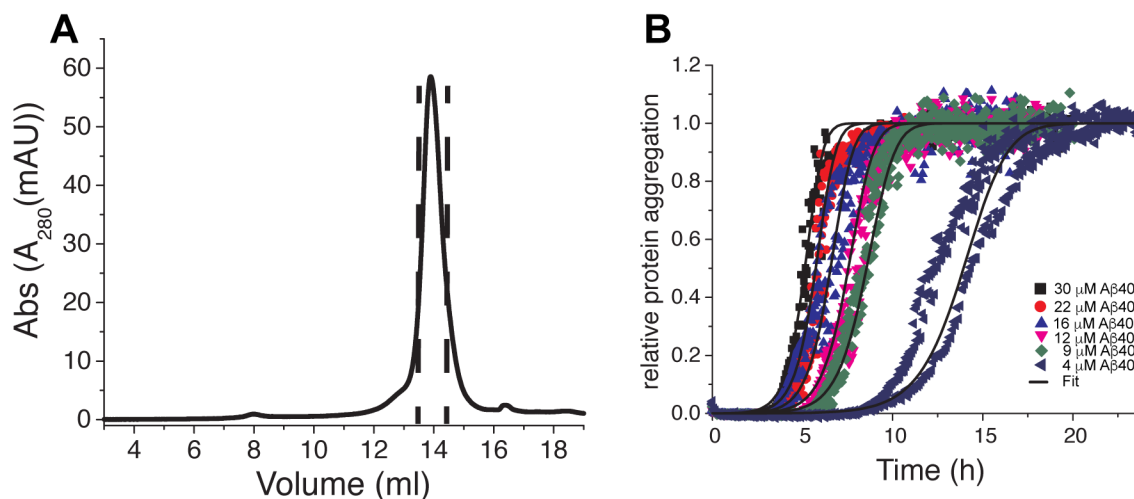
Figure 9: Aβ40 amyloid kinetics.
(A) Size elution chromatogram of Aβ40 on analytical S75 column, marked are the center fractions taken for kinetic assays. (B) ThT assay of a serial dilution of Aβ40 monomeric protein. Assay was conducted under quiescent conditions at 37 °C (20 mM NaH_2PO_4, 200 μM EDTA, pH 7.4). Data was fitted to multistep secondary nucleation mechanism using amylofit [41].

4.2.2 ScSERF accelerates Aβ40 amyloid formation

To investigate the effect of ScSERF on Aβ40 aggregation, a range of ScSERF concentrations were added to a constant concentration of Aβ40. ScSERF accelerates Aβ40 amyloid aggregation at sub-stoichiometric concentrations (Fig. 10 A). The halftime of Aβ40 amyloid formation is reduced from 6 h which is what occurs with Aβ40 alone to 2.6 h upon addition of a 1: 0.1 Aβ40: ScSERF ratio. This acceleration is less pronounced at equimolar Aβ40: ScSERF ratios but the lag time is still reduced by over one hour (Fig. 10 B).

Unexpectedly, in the presence of a large molar excess of ScSERF to Aβ40, the amyloid kinetics are slower, a high molar-excess concentration of ScSERF increased the halftime of Aβ40 amyloid formation (Fig. 10 E). The fibrils present at the end of the reaction were examined by transmission electron microscopy (TEM). On the surface, the morphology of the formed amyloid fibrils appeared unchanged (Fig. 11 A-F), but in presence of a molar-excess of ScSERF, amorphous aggregates appeared in the addition to the excepted amyloid fibrils (Fig. 10 D, 11 G-H). These amorphous aggregates were not observed for fibrils formed in the presence of low concentration of ScSERF (Fig. 11 C, D).
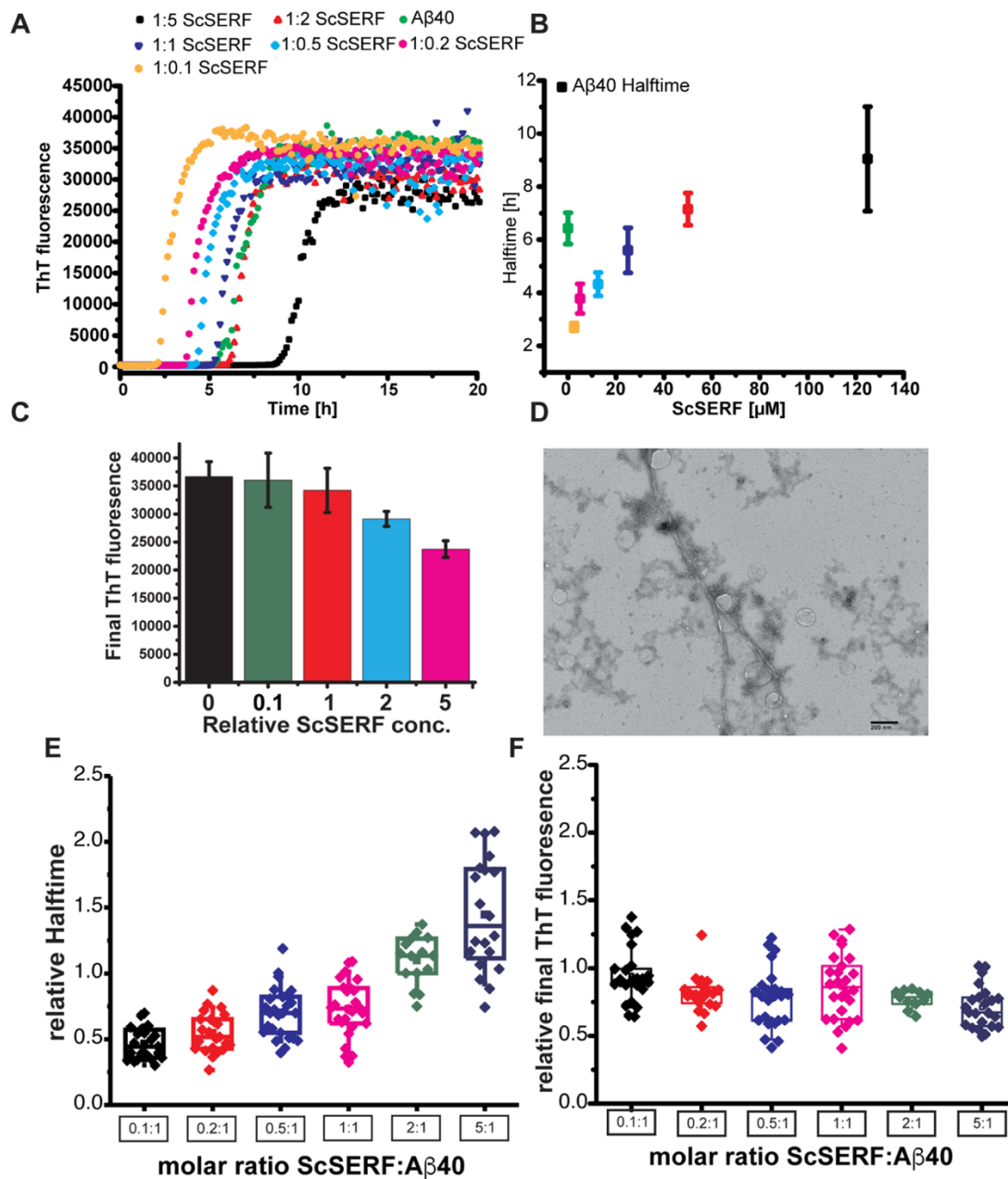
Figure 10: ScSERF modifies Aβ40 aggregation in a bi-modal fashion.
(A) The kinetics of Aβ40 amyloid formation as measured by ThT fluorescence for 25 μM Aβ40 incubated in the absence (black) or presence (various colors) of different concentrations of ScSERF. (B) Halftimes of Aβ40 amyloid formation plotted against the indicated concentrations of ScSERF. Assays were conducted under quiescent conditions at 37 °C (20 mM NaH_2PO_4, 200 μM EDTA, pH 7.4). (C) Final ThT fluorescence of the plateau phase's dependence on various ScSERF concentrations (shown in panel A). (D) representative TEM image of Aβ40 fibrils formed after 48 hours incubated in the presence of 5 molar excess ScSERF (E, F) Box plot of analysis of 3-4 independent Aβ40 ThT aggregation experiments. Box signifies upper and lower quartiles, median is represented by the line in the box. (E) Changes of halftime for different ScSERF concentration are normalized to Aβ40 halftime (=1). (F) Analysis of the relative change in final ThT fluorescence to final Aβ40 fluorescence (=1) (Figure adapted after Meinen *et al.,* 2019).

Consistent with these observations, we found that in some of the assays, the final ThT fluorescence was reduced in the presence of an excess of ScSERF (Fig. 10 C). The final ThT fluorescence relative to the observed Aβ40 final ThT fluorescence did not show a clear correlation with ScSERF concentrations across multiple experiments (Fig. 10 F). Nevertheless, it appears that the molar-excess ScSERF concentrations show overall slightly lower final ThT fluorescence values. ThT fluorescence depends on the concentration of amyloid protein, the morphology of the fibrils and ThT concentration[125]. The observation of non-amyloid aggregation by TEM suggest that high ScSERF concentrations can cause the formation of off-pathway aggregation of Aβ40. In the context of other modifies amyloid-β off-pathway aggregation has been observed, for example in experiments conducted with equimolar concentration of Zn^{2+} ions[126].

4.2.3   Aβ40 amyloid fibrils in the presence of ScSERF

After 48 hours of incubation, at the completion of the ThT fluorescence kinetics, samples were taken and visualized using transmission electron microscopy. Aβ40 fibrils formed in the presence and absence of 1:0,1, 1:1, 1:5 molar ratios of ScSERF, were at least superficially indistinguishable, all showing the previously described twisted fibril structures (Fig. 11A-F). As mentioned in the previous section, an excess of ScSERF leads to a decrease in ThT fluorescence and at these concentrations we observed non-fibral aggregation (Fig. 11 G, H). ScSERF itself does not form any aggregates or ThT reactive species by itself consistent with observations made for SERF1a (Fig. 11 I)[90].
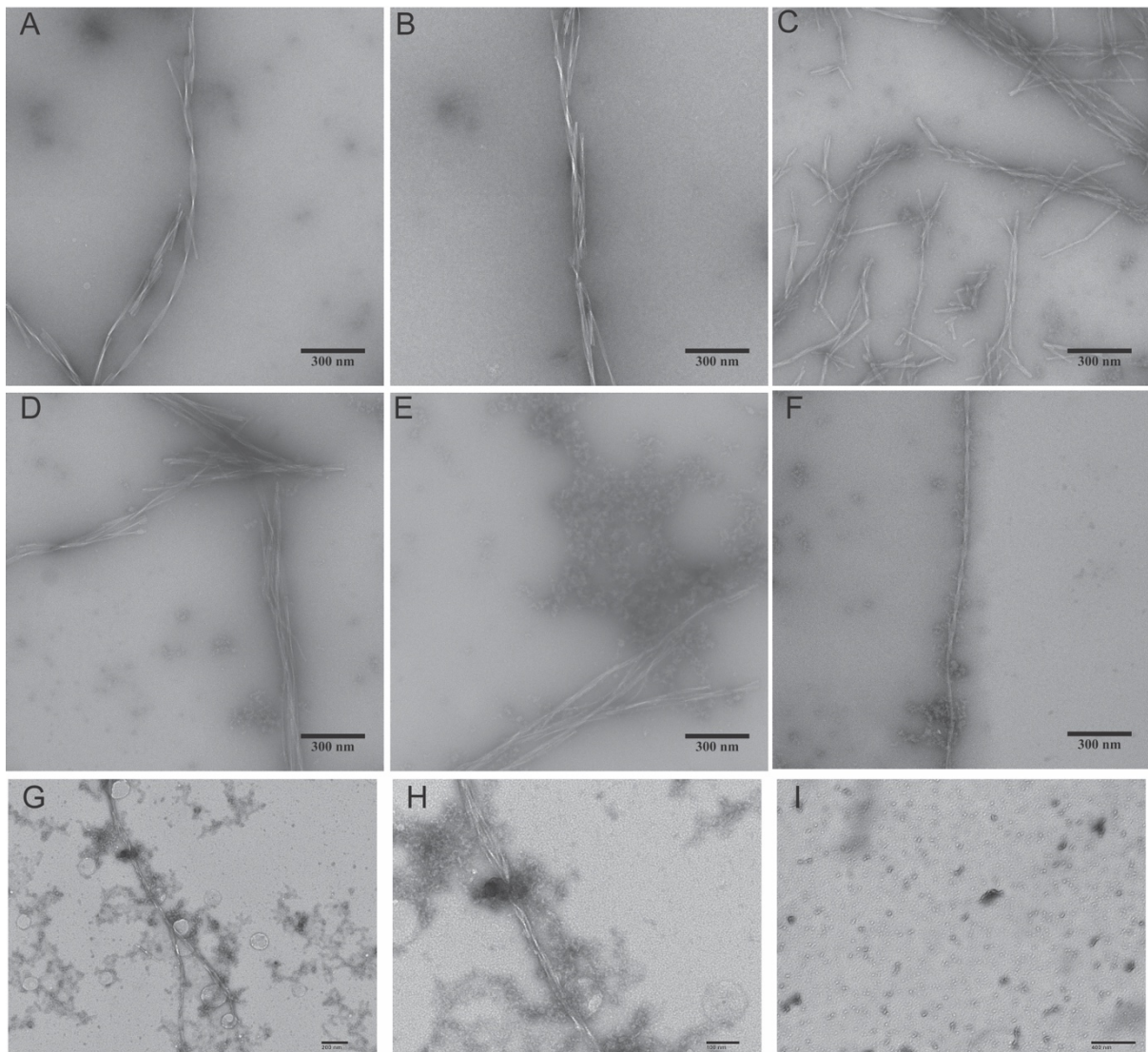
Figure 11: TEM characterization of Aβ40 fibrils +/- ScSERF.
Aβ40 was incubated in the presence or absence of different molar ratios of ScSERF for 48 h. Images were taken by TEM. (A, B) Representative images of Aβ40 fibrils. (C, D) Images of Aβ40 fibrils in the presence of 0.1 molar equivalent of ScSERF. (E, F) Images of Aβ40 fibrils in the presence of 1 molar equivalent of ScSERF. (G, H) Images of Aβ40 fibrils in the presence of 5 molar equivalent of ScSERF (I) Image of ScSERF alone, also incubated for the duration of the ThT experiment (Figure adapted after Meinen *et al.,* 2019).

4.2.4   Mathematical modeling of amyloid kinetics

One tool used to visualize amyloid kinetics is simulation. We thus simulated the published kinetic mechanism for Aβ40 aggregation using the software Berkley Madonna (https://berkeley-madonna.myshopify.com/). These simulations allow us to visualize how aggregation kinetics should change in response to changes in the various rate constants involved. A change in the primary nucleation rate constant leads to a change in the lag-phase

but does not affect the shape of the aggregation curve (Fig. 12 A). Changes in elongation and secondary nucleation affect both the slope of the aggregation curve and the lag phase, but in distinguishable ways (Fig. 12 B, C). A comparison of the simulated curves and the experimental data (Fig. 12 A) shows that the simulation where we varied the primary nucleation rate matches well with the experimentally observed kinetics (Fig. 13 C), much better than when we changed the elongation and secondary nucleation rates. In the following we used data fitting to test this hypothesis.
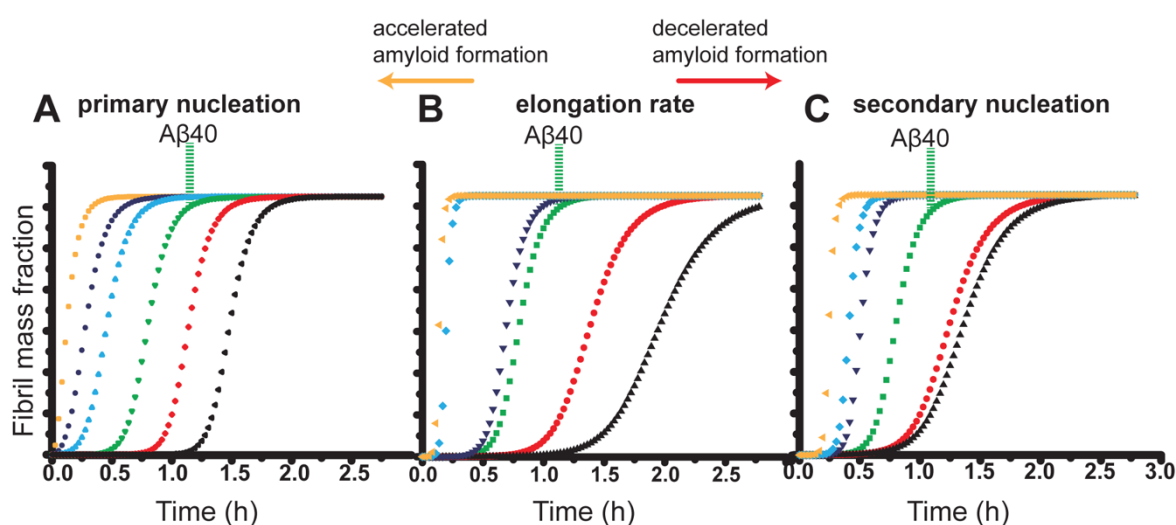
Figure 12: Mathematical modeling of amyloid kinetics.
Simulation of 25 μM Aβ40 amyloid kinetics based on the published model; simulation with the published rate constants is shown in green (primary nucleation rate = 2×10^{-6}, elongation rate = 3×10^{5}, and secondary nucleation rate = 3×10^{3}) [53]. Increasing the primary nucleation (A), secondary nucleation (C) or elongation rate (B) (blue, purple, orange lines) or decreasing it (red, black lines) changes the lag time, or curvature of the plot[64] (Figure adapted from Meinen et al., 2019).

4.2.5 Determination of Aβ40 amyloid mechanism in the presence of ScSERF

Since we could generate reproducible amyloid formation kinetic traces we reasoned that these could be used to determine which specific step in Aβ40 amyloid formation is affected by ScSERF. To do this, first, the reaction mechanism in the presence of ScSERF was determined. The halftimes were determined as described in the method section, using the webtool amylofit (https://www.amylofit.ch.cam.ac.uk)[41]. It has been shown that a double-logarithmic plot of Aβ40 monomer concentration against the aggregation halftime changes its shape dependent on the underlying amyloid mechanism. A linear concentration-dependence indicates that the mechanism is the same for all concentration this has been the case for the aggregation of

Aβ42[41,53]. A positive curvature with a change in slope at higher concentrations indicates a saturation effect at higher amyloid protein concentrations. This behavior has been observed in the past for aggregation of Aβ40[53]. In our assay the Aβ40 control sample showed the published pattern (Fig. 13 A, B). The addition of a sub-stoichiometric concentration of ScSERF lead to the acceleration of amyloid formation, but did not affect the shape of the double-logarithmic plot (Fig. 13 A, B). This insensitivity to shape indicates that the overall reaction mechanism of Aβ40 is not changed by ScSERF, but rather a step in the kinetics of Aβ40 aggregation is affected.

4.2.6 ScSERF accelerates primary nucleation

We used the amylofit tool (https://www.amylofit.ch.cam.ac.uk) to determine the changes in microscopic rate constant that occurred in the presence of ScSERF[41]. As a first step, the ThT fluorescence data is normalized, the model assumes that the final ThT fluorescence is proportional to the starting concentration of monomeric amyloid protein. The samples containing a high molar excess of ScSERF were excluded from the following analysis, because the models available are unable to account for the formation of off-pathway amorphous aggregation.

To determine the rate constant that ScSERF affects, the ScSERF concentration from sub-stoichiometric to equimolar concentration were fitted to the determinate mechanism of multi-step secondary nucleation process. In the mechanism of multi-step secondary nucleation, three rate constants are determined, k_n, the rate constant for primary nucleation, k_+, the rate constant for elongation and k_2, the rate constant for secondary nucleation. In an unseeded aggregation reaction, the amyloid kinetics depend on the combination of the rate constant for primary nucleation k_+k_n and secondary nucleation k_+k_2 [53].
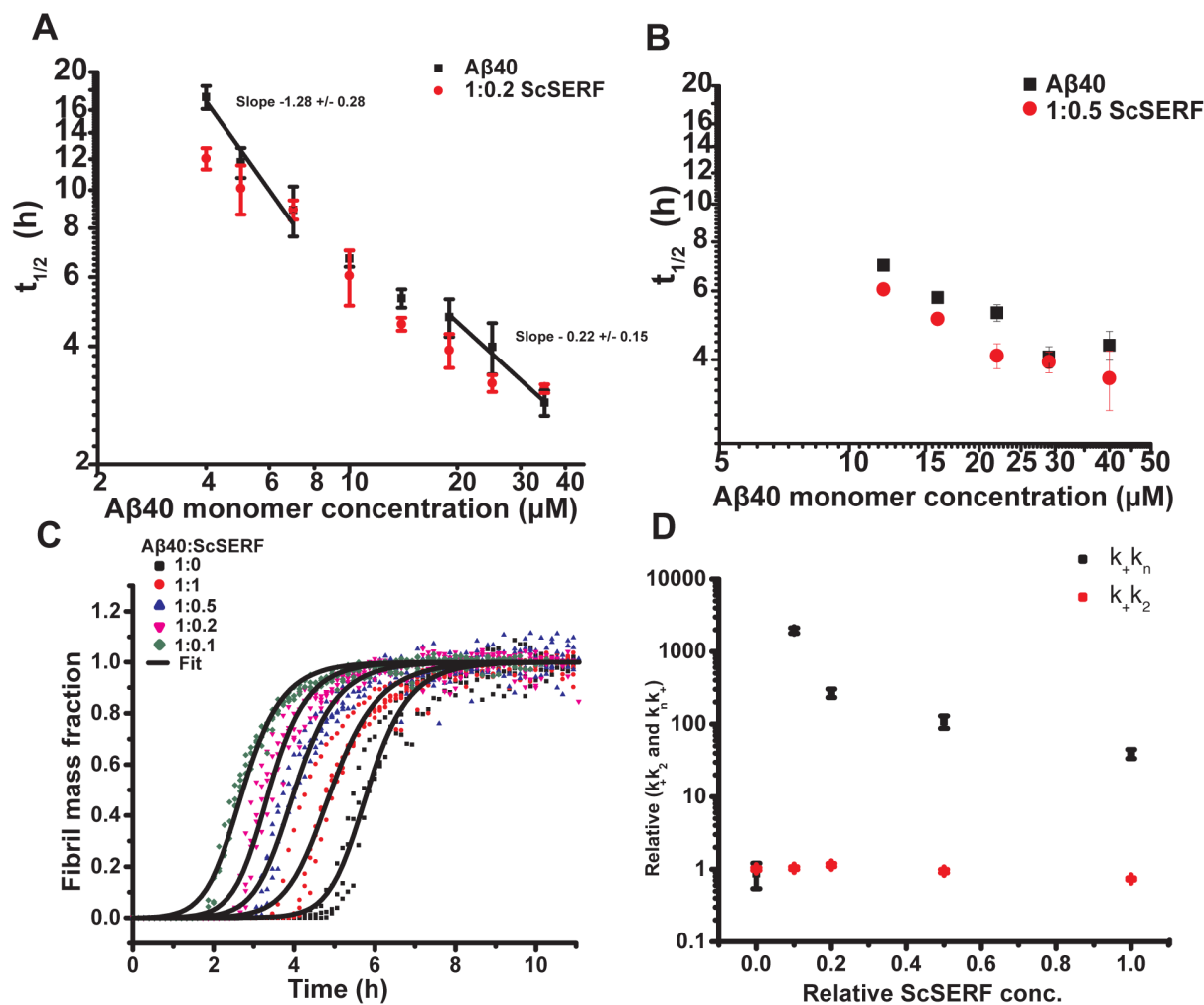
Figure 13: ScSERF accelerates primary nucleation of Aβ40 aggregation.
(A) Double logarithmic plot of average halftime of Aβ40 aggregation in the absence (black) or presence of 1:0.2 Aβ40:ScSERF (red). (B) Double logarithmic plot of average halftime of Aβ40 aggregation in the absence (black) or presence of 1:0.5 Aβ40:ScSERF (red). (C) Fibril mass fraction of 25 μM Aβ40 incubated in the absence (black) or presence of different concentrations of ScSERF. Data were fit with a multi-step secondary nucleation model, with k_+k_n being that combined primary nucleation rate constant and k_+k_2 being the combined secondary nucleation rate, both were used as free fitting parameters. (D) Dependencies of the relative combined rate constants k_+k_n, and k_+k_2 to relative ScSERF concentration obtained from fitting the kinetic data from panel 13 C (Figure adapted after Meinen *et al.,* 2019).

The amyloid assay in the presence of ScSERF was globally fitted with the two rate constants as free fitting parameters, as this procedure allows us to determine changes for all ScSERF concentration at the same time. The fits describe the data for different ScSERF concentrations reasonably well (Fig. 13 C). We attempted to fit of the data with simpler models available through amylofit but none of the models described the data well at all (Appendix Fig. 32)[41]. The rate constant for secondary nucleation k_+k_2 is unchanged in the presence of ScSERF concentrations, while the rate constant for primary nucleation k_+k_n is increased by the addition

of ScSERF (Fig.13 D). The relative change of k_+k_n in comparison to the Aβ40 control is shown in Fig. 14 D. Sub-stoichiometric concentration of ScSERF leads to an over 100-fold increase in primary nucleation rate k_+k_n (Fig. 13 D).

4.2.7 ScSERF accelerates amyloid formation of α-synuclein

The aggregation kinetics of α-synuclein were also monitored by ThT fluorescence. The addition of ScSERF leads to an acceleration of amyloid formation (Fig.14 A). At sub-stoichiometric ratios of ScSERF, the halftime of α-synuclein amyloid formation is reduced from 37 h to around 10 h. In the case of α-synuclein aggregation, we did not observe an inhibitory effect of higher ScSERF concentrations. ScSERF is almost as efficient in accelerating α-synuclein amyloid formation at the low concentration of 20 μM as it is at the high concentration of 200 μM (Fig.14 B).
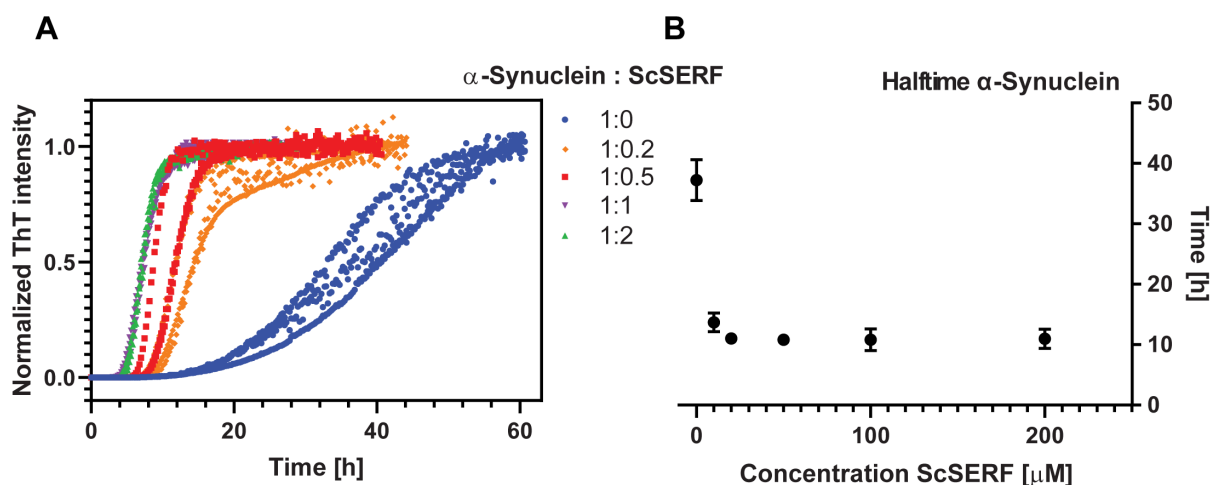
Figure 14: ScSERF accelerates α-synuclein amyloid formation.
(A) Normalized ThT fluorescence of 100 μM α-synuclein incubated in the absence (blue) or presence of different concentrations of ScSERF. (B) Halftimes of α-synuclein were plotted against ScSERF concentration. Assays were conducted with constant shaking at 37 °C in 20 mM NaH_2PO_4, 50 mM NaCl, 200 mM EDTA, pH 7.4 (Figure adapted from Meinen *et al.,* 2019).

In comparison to Aβ40, the amyloid kinetics of α-synuclein are more difficult to quantify as α-synuclein aggregation can take weeks to be complete under quiescent conditions[51]. To obtain amyloid kinetics on a reasonable timescale, the samples in this study were subject to constant shaking at 300 rpm. The process of shaking leads to fragmentation of amyloid fibrils, which makes fragmentation the dominate reaction step for amyloid fibril formation. There is no unified model for α-synuclein aggregation at neutral pH, some characterizations have been

studied at mildly acidic pH[52]. We utilize self-seeded data to distinguish between primary and secondary nucleation processes at neutral pH.

4.2.8 α-synuclein amyloid fibrils in the presence of ScSERF

The α-synuclein fibrils formed in the presence of ScSERF were monitored by transmission electron microscopy (Fig. 15). The overall fibril morphology appears to be unchanged in the presence of ScSERF, which matches the observation made in the literature[90]. The α-synuclein fibrils formed in the presence of ScSERF however appear to be a bit shorter and more clumped together, this might be result of fibril fragmentation during the shaking and agitation of the samples (Fig. 15 C, D).
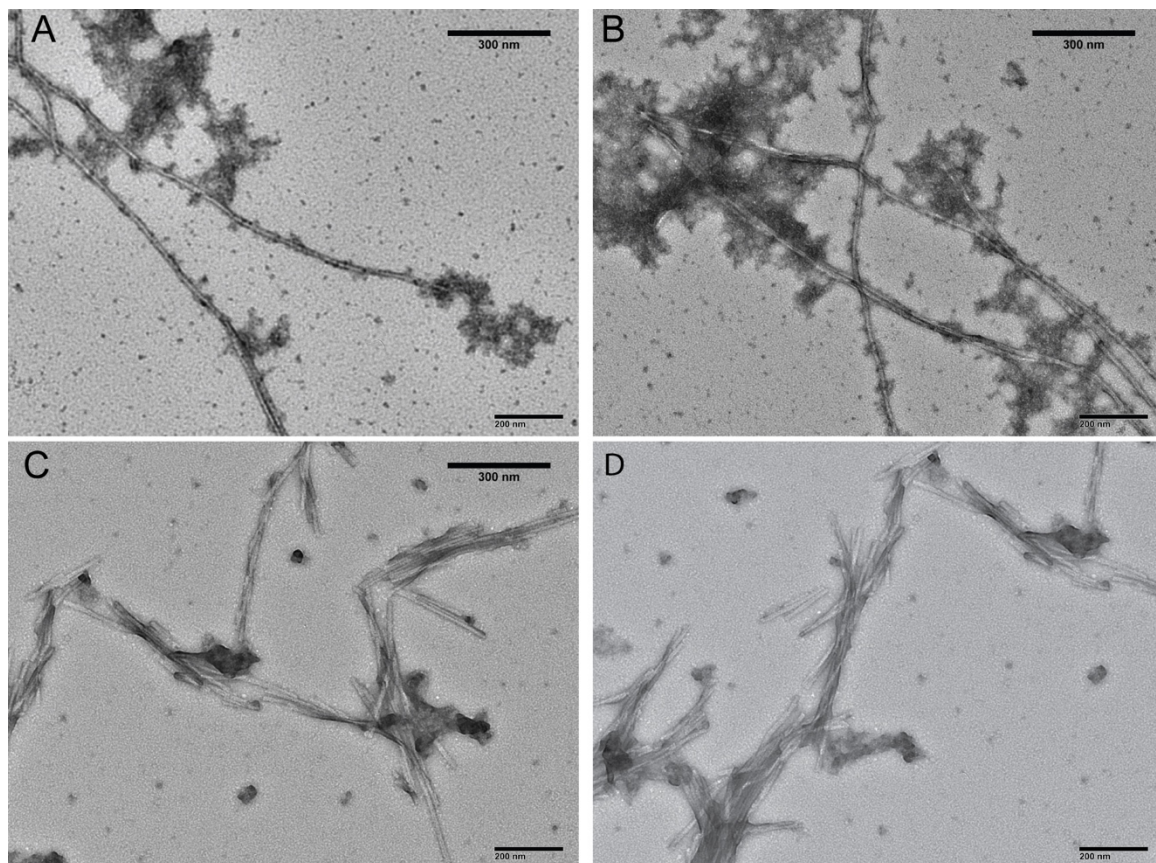
Figure 15: TEM characterization of α -synuclein fibrils +/- ScSERF.
(A, B) Negatively-stained TEM images of 200 μM α-synuclein after completion of the ThT assay. (C, D) Images of 200 μM α -synuclein incubated with 100 μM ScSERF (Figure adapted after Meinen *et al.,* 2019).

4.2.9   ScSERF has no perceptible effect on self-seeded amyloid formation

In the previous described unseeded amyloid kinetic experiments, the reaction is initiated using pure monomeric protein. In the case of a self-seeded experiment, a seed of pre-formed aggregates and fibrils are added at the start of the reaction. The seeds bypass the initial step of primary nucleation, leading to a change of reaction behavior. The monomeric amyloid proteins can attach to the fibril seeds and start the elongation process or undergo surface catalyzed secondary nucleation to form new fibril seeds. The amyloid formation curves conducted in the presence of seeds lack a lag-phase. To test if ScSERF influences elongation or secondary nucleation, ScSERF was added to self-seeded experiments for Aβ40 and α-synuclein. We observed that the slope of the aggregation curves seen at low seed concentrations (Fig. 16 A, C) is less steep, than in the reactions that used higher seed concentrations (Fig. 16 B, D). As expected, for self-seeded experiments, the lag phase cannot be observed (Fig. 16 A-D).
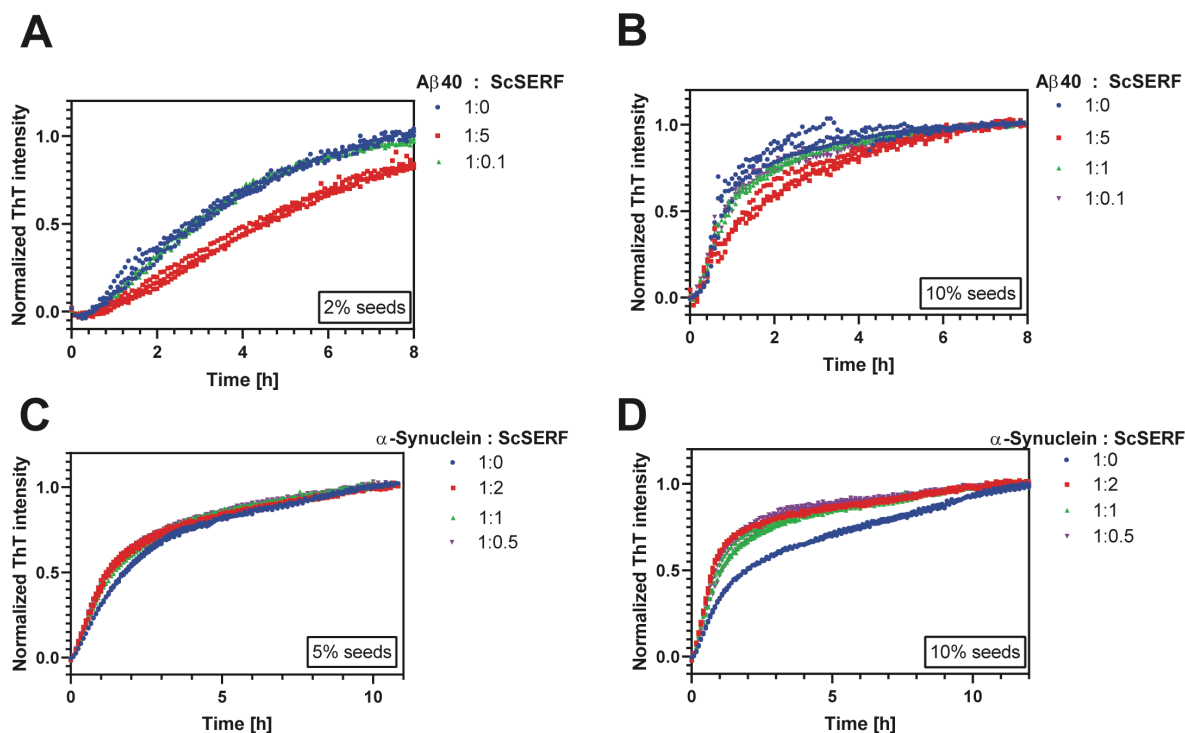
Figure 16: ScSERF has minimal effect on self-seeded amyloid kinetics.
(A) Normalized ThT fluorescence of 25 μM Aβ40 self-seeded with 0.5 μM pre-formed Aβ40 fibrils (2 % seeds) incubated in the absence (blue) or presence of different concentrations of ScSERF. (B) Same as in (A), but self-seeded with 2.5 μM pre-formed Aβ40 fibrils (10 % seeds). (C) Self-seeding assay with 100 mM α-synuclein and 5 % seeds. (D) Self-seeding assay with 100 μM α-synuclein and 10 % seeds. In all experiments, assays were conducted under quiescent conditions at 37 °C (20 mM NaH$_2$PO$_4$, 50 mM NaCl, 200 μM EDTA, pH 7.4, 25 μM ThT). (Figure adapted from Meinen *et al.*, 2019)

ScSERF addition to self-seeded Aβ40 assay showed no increase in the rate of amyloid formation (Fig. 16 A-B). A molar-excess of ScSERF appears in this one case to slow the reaction seen at low seed concentration (Fig. 16 A), however, this was not routinely observed. In the case of the α-synuclein reaction conducted the presence of ScSERF the kinetics were not affected in a significant manner (Fig, 16 C-D). This result supports our finding that ScSERF primarily affects primary nucleation of Aβ40 and also suggested that ScSERF effects α-synuclein in the early stages of amyloid formation.

4.2.10 ScSERF binds to amyloid fibril surface

It had been reported that SERF1a remains in the soluble fraction after it is used to accelerate α-synuclein amyloid aggregation[90]. To determine the fate of ScSERF at the end of the amyloid aggregation reaction, the insoluble and soluble fractions were separated by centrifugation and analyzed by SDS-PAGE. It was observed that both amyloid proteins Aβ40 and α-synuclein were in the insoluble fraction, whereas almost all of the ScSERF protein was in the soluble fraction (Fig. 17 C, E). However, a small amount of ScSERF was detected in the insoluble fraction.

As previously described, we could not determine any changes of the morphologies of amyloid fibrils in the presence of ScSERF, making it unlikely that ScSERF is integrated into amyloid fibrils. To follow up this observation, we investigated whether ScSERF binds to pre-formed amyloid fibrils. To monitor the binding, a cysteine mutant of ScSERF A63C was generated via site-directed mutagenesis and the introduced cysteine was site-specifically labeled with AlexaFluor532, a dye that can be easily visualized in fluorescence anisotropy experiments. We chose to do fluorescence anisotropy because it is sensitive to changes in particle size. AlexaFluor532-labeled ScSERF (AF532 ScSERF) was titrated with pre-formed Aβ40 or α-synuclein fibrils and the change in fluorescence anisotropy was monitored. The fluorescence anisotropy signal for AF532 ScSERF will increase if a complex is formed[127]. The addition of pre-formed Aβ40 fibrils resulted in an increased fluorescence anisotropy signal (Fig. 17 A) indicating that a complex is indeed formed. The addition of unlabeled ScSERF to the complex of pre-formed Aβ40 fibrils and ScSERF resulted in a decreased anisotropy signal almost to the same level seen for free ScSERF, indicating that binding is reversible (Fig. 17 B).
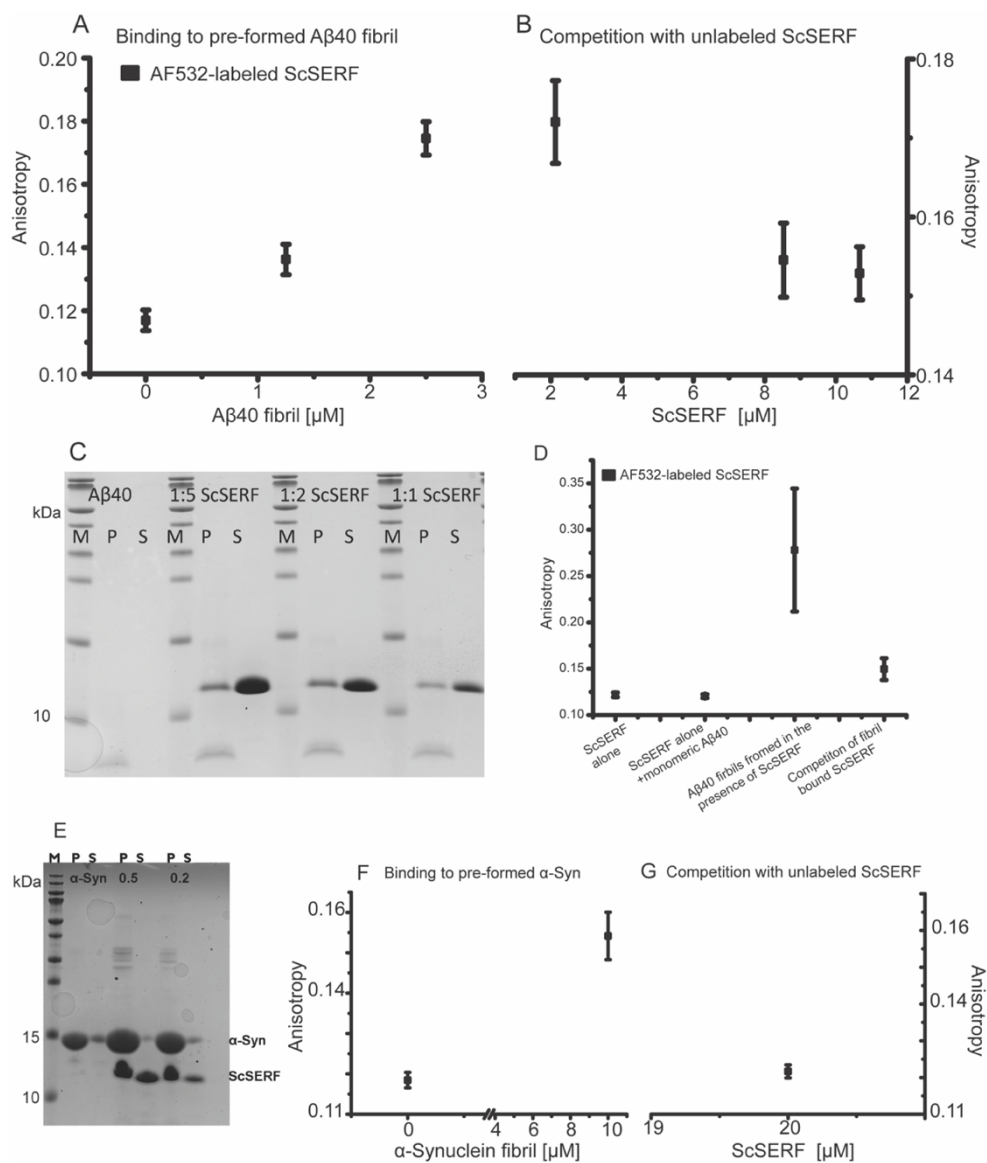
Figure 17: ScSERF interacts with per-formed Aβ40/α-synuclein fibrils.
(A) Fluorescence anisotropy change of AF532-labeled ScSERF upon addition of pre-formed Aβ40 fibrils. (B) Change in anisotropy upon competition with unlabeled ScSERF. Titration was performed at 25 °C in 20 mM NaH$_2$PO$_4$, 200 μM EDTA, pH 7.4. (C) SDS-PAGE analysis of soluble and insoluble fractions of 25 mM Aβ40 aggregation at the plateau of aggregation in the presence of different concentrations of ScSERF: 125 μM (1:5), 50 μM (1:2), and 25 μM (1:1); M: marker, P: pellet, S: soluble fraction. (D) AF532-labeled ScSERF is not integrated into Aβ40 fibrils. Plots show fluorescence anisotropy change of AF532-labeled ScSERF upon addition of monomeric Aβ40, after incubation with Aβ40 for 72 h at 37 °C, and when competed against with unlabeled ScSERF (20 mM NaH$_2$PO$_4$, 200 μM EDTA, pH 7.4, 25 μM ThT). (E) SDS-PAGE analysis of soluble and insoluble fractions of 100 mM α-synuclein aggregation for different ratios of α -synuclein:ScSERF (1:0, 1:0.5, and 1:0.2); M, P, and S same as in (C). (F,G) Fluorescence anisotropy change of AF532-labeled ScSERF upon addition of pre-formed α-synuclein fibrils (F) and when competed against with unlabeled ScSERF (G). (Figure adapted after Meinen *et al.,* 2019)

When AF532 ScSERF was co-incubated with Aβ40 during fibril formation, some of the ScSERF was found to be bound to the fibrils as indicated by the high anisotropy signal, the addition of unlabeled ScSERF in this case resulted also in a decrease of anisotropy signal (Fig. 17 D). These results indicate that ScSERF is not irreversibly integrated into fibrils, but instead is reversibly associated with the surface of Aβ40 fibrils.

The same set up was used to investigate the binding of ScSERF to α-synuclein fibrils. The addition of ScSERF to pre-formed α-synuclein fibrils resulted in an increase in anisotropy. The addition of unlabeled ScSERF resulted in competition with labeled AF532 ScSERF for binding (Fig. 17 F, G). In summary, for both Aβ40 and α-synuclein, ScSERF can reversibly bind to amyloid fibrils, but it does not permanently integrate into these fibrils.

4.2.11 ScSERF binds monomeric Aβ40 and α-synuclein

To determine if ScSERF can bind to monomeric Aβ40 and α-synuclein we are utilizing fluorescence anisotropy. Aβ40 was labeled with AlexaFluor532 at its primary amine group. The labeled fraction of AF-532 Aβ40 was isolated by size exclusion chromatography. ScSERF was titrated into labeled AF-532 Aβ40, the increase in fluorescence anisotropy upon addition of ScSERF indicates binding of ScSERF to Aβ40. The resulting saturation binding curve was fitted and a dissociation constant K_d of 32 μM was obtained (Fig.18 A). We tested ScSERF binding and performed a fluorescence anisotropy titration where α-synuclein was titrated into AF532-labeled ScSERF. The increase in anisotropy was fitted to a binding isotherm that determined a K_d of 9 μM for the binding between ScSERF and α-synuclein (Fig. 18 B). Falsone et al. showed that human SERF1a binds to α-synuclein with a comparable K_d value of 8 μM[90]. We used sedimentation velocity analytical ultracentrifugation to determine that all three proteins were monomeric under the conditions used for the titration experiment.

A

B
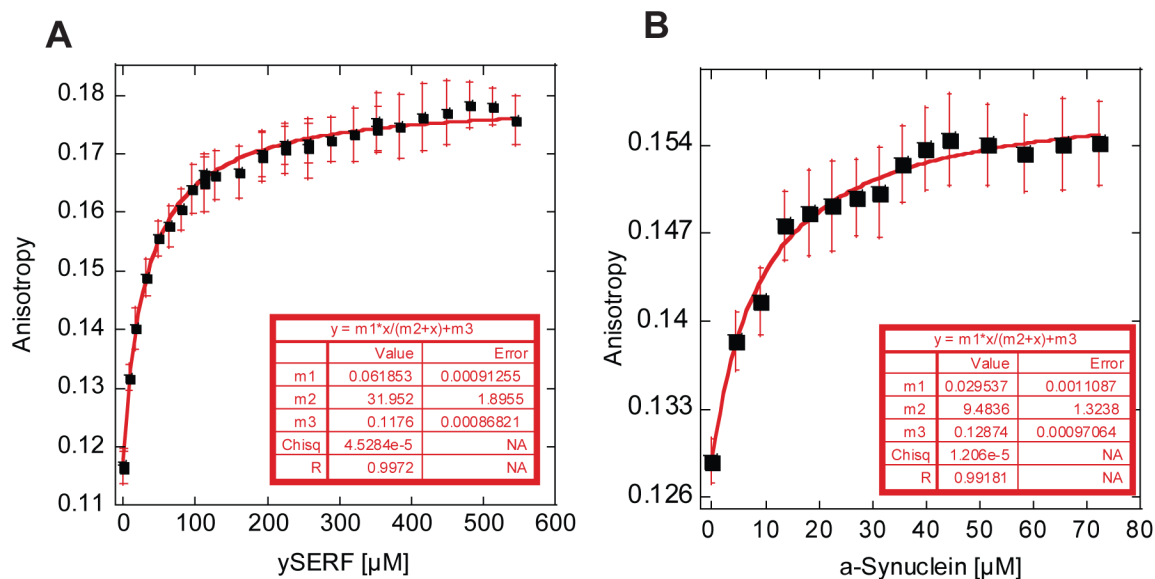
Figure 18 Binding of ScSERF to monomeric Aβ40/α-synuclein.
(A) Increase in fluorescence anisotropy upon titration of ScSERF into monomeric AF532-labeled Aβ40. The equilibrium binding constant (K_d) was determined to be 31.9 ± 1.89 μM. Titration was performed at 25 °C in buffer containing 20 mM ammonium acetate, pH 7.4. (B) Increase in fluorescence anisotropy upon titration of α-synuclein into AF532-labeled ScSERF. The equilibrium binding constant (K_d) was determined to be 9.48 ± 1.32 μM (Figure adapted after Meinen *et al.*, 2019).

The sedimentation velocity experiment showed only one species for all three proteins under the used conditions (Fig. 19). The estimated molecular weight from the analysis indicated, that all proteins are monomeric. A pseudo 3D plot shows the sedimentation coefficient S vs. the frictional ratio f/f0 [111]. The frictional ratio f/f0 is the ratio between the experimental observed frictional coefficient of a molecule vs. the theoretical determined frictional coefficient of an ideal sphere with the same molecular weight. The frictional ratio of an ideal sphere would be 1.0. For global proteins, frictional ratios of 1.1 to 1.35 have been observed[111,128,129]. The frictional ratio f/f0 for α-synuclein is 2.1, which indicates that α-synuclein has an extended structure in solution (Fig. 19 A). Similar observations are made for ScSERF, it shows a frictional ratio of 1.7 (Fig. 19 C) indicating that it too has an extended configuration in solution. This is further evidence that both these proteins are intrinsically disordered with extended structures in solution. Aβ40 appears to be in a comparably more compact state in solution with a frictional ratio f/f0 of 1.3 (Fig. 19 B).
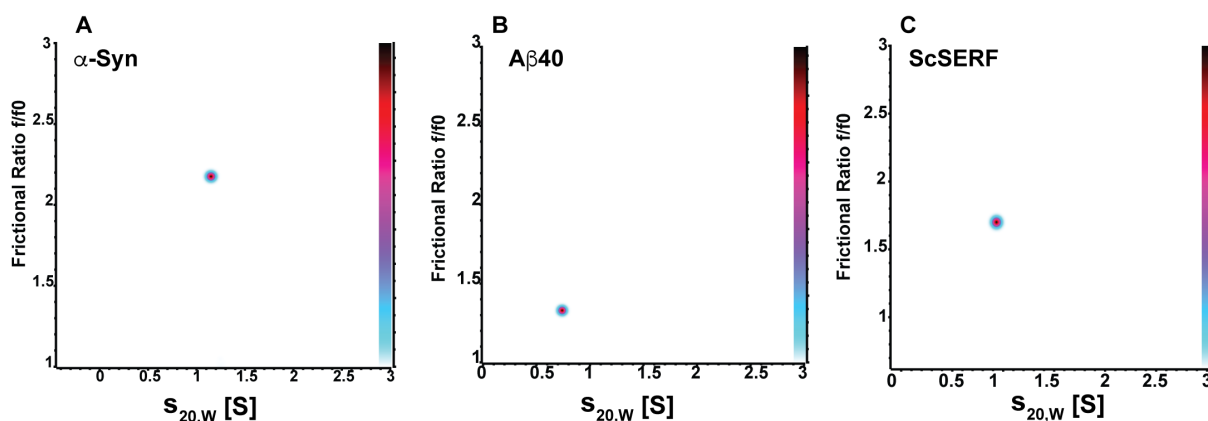
Figure 19: Pseudo-3D plots of 2DSA analysis from sedimentation velocity experiments.
Solute distribution of SV-AUC experiments, plotted is the sedimentation coefficient $S_{20,w}$ against the frictional ratio f/f0. (A) α-synuclein was sedimentation at 58,000 rpm. (B) Labeled AF532-labled Aβ40 was sedimented at 59,000 rpm. (C) ScSERF was monitored at 225 nm and sedimented at 58,000 rpm.

4.3 Structural investigation of early complexes formed between ScSERF and Aβ40/α-synuclein

4.3.1 Solution NMR of Aβ40 with ScSERF

We attempted to determine if there is a particular set of residues that are important for the interaction between ScSERF and Aβ40. Therefore, Aβ40 was recombinantly expressed, isotopically ^{15}N-labeled and purified for use in NMR spectroscopy. The heteronuclear single quantum correlation (HSQC) spectra for Aβ40 has previously been assigned[130]. Unlabeled ScSERF was titrated into ^{15}N-labeled Aβ40 (Fig. 20 A). At equimolar concentration of ScSERF to Aβ40 the signal intensity of most peak signals is decreased by around 20 % (Fig. 20 B). The addition of higher concentration of ScSERF lead to further decrease of some peak intensities to 60 % – 70 % in comparison to the starting signal. The overall decrease in signal upon the addition of ScSERF could be due formation of NMR invisible complexes or higher oligomeric states of Aβ40. It has been shown that the transition of Aβ40 monomers into higher oligomeric species leads to substantial line boarding and a disappearing of signals in the HSQC spectra[131]. Only small chemical shift changes for some Aβ40 residues were observed (Fig. 20 C). The largest change was observed for Valine 24, which is in the linker region between the two hydrophobic patches ([17]LVFFA[21]) and the C-terminus in the Aβ40 sequence. Some shifts were also detected in residues in C- and N-terminal region of Aβ40. Although the data indicates that binding is occurring between Aβ40 and ScSERF, we cannot identify one

strong binding site. The data suggests that ScSERF:Aβ40 complex is flexible and the signal disappearance is caused by conformational exchange in the complex resulting in a change in NMR signal intensity, probably due to a shift towards the intermediate exchange regime. This is not surprising because both proteins can be characterized as intrinsically disordered proteins.
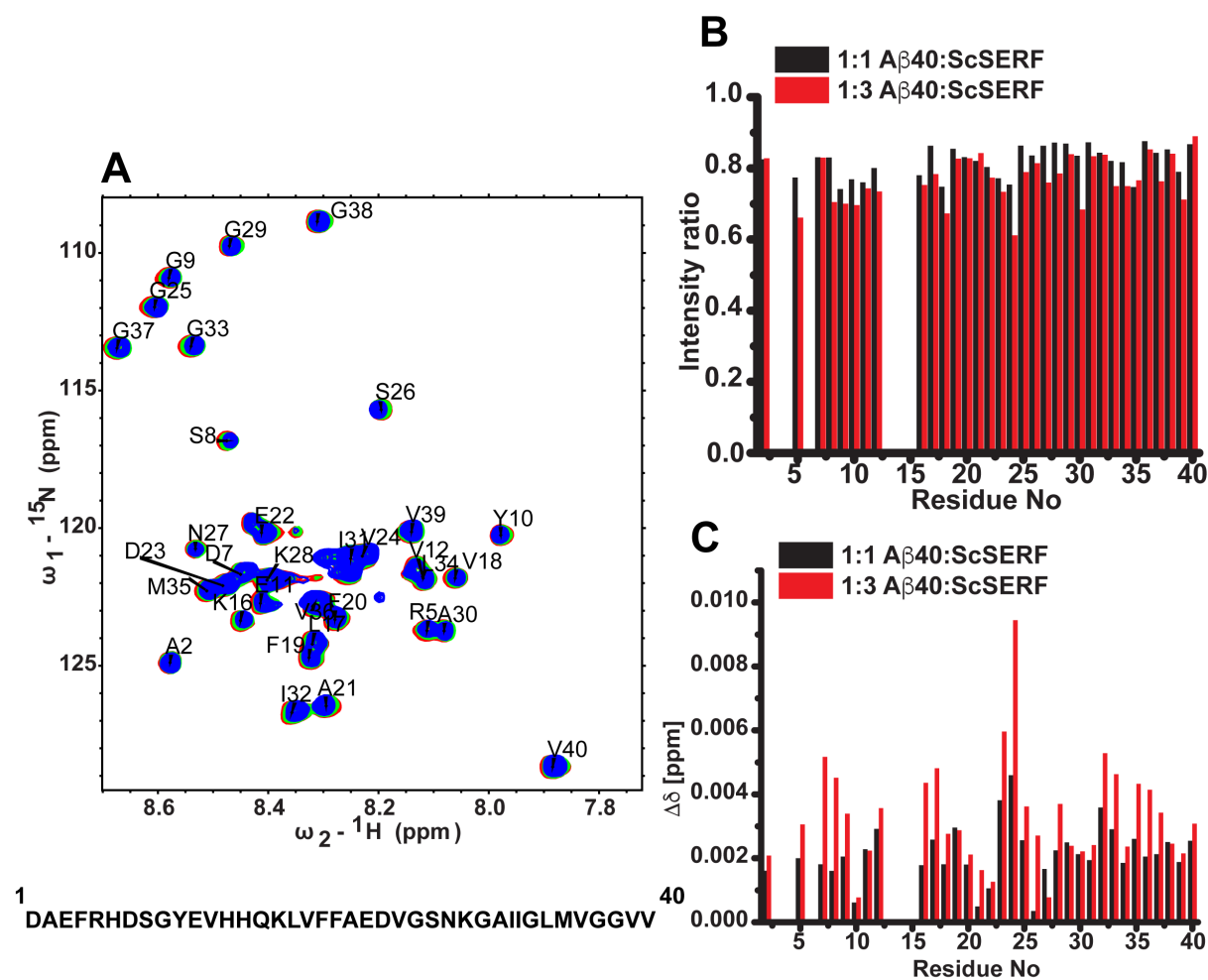
Figure 20: Changes in HSQC spectra of [15]N Aβ40 upon titration of ScSERF.
HSQC Spectra of [15]N Aβ40, Aβ40 red (116 μM), green 1:1 Aβ40:ScSERF (118 μM), blue 1:3 Aβ40:ScSERF (350 μM), below spectra shown is Aβ40 amino acid sequence. (B) Relative change in intensity to Aβ40 sample after integration of signal intensity in each HSQC spectra. (C) Change in average chemical shift (Δδ) in Aβ40 upon addition of ScSERF. Aβ40 assignments from BMRB code: 17764.

4.3.2   Characterization of ScSERF:Aβ40 and α-synuclein complexes via Native IM-MS

The data indicates that ScSERF interacts with monomers of Aβ40/α-synuclein and affects the lag phase of Aβ40 and α-synuclein amyloid formation. The dye Thioflavin T can be used to monitor the kinetics. It binds to β-sheet rich conformation as present in the cross β -sheet structure formed in amyloid fibrils [132]. However, the conformational change and formation of transient species that occur during the lag phase of the fibrillation kinetics are unfortunately ThT-invisible. To monitor the early events in amyloid formation ion mobility, native mass spectrometry was employed. Native ion-mobility mass spectrometry (IM-MS) is an analytical technique to analyze proteins and protein complexes in the gas phase preserving the native state and non-covalent protein-protein interactions present in solution[133].

IM-MS experiments provide structural information on protein complexes in terms of charge state distributions (CSDs) and collision cross section (CCS) distributions[133]. Natively folded, structurally homogeneous proteins typically ionize in a specific number of charge states directly related to the surface area of the protein. For reference, native ubiquitin, an 8.6 kDa protein standard typically has 3-4 charge states, typically 4+ to 6+. In contrast intrinsically disordered proteins display a broader and higher range of CSDs and CCS distributions[134,135].

4.3.3   ScSERF is elongated and intrinsically disordered in IM-MS

The measurement of m/z, the drift time of the ions and their intensity results in a robust three-dimensional output, where the x-axis represent the m/z, the y-axis shows the drift time of the ions and the intensity is presented in the z-axis. We found that ScSERF behaves like a an intrinsically disordered protein with flexible structural properties in the IM-MS experiment. In comparison to the example of native ubiquitin, ScSERF has an unusually broad charge state distribution (11 charge states) from 4+ to 15+, which is indicative of the various structures of ScSERF present in solution prior to the nESI process (Fig. 21 A,B). Furthermore, the lower chare states (5+,6+,7+) have an extended drift time distribution in the ion mobility dimension (Fig. 21 C). An extended conformation of ScSERF was also observed in solution, as indicated the frictional ration f/f0 of 1.7 measured by sedimentation velocity analytical ultracentrifugation experiments (Fig. 19 C). Broad drift time distributions within one charge state represents a subset of ScSERF conformers which ionize with the same set of charges due

to having similar surface areas, but interact differently with the drift gas and as a result show different arrival times (Fig 21 C). The lower chare states (5+,6+.7+) have multiple arrival time distributions, whereas the higher charge states (8–15+) show only one structural conformation. An analysis of the arrival time distribution (ATDs) of the 11 charge states gives information on the number and range of conformations in one charge state (Fig. 21 C). The ATDs were fitted to multiple Gaussian functions and defined discrete conformers of ScSERF that range in CCS from 9 to 22 nm^2 were calculated. The relationship between molecular weight and CSS follows a power law correlation, however some of the extended conformers of ScSERF are nearly 2- to 3-fold larger than expected for 7,949 Da protein[133].

We also observed a dimeric species of ScSERF in the native IM-MS experiment. The ScSERF dimer has three charge states (10+, 9+, 8+). ScSERF dimers have collision cross section of 13-17 nm^2 (Fig. 21 C). In contrast to the heterogenous population of ScSERF monomer the dimeric species has a relatively compact CCS value. We did not observe a dimeric population of ScSERF in SV-AUC experiments.

4.3.4 ScSERF forms structural diverse complexes with Aβ40

ScSERF shows a high ionization efficiency, which results in a very high signal intensity, we found that an equimolar ratio of ScSERF and Aβ40 resulted in the best signal to noise ratio for the IM-MS experiment. We analyzed the ScSERF and Aβ40 complexes via IM-MS that result from the incubation of equimolar ratio of ScSERF to Aβ40. In this sample we detected, as expected, monomeric ScSERF, dimeric ScSERF, monomeric Aβ40 and a low intensity signal of dimeric Aβ40. We detected complexes with three different stoichiometries between ScSERF and Aβ40 a 1:1 complex of ScSERF:Aβ40 , 2:1 ScSERF:Aβ40 , 1:2 ScSERF:Aβ40 (Fig. 21 A-C).

To quantify the percentage of complexes formed under the investigated conditions we assumed that Aβ40 and Aβ40 containing complexes have a comparable ionization behavior. In the sample of equimolar 10 μM ScSERF and Aβ40 we detected that about ~33% of Aβ40 is bound to ScSERF. We further estimated the dissociation constant K_d between ScSERF and Aβ40 using IM-MS to be 10 ± 2 μM (Fig. 21 D) this is in the same range as the K_d determined in solution of 32 μM (Fig. 18 A). Based on these measured K_d values we would predict about 24 % to 50 % of complexes should be present when both proteins are at a concentration of 10 μM, which is in the range of about ~33 % we experimentally measured for the 1:1 complex.

The 1:1 complex is the most abundant complex with over 90 % of protein in complex being in a 1:1 complex.
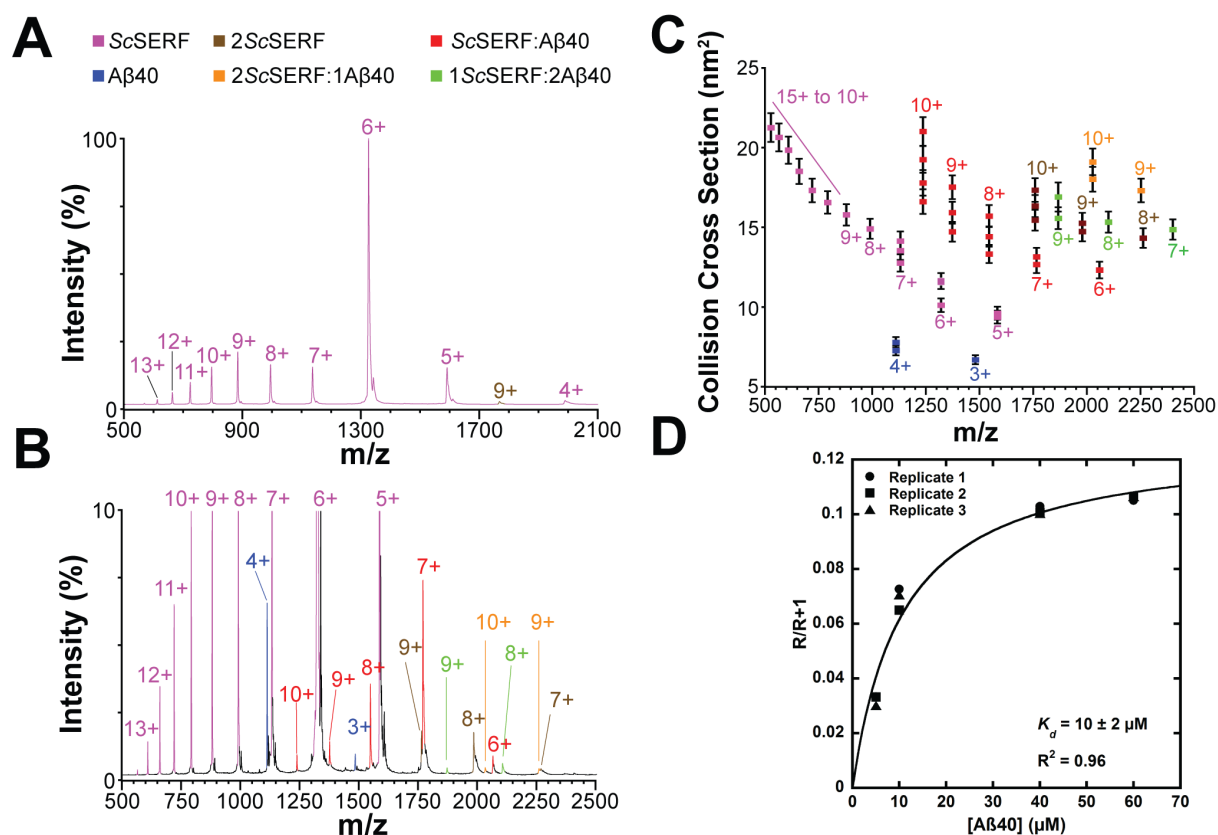
Figure 21: Analysis of ScSERF interacting with Aβ40 using nESI IM-MS.
(A) Native mass spectrum of Aβ40 and ScSERF at 10 μM. The measured monoisotopic mass of 7945 ± 1 Da is in close agreement with the average sequence mass of ScSERF at 7949 Da (UniProtKB ID Q3E7B7). The 4–13+ charge states of ScSERF monomer (magenta) and the 9+ charge state of ScSERF dimer (brown) are labeled. (B) 25 μM ScSERF and Aβ40 were incubated together. Samples were diluted to 10 μM each and analyzed by native IM-MS. The mass spectrum shows charge states corresponding to 6 different complexes as indicated by the color key at the top of the figure. The spectrum is cropped to 10 % relative intensity to enlarge the low intensity signals correlating to ScSERF:Aβ40 complexes that are suppressed by the high intensity of ScSERF. (C) The arrival time profile of each ion was extracted and fit to Gaussian functions. The Gaussian centroids are converted to collision-cross sections (CCSs) and plotted vs. m/z. The error bars are least squares errors, which account for calibration error as well as the standard deviation for at least three samples. (D) Titration 2 μM ScSERF was titrated with 5, 10, 40, and 60 μM Aβ40 to determine the dissociate on constant (K_d) of ScSERF binding to monomeric Aβ40. At concentrations higher than 60 μM, Aβ40 aggregated and thus interfered with accurate measurement of the amount of 1:1 ScSERF:Aβ40 complex. The fraction of ScSERF was determined from intensities of bound and unbound species in individual mass spectra. The fraction of bound ScSERF was plotted vs. Aβ40 concentration for 3 replicate measurements. The data were fit using a quadratic function described previously for measuring K_d by MS[117]. The data from 3 replicate measurements was fit with an R^2 of 0.96, and a K_d of 10 ± 2 μM was obtained (Figure adapted after Meinen *et al.,* 2019).

Monomeric Aβ40 typically ionizes in 2-3 charge states (4+ to 2+) [61], monomeric Aβ40 appears to be more compact in comparison to monomeric ScSERF. Analytical ultracentrifugation of monomeric Aβ40 resulted in a frictional ratio of 1.3 matching the observation of a more compact conformation in solution and the gas-phase (Fig. 19 A).

In contrast to monomeric Aβ40, the 1:1 complex between ScSERF and Aβ40 occupy extended conformations with collision cross sections (CCSs) ranging from 12 to 22 nm^2 indicating that Aβ40:ScSERF complex is dominated by extended conformation.

Furthermore, the broad charge state distribution (CSD) of the complex shows that multiple ScSERF conformations can interact with possibly multiple conformations of monomeric Aβ40. It has been observed that Aβ40/42 monomers become more compact in oligomeric tetramer structure[61], but not much is known about the early conformational changes occurring in Aβ40 amyloid. In that context it is interesting and novel, that the complex conformation leads to extended structures rather than more compact conformations.

The 1:2 and 2:1 complex between ScSERF and Aβ40 also show broad collision cross sections, indicating that the higher oligomeric complexes also have extended structures and multiple conformations. The complexes have measured collision cross sections that are nearly 2-fold above the expected CCS for globular protein ions in the respective size range of predicted from the molecular weight (Fig. 21 C). This supports the idea, that ScSERF keeps its extended conformation in all complexes with Aβ40.

4.3.5 Monitoring ScSERF:Aβ40 complexes over a time period via IM-MS

After we identified the complexes formed between Aβ40:ScSERF we followed the time course of Aβ40 amyloid formation in the presence of ScSERF via native IM-MS. An equimolar ratio of Aβ40:ScSERF was incubated in the same conditions used for the kinetic measurements, samples were taken every 30 minutes and analyzed via IM-MS. We monitored the intensity of each species present at each time point. The distribution of ions detected did not change during the time course (Fig. 22 A). After 360 minutes into the experiment, the Aβ40 signal disappears completely. This is likely due to the formation of insoluble aggregates, that do not ionize and therefore cannot be analyzed by IM-MS. The ScSERF signal is stable even after 24 h of incubation, providing a good indication that ScSERF stays soluble during the reaction.

An analysis of the collision cross section distribution in the 1:1 Aβ40:ScSERF complex over time showed some interconversion in between states, but no accumulation of a particular state over the monitored time period (Fig. 22 B).
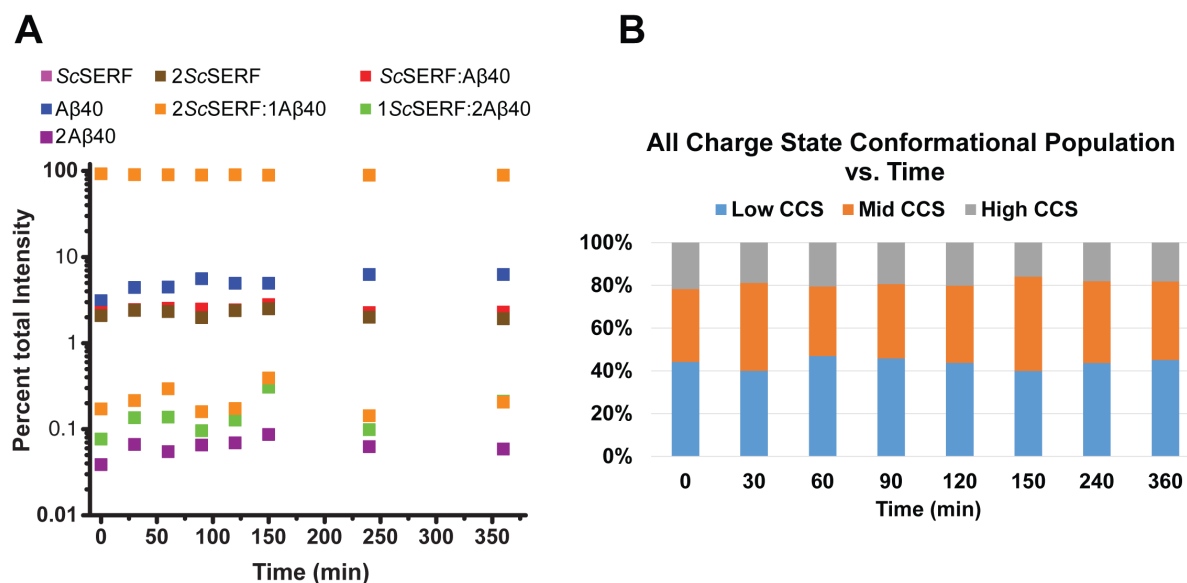
Figure 22: Analysis of ScSERF interacting with Aβ40 over time.
Equimolar ratio of Aβ40:ScSERF were incubated at 37 °C in Corning, #3881 plate. Samples were taken at indicated time points and immediately analyzed by nESI-IM-MS. (A) Normalized intensity of individual complexes observed over time. (B) From the IM-MS data, relative amount of different of 1:1 ScSERF:Aβ40 complex was monitored vs. time. The occupancy of each conformational state was determined by calculating the area under the Gaussian peaks fit to the raw data during collision cross section analysis (Figure adapted after Meinen *et al.,* 2019).

4.3.6   ScSERF and α-synuclein form heterogenous elongated complexes

In the IM-MS samples, α-synuclein exists in both monomeric and dimeric states. Monomeric α-synuclein spanned collision cross sections (CCSs) from 20-30 nm^2, while for dimeric α-synuclein CCSs ranged from 30 -50 nm^2 (Fig. 23 B-D). In contrast to monomeric Aβ40, α-synuclein alone shows a broad arrival time distribution. The broad collision cross section for α-synuclein are consistent with an intrinsically disordered protein of that size. We determined a frictional ratio f/f0 of 2.1 for α-synuclein in solution via analytical ultracentrifugation (Fig. 19 C), which matches the extended structure observed in the IM-MS (Fig. 23 B). We did not observe dimeric α-synuclein in the SV-AUC experiment.

Samples containing equimolar concentrations of α-synuclein and ScSERF showed complexes in four different stoichiometries of 1:1, 1:2, 2:1, and 2:2 ScSERF:α-synuclein (Fig. 23). For α-synuclein and ScSERF we observe the higher stoichiometry complexes of 2:2, that has not been observed for ScSERF and Aβ40. Based on the intensity of the complexes, we find about ~40 % of α-synuclein is bound to ScSERF in the 1:1 complex. Based on the determined dissociation constant in solution we would expect about 52 %. of protein in complex. This suggest that the dissociation constant determined in solution qualitatively matches the complexes we detect in the IM-MS experiment. The complexes between ScSERF and α-synuclein also show above average collision cross section and broad charge state distribution (Fig. 23 B). The 1:1 complex have collision cross sections ranging from 30 to 50 nm^2, the 2:1 ScSERF:α-synuclein complex and 1:2 ScSERF: α-synuclein complex have extended collision cross sections from 35 to 55 nm^2 (Fig. 24 C, D). This indicates that both α-synuclein and ScSERF keep their disorder and heterogenous structure in both complexes. Complexes between two flexible and disordered proteins are a new theme emerging in the study of intrinsically disordered proteins, this the first time this has been observed in the context of amyloid formation[5].

The 2:2 complexes have collision cross sections ranging between 30 to 70 nm^2 (Fig. 23 C, D). The larger complexes have CCSs almost 3-fold larger than their molecular weight[133]. In the case of intrinsically disordered proteins larger CCSs are expected, but 3-fold larger CCSs are surprisingly large. Therefore, we can hypothesis that not only in the 1:1 complex, but also in the 2:2 complex ScSERF and α-synuclein are in extended structures.
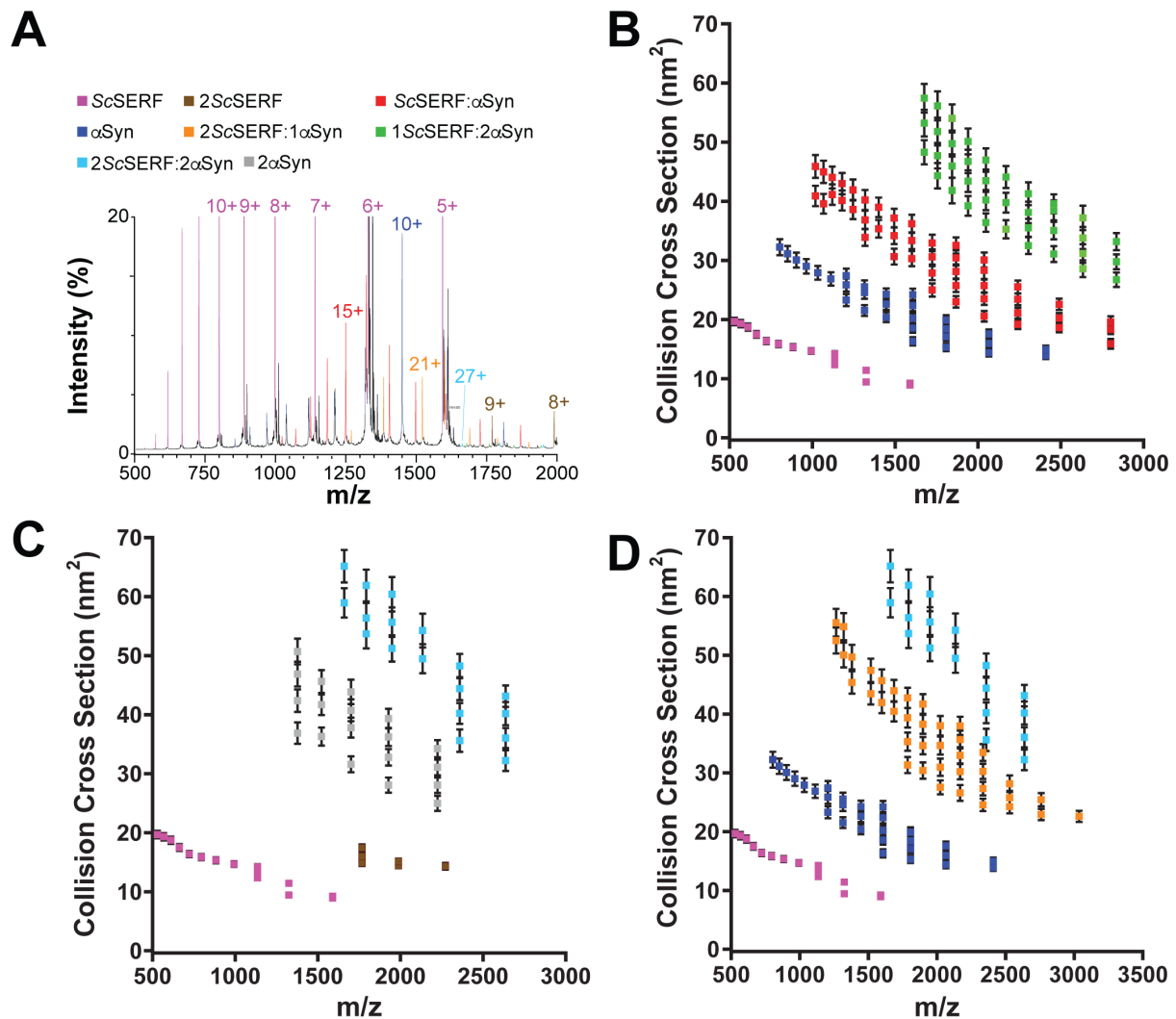
Figure 23: Analysis of ScSERF interacting with α-synuclein using nESI IM-MS.
(A) 25 μM ScSERF and α-synuclein (αSyn) were incubated together. Samples were diluted to 10 μM each and analyzed by native IM-MS. The mass spectrum shows charge states corresponding to 8 different complexes as indicated in the color key at the top of the figure. The spectrum is cropped to 20 % relative intensity to enlarge the low intensity signals correlating to ScSERF:α-synuclein complexes that are suppressed by the high intensity of ScSERF. The m/z range is cropped at 2000 because signals corresponding to complexes beyond m/z = 2000 are << 1% total intensity. These complexes can, however, be isolated and included for CCS analysis. The presence of these complexes is addressed in the CCS vs. m/z plots. (B-D) The arrival time profile of each ion was extracted and fit to Gaussian functions. The Gaussian centroids are converted to CCSs and plotted vs. m/z. The error bars are least squares error, which account for calibration error as well as the standard deviation for at least 3 samples (Figure adapted after Meinen *et al.,* 2019).

Protein complexes in which one or multiple proteins retain flexible, partial or fully disordered regions are classified as fuzzy complexes [24]. The concept of fuzziness in the context of amyloid formation has only been proposed in the context of two prion proteins Ure2p and Sup35p[136,137].

In our data the broad arrival time distributions (ATD) for a range of different stoichiometries between ScSERF and Aβ40/α-synuclein indicates that the concept of fuzzy complexes in early steps of amyloid formation can be expanded to these human disease-related proteins.
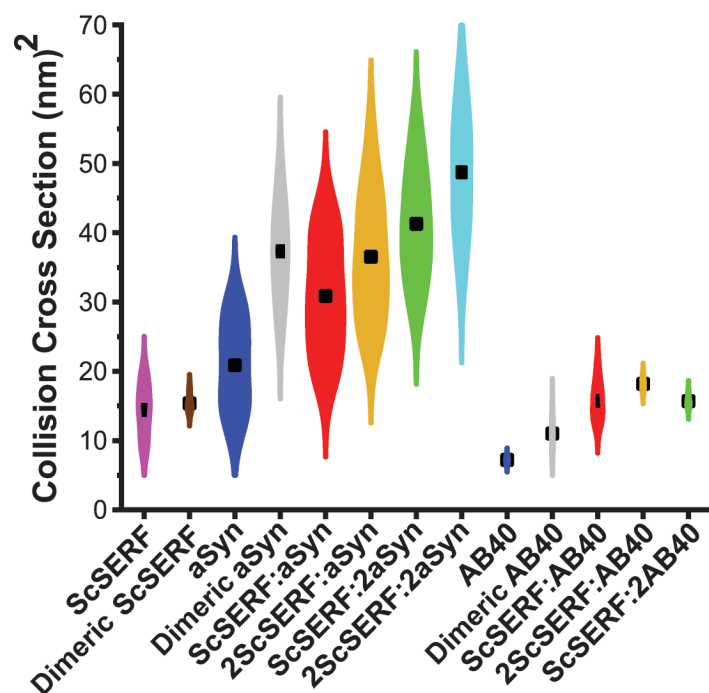
Figure 24: Violin plot of complexes between ScSERF and Aβ40/α-synuclein.
Violin plots of the collision cross section (CCSs) distributions of the three proteins and different ScSERF containing complexes observed in the native IM-MS experiments. Black squares indicate the mean CCS of each complex. The kernel density distributions around the mean are a probability estimation of the number of complexes occupying that CCS bin based on the input set of experimental data (Figure adapted after Meinen *et al.,* 2019).

The broad ATDs observed for all the complexes suggest that multiple ScSERF conformations can bind to various conformations of the studied amyloid proteins and that the resulting complexes are also flexible and dynamic in solution. A plot summarizing the collision cross section of all species observed in the nESI IM-MS experiments is shown in (Fig. 24). The violin plot illustrates, that the observed complexes have extended structures with unusually large CCS values for proteins in this mass range. In the case of ScSERF interaction with Aβ40/α-synuclein the complexes are best described as fuzzy complexes. This is an exciting observation for understanding how modifiers can affect amyloid formation for the human disease-related proteins and Aβ40 and α-synuclein.

4.4 ScSERF effect on amyloid induces toxicity in *S. cerevisiae*

Modifier of aggregation MOAG-4 was discovered as a modifier of amyloid aggregation in *C. elegans*[87]. A deletion of MOAG-4 lead to a decrease in protein aggregation and longer lifespan in *C. elegans*. *S. cerevisiae* has been used to study in vivo aspects of amyloid aggregation for a range of amyloid proteins[138]. We thus decided to investigate if the deletion of the yeast homolog to MOAG-4, ScSERF is beneficial when overexpressing amyloid proteins in vivo. The ScSERF gene (*ydl085c-a*) was deleted from *S. cerevisiae*. Yeast strains with or without the ScSERF gene were transformed with a plasmid that overexpresses Huntington Exon1 (HD1) with different length of polyglutamine residues (25Q or 130Q) under galactose control. It has been shown that polyglutamine toxicity is length dependent the shorter polyQ fragment show minor toxicity effect in serial dilution spotting assay, while longer polyQ length show high toxicity[101]. The addition of galactose induced the expression the amyloid protein. The control growing on plates containing glucose shows that under non-expressing conditions, wildtype and deletion strains both grow similarly (Fig. 25 A). The phenotype was reproduced in the experiment wild type control, where strains overexpressing HD130Q show only one log of growth (Fig. 25 B). The deletion of ScSERF showed no change in survival while overexpressing polyQ compared to the control strain (Fig. 8). In the amyloid system used here, we could not detect a positive or negative effect of the ScSERF deletion in *S. cerevisiae* on amyloid formation.
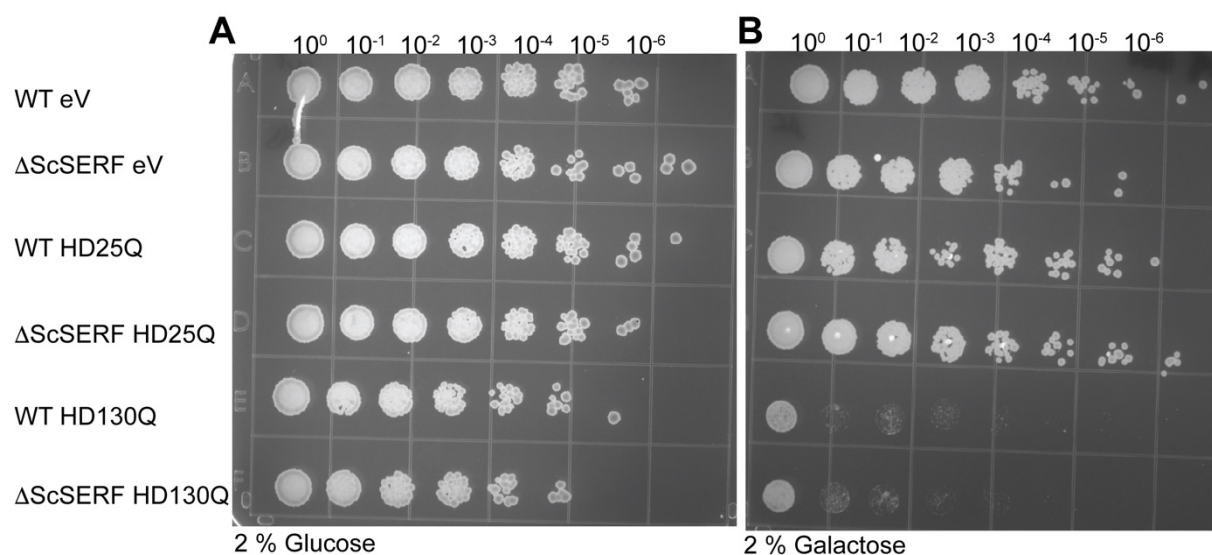
Figure 25: Survival assay of *S. cerevisiae* overexpressing polyQ proteins.
Mid-log phase cells of *S. cerevisiae* expressing pYES2-empty Vector (eV), pYES2 Htt 103Q, Htt 25Q were normalized to OD600nm = 5. Serial dilutions of the cultures were spotted on SD–URA plates containing either (A) 2 % Glucose (B) 2 % Galactose and incubated for 3 days at 30 °C.

α-synuclein is a second amyloidogenic protein that when overexpressed by the strong Gal-promoter can induce toxicity in *S. cerevisiae*. Furthermore, certain mutants in α-synuclein change the aggregation behavior of α-synuclein. The α-synuclein A30P mutation slows down the aggregation process in vivo and leads to less toxicity in comparison to α-synuclein WT, while the A53T and Y125F lead to more toxicity in yeast[139]. Evidence presented in the literature showed that MOAG-4 deletion leads to less aggregated α-synuclein inclusions in *C. elegans*[87].

Plasmid's overexpressing α-synuclein were transformed into *S. cerevisiae* strains and the toxicity was assayed in survival assays. Here, the wild type strains followed the published pattern of toxicity (Fig. 26). The deletion of ScSERF had no impact on the survival of *S. cerevisiae* in comparison to the WT yeast (Fig. 26). It appears that in *S. cerevisiae* the deletion of ScSERF does not lead to an improvement in survival. In other words the yeast ScSERF deletion does not give similar results as the phenotypes observed for *C. elegans* and the human cell culture model[87].
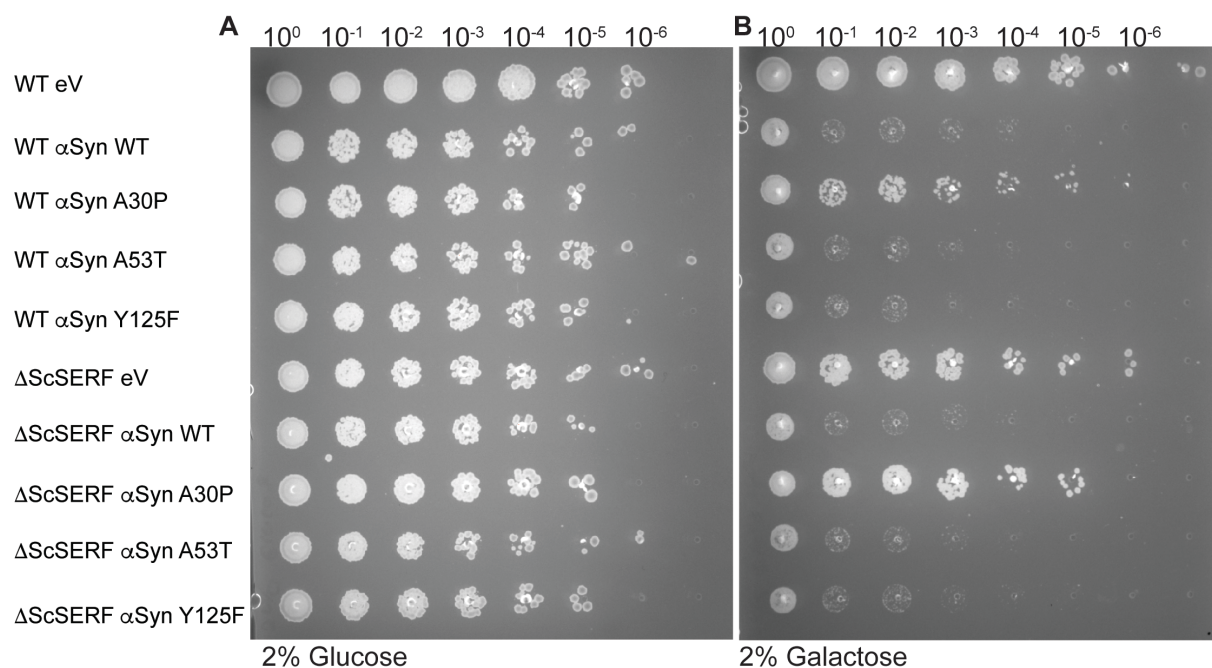
Figure 26: Survival assay of *S. cerevisiae* overexpressing α-synuclein.
Mid-log phase cells of *S. cerevisiae* expressing pRS426 Gal1 empty Vector (eV) or variants of α-synuclein were normalized to $OD_{600nm} = 5$. Serial dilutions of the cultures were spotted on SD –URA plates containing either (A) 2 % Glucose (B) 2% Galactose and incubated for 3 days at 30 °C.

5   Discussion

In this thesis I for the first time characterized the *S. cerevisiae* SERF homologue YDL085C-A termed as ScSERF.

5.1   ScSERF is an intrinsically disordered protein

Protein structures solved by crystallography account for the highest share of structures in the protein database. Unfortunately, this method biases the observed protein conformation towards folded states, that improve crystal packing. Therefore, the structure and importance of intrinsically disordered regions and intrinsically disordered proteins have been underrepresented and underestimated. The generated model for ScSERF was generated by using NMR data, a technique ideally suited to collect structural information of dynamic proteins.

ScSERF shows the propensity to form a α-helical secondary structure at low temperature (4 °C) with a transition to an unstructured state at higher physiologically relevant temperatures (30 °C - 37 °C) (Fig. 8). The HSQC spectra of ScSERF could be assigned and the ^{13}Cα/Cβ secondary chemical shifts were analyzed using TALOS[119]. The generated restraints were used to generate a CS-Rosetta model for the low-temperature data. This model agrees with the NMR structure ensemble published for MOAG-4 that was also generated at low temperature (4 °C)[91].

The similarity between our model and the published MOAG-4 structure is consistent with the observation that the N-terminal region of SERF has the highest sequence conservation across species, suggesting that maintaining disorder of that region may be essential for function throughout evolution.

The analysis of ^{13}Cα/Cβ secondary chemical shifts for the human SERF1a by Merle et al., shows that SERF1a has the propensity to adopt α-helical structures in a short N-terminal (residues 5-15) and a long C-terminal segment (residues 35-60)[140], similar to what the ScSERF model shows. Overall, the structural data collected for ScSERF agrees well with the structural information published for the homologs MOAG-4 and human SERF1a.

Based on our secondary structure analysis, it is likely that the C-terminal α-helical structure element is not highly populated at physiological temperature. Therefore, the structural models generated here for ScSERF and published for MOAG-4 show a more structured state, than we expect for SERF in the cell, where the structure is more dynamic and disordered. There are several examples in which a disordered protein or disorder region adopt a secondary-structure

element (e.g. α-helix) when bound to a binding partner[19]. Therefore, one hypothesis is that SERF proteins can adopt a α-helical structure when bound to a yet unknown cellular binding partner.

5.2 ScSERF accelerates amyloid kinetics of Aβ40 and α−synuclein

The question addressed here was to determine the underlying mechanism by which the SERF protein accelerates amyloid formation of a diverse range of amyloid proteins[90]. Late-onset of neurodegenerative diseases like Alzheimer's or Parkinson's disease is in most cases, sporadic meaning there is no clear trigger[141]. The late-onset is probably due to the process of nucleation being slow. Based on the microscopic rate constants for nuclei formation determined from the amyloid kinetics of Aβ40/42 in vitro it would take on average $10 - 300$ years for primary nucleation to occur in vivo[142].

Here, the protocol and conditions described by Meisl et al. were successfully used to reproduce the previously published saturation secondary-nucleation mechanism of Aβ40[41,53]. An analysis of the halftimes of Aβ40 amyloid kinetics in the presence of sub-stoichiometric concentration of ScSERF showed that ScSERF does not change the underlying reaction mechanism of Aβ40 amyloid formation in vitro (Fig. 13).

The experimental data with a constant Aβ40 concentration and varying ScSERF concentration was globally fitted while keeping the two combined rate constants for primary nucleation $k_n k_+$ and secondary nucleation $k_2 k_+$ as variable parameters as described previously[41,53,70]. The fit described the data reasonably well, with the highest variance was observed in the transition between lag-phase and growth phase (Fig. 13). Simpler kinetic mechanisms available on amylofit could not describe the data accurately (Appendix Fig. 32). The data fitting revealed that the combined rate constant for primary nucleation, $k_n k_+$, of Aβ40 is accelerated upon the addition of ScSERF at sub-stoichiometric to equimolar concentrations. The combined rate constant for secondary nucleation $k_2 k_+$ was unaffected by ScSERF. The ability to infer mechanism from fitting amyloid kinetics is a novel approach in amyloid research[40,41]. The generation of highly accurate fits for amyloid formation is a difficult task, because of the complexity of the multistep process of amyloid formation and the non-trivial task of experimentally generating high quality data[41].

Two additional approaches were employed to validate the insights gained from the data-fitting analysis. Mathematical modeling can be used to simulate the effect of changing particular rate constants on the sigmoidal amyloid aggregation curve. We can qualitatively compare the

generated kinetic simulations to the reaction curves of Aβ40 aggregation in the presence of varying ScSERF concentrations. We found that the simulation generated when modulating the rate constant for primary nucleation matches our experimental data the best, since we observe a change in the lag-phase, but the slope of the growth phase appears unchanged (Fig. 12).

Another experimental approach to test our hypothesis that ScSERF affects the primary nucleation step is a self-seeded aggregation experiment. In a self-seeded amyloid reaction, the step of primary nucleation is eliminated by the addition of prior generated amyloid seeds. A change in the kinetics would mean that ScSERF effects a second step like elongation or secondary nucleation. I found that ScSERF did not significantly affect kinetics in the self-seeded experiments for Aβ40 (Fig. 16). In conclusion low to equimolar concentration of ScSERF are not changing the underlying mechanism of Aβ40 amyloid formation, but accelerate the specific step of primary nucleation.

I found that sub-stoichiometric ScSERF concentration accelerate the amyloid formation of α-synuclein (Fig. 14). The un-seeded α-synuclein kinetics could not be fitted due to the known experimental limitation in studying α-synuclein aggregation under quiescent conditions at neutral pH[51,52]. Self-seeded amyloid reactions were used to distinguish between primary nucleation and the later steps of elongation and secondary nucleation. ScSERF has only very small effects on the self-seeded aggregation of α-synuclein comparable to the results for Aβ40. Therefore, we concluded that ScSERF mainly affects primary nucleation in the case of α-synuclein as well.

Only a few factors that accelerate amyloid formations have been studied in detail. Two better studied examples are membranes in the form of lipid vesicle and the poly-anion polyphosphate. Lipid vesicles lead to acceleration of amyloid formation of amyloid-β and α-synuclein by providing a surface for heterogenous primary nucleation[143,144]. In the case of polyphosphate it has been shown that polyphosphate accelerates amyloid formation for multiple amyloid proteins (e.g. Aβ40, α-synuclein, tau)[84]. Polyphosphate acts on a aggregation step after primary nucleation has taken place and does not bind to monomeric amyloid proteins[145]. In contrast to these examples, that change the underlying mechanism of amyloid formation, ScSERF action is unique by not changing the underlying mechanism, but rather accelerating the intrinsic rate of primary nucleation. An example in which a protein accelerates amyloid formation is the interaction between α-synuclein and Aβ42. The conformational state of α-synuclein determines the effect it has on Aβ42 amyloid formation. In that case, monomeric α-synuclein

can bind to fibril surfaces and inhibit secondary nucleation of Aβ42. In contrast to its monomeric form, α-synuclein fibrils provide a surface or nuclei to accelerate Aβ42 amyloid formation via a heterogenous nucleation pathway[146]. We did not observe higher oligomeric states of ScSERF and determine its monomeric state as the active state, that accelerates amyloid formation. Our data shows that ScSERF is the first well studied intrinsically disordered protein that accelerates primary nucleation rate for two different amyloid proteins.

While ScSERF affect the same step in the amyloid formation of both Aβ40 and α-synuclein we observed a difference in the ScSERF concentration-dependent effect on the amyloid kinetics. In the case of α-synuclein low ScSERF concentrations are already potent enhancers of amyloid formation, but higher ScSERF concentrations result in even faster amyloid kinetics. In contrast, while sub-stoichiometric concentrations of ScSERF were also very efficient in accelerating Aβ40 amyloid formation, but surprisingly high molar excesses of ScSERF lead to a deceleration of the amyloid formation (Fig. 10). Transmission electron microscopy revealed that Aβ40 formed amorphous aggregates in the samples with high molar ratios of ScSERF (Fig 11). This was not observed in the case of α-synuclein aggregation. Under certain conditions or in the presence of modifiers it has been observed that amyloid proteins can form amorphous aggregates instead of ordered amyloid fibrils. Examples of theses modifiers are metals like zinc ions Zn^{2+}, peptides like IAPP-GI or proteins like Transthyretin (TTR). Equimolar concentration of Zn^{2+} ions lead to the formation of non-amyloid $ZnA\beta40$ oligomers with hydrophobic surfaces that show increased toxicity[126]. IAPP-GI is a peptide that was found to interact with amyloid-β. A complex between IAPP-GI and amyloid-β leads to the formation of insoluble amorphous aggregates, that have been characterized as non-toxic off-pathway aggregates[147]. Transthyretin (TTR), by itself involved in TTR amyloidosis, is another factor that has been shown to alter the Aβ fibril formation pathway. Amyloid aggregation in the presence of Transthyretin (TTR), leads to the formation of ThT-inactive non-fibrillar oligomers[148]. These published examples are cellular factors (e.g. metal ions, proteins etc.) that change the aggregation pathway of amyloid-β into non-fibril aggregates and the off-pathway reaction becomes the dominant reaction. Our data indicates that in the presence of high concentrations of ScSERF both amyloid aggregation and amorphous aggregation are taking place at the same time. We can further hypothesize that the off-pathway reaction can be one explanation for the change in halftime, by decreasing the concentration of free monomeric Aβ40 available for fibril formation. The microscopic steps of amyloid formation are dependent

on the concentration of Aβ40, therefore a lower active concentration will slow down the process of amyloid formation.

An alternative explanation for a decrease in halftime at high ScSERF concentrations might be an unspecific charge effect, ScSERF has a net-charge of +11 at pH 7.4. A study investigating if the net-charge of a protein influences its ability to inhibit amyloid formation found that a small hydrophilic protein that was carrying a net charge between +2 to -4 did not affect Aβ40 aggregation. If the same protein is changed to carry net charges above +6 to +8, it showed the ability to prevent Aβ40 amyloid aggregation in vitro[149]. We can speculate that at high ScSERF concentration a similar nonspecific charge-dependent effect influences the Aβ40 amyloid kinetics and competes with ScSERF accelerating primary nucleation.

Only a few publications have explored the function of SERF proteins in vivo and in vitro[89–91]. The observations made in vivo suggest that the deletion of SERF is beneficial to *C. elegans* or human cells, consistent with the idea that SERF accelerates amyloid formation. The concentration of MOAG-4/SERF protein in vivo varies between organisms and also tissues in humans. In *S. cerevisiae* the concentration of ScSERF was determined be 876 molecules/cell; for comparison the level of the chaperone Hsp70 SSB1 was at 170000 molecules/cell[150]. Therefore, the acceleration of amyloid proteins like α-synuclein and Aβ40 observed with lower concentrations of ScSERF is likely the physiologically relevant mechanism rather than the deceleration of Aβ40 amyloid formation induced by high concentrations of ScSERF.

5.3   Characterization of ScSERF binding to Aβ40 and α-synuclein

Fluorescence anisotropy titrations were employed to determine binding constant K_d for the interaction between ScSERF and both amyloid proteins. The K_d value for α-synuclein was determined to be 9 μM (Fig. 18). A recent study determined the binding constant between SERF1a and α-synuclein to be 2.5 μM[140]. This provides evidence that the highly homologous proteins ScSERF and human SERF1a bind α-synuclein with similar affinities. The K_d for ScSERF binding to Aβ40 was determined to be 32 μM in solution and 10 μM in the gas-phase (Fig. 18, 21). The tighter binding in the gas-phase experiment could be due to a strengthening of ionic interactions in the gas-phase[151].

The acceleration of α-synuclein and Aβ40 amyloid formation in the presence of low ScSERF concentrations might suggest a tighter binding affinity for ScSERF and the monomeric amyloid proteins. In the case of the amyloid kinetics the concentration of both proteins is relevant to

determine the amount of complex present. For example, in the case of 100 μM α-synuclein and 20 μM of ScSERF under equilibrium conditions we would except that 17 % of protein to be in complex with each other. One hypothesis could be that the kinetics of binding and release between ScSERF and the two amyloid proteins is fast. In that case one ScSERF molecule can interact with a number of amyloid protein molecule in a short amount of time and the interaction might be sufficient to lower the energy barrier of nuclei formation. To test this hypothesis further investigation of the kinetics of monomer binding are needed.

SDS-PAGE analysis showed, that the majority of ScSERF protein was in the soluble fraction, while a small amount was found in the pellet. In fluorescence anisotropy experiment we found that ScSERF binds to pre-formed amyloid fibrils of Aβ40 and α-synuclein. Recently Merle et al., showed that aggregated GFP-tagged α-synuclein and SERF1a are co-localized in a human cell-line experiment. From the published study it is not clear if the co-localization is indicative of binding between human SERF1a and α-synuclein aggregates[140]. In contrast to this finding it was previously reported that the *C. elegans* homologue MOAG-4 is only present in the soluble fraction when accelerating the amyloid aggregation of α-synuclein in vitro[91]. The previously shown analysis of amyloid kinetics revealed that ScSERF does not affect the kinetic steps that are involving amyloid fibrils. The fibril binding, we observe could be unspecific due to favorable charge-charge interactions between ScSERF and amyloid proteins in the fibril state. Based on our kinetic finding that ScSERF affects primary nucleation, we focused our structural investigation on the early monomer-dependent steps of amyloid formation.

5.4 Structural investigation of complexes

5.4.1 Determine the ScSERF-binding on ^{15}N-Aβ40

The interaction between ScSERF and monomeric Aβ40 was studied by NMR spectroscopy. We found that the addition of ScSERF to ^{15}N-labeled Aβ40 showed very small chemical shift perturbations. The HSQC spectra for Aβ40 was previously assigned and used to identify the residues affected upon ScSERF addition[152]. The largest chemical shift change was observed in Valine 24 and in the N-terminal region of Aβ40. Additionally, a decrease in the signal intensity across all residues was observed, with the biggest decrease in N-terminal region of Aβ40. This decrease in signal intensity can be interpreted as a shift of the Aβ40 signals towards the intermediate exchange regime, making the interpretation of the interaction data difficult[153].

Previously, a shift towards the intermediate exchange regime for Aβ40 was observed upon the addition of Zn^{2+} [154]. In amyloid-β fibril structures the residue Valine 24 is found in the loop region between two hydrophobic patches formed by the residues ([17]LVFFA[21]) and the C-terminal residues ([34]LMVGGVV[40]) that interact with each other in a β-sheet structure[155,156]. Based on the estimated K_d between Aβ40 and ScSERF complete saturation of the complex was not achieved at the highest ScSERF concentration in the NMR titration (87 % of protein is expected to be in complex). The interaction between ScSERF and Aβ40 has not been previously investigated, but recent publications studied the interaction between MOAG-4/SERF1a and α-synuclein[91,140]. The authors found that SERF1a binds to the negatively charged C-terminal region in α-synuclein. α-synuclein appears to bind to the conserved region in the N-terminal region of SERF1a.

The reverse experiment of titrating Aβ40 into isotopic labeled ScSERF to identify the binding site in ScSERF has the following experimental limitation. The weak binding affinity requires the addition of high concentrations of Aβ40. Aβ40 aggregation is fast at high concentrations making it is difficult to maintain monomeric Aβ40 when concentrating Aβ40 to high concentrations needed for the titration experiment. In conclusion, we could not determine a clear binding site in Aβ40. To study the dynamic interactions during the early steps of amyloid formation we employed native ion mobility mass-spectrometry (IM-MS), which has the advantages of only requiring low protein concentration and enables fast data collection.

5.4.2 Native IM-MS reveals fuzzy complexes between ScSERF and Aβ40/α-synuclein

nESI-IM-MS was employed to investigate the complex between ScSERF and both amyloid proteins. The desolvation of a protein by nano-electrospray ionization (nESI) gives rise to the charge-state distribution of a protein, which provides information on the number of conformational states a protein occupies in solution[157]. Furthermore, IM-MS informs on the structural conformation of a protein or protein complex in the form of the rotationally averaged collision cross sections (CCSs). A comparable parameter to the CCSs in solution is the frictional ratio f/f0 of a protein, that can be determined by sedimentation velocity analytical ultracentrifugation experiments.

Here for the first time we characterized ScSERF by IM-MS. ScSERF shows a broad charge state distribution with 11 different charge states indicating that ScSERF has multiple conformations in solution (Fig. 21). This is characteristic for an intrinsically disordered protein occupying a range of conformations in solution[158]. A globular folded protein (for example

ubiquitin) below 150 kDa tends ionize in fewer than 7 charge states, in comparison to disordered or denatured protein that have more than 7 charge states[134].

By analyzing the arrival time distribution (ATDs) we found that ScSERF has a range of conformations with collision cross sections (CCCs) values ranging from 9 to 22 nm^2. The broad range of CCS shows that ScSERF exists in elongated conformations, which was consistent with the frictional ratio f/f0 of 1.7 determined for ScSERF.

Additionally, to extended monomeric conformations of ScSERF we found multiple charge states corresponding to dimeric ScSERF species. It is possible that at high protein concentrations two proteins can get trapped in the same nESI droplet due to proximity in solution. To avoid this all experiments were performed at low protein concentrations, therefore we can exclude this possibility. Nevertheless, we could not observe ScSERF dimers in solution experiments indicating a transient and/or low populated state. The role of these ScSERF dimers remains unexplored and more experiments are needed. Higher resolutions methods like single-molecule fluorescence resonance energy transfer (smFRET) have the ability to interrogate dimer formation in solution[159].

For Aβ40 we detected only two charge states with a narrow range of CCSs, indicating a more compact conformation, that was confirmed by the friction ratio f/f0 of 1.3 for Aβ40 in solution. Aβ40 dimers are also seen at low intensity in our samples. Aβ40 was previously characterized by IM-MS and our observation of match the published results[134,160].

We found that in an equimolar mixture of Aβ40:ScSERF engage in complexes with three different stoichiometries (1:1, 1:2, 2:1) (Fig. 21). The 1:1 complex is the most abundant complex. We observe multimodal broad arrival time distribution (ATDs) indicating that the complex exists a range of conformations. The large collision cross section detected for the 1:1 complex indicates that ScSERF keeps it extended conformation when binding to Aβ40. Additionally, the multiple states occupied by the 1:1 complex indicates that ScSERF and Aβ40 interact in multiple conformations. A dynamic interaction can be supported by our observation that addition of ScSERF to ^{15}N-Aβ40 leads to a change of the exchange regime. Additionally, to the 1:1 complex, higher stoichiometric complex were observed. These complexes also exist in multiple conformations.

In comparison to the 1:1 complex, the higher stoichiometric complexes (1:2, 2:1) show comparatively more compact collision cross section. The complexes could be the result of a dimeric ScSERF or dimeric Aβ40 binding to a monomeric ScSERF/Aβ40 protein or it could be that two independent monomers bind another monomer. Based on the data we have collected

both scenarios are conceivable. Soluble dimeric and tetrameric Aβ40 complexes have been previously observed by IM-MS[61]. In our case the we only observe monomer and dimers of Aβ40. IM-MS analysis enabled us to visualize the lower abundance higher stoichiometric complexes[161]. To our knowledge ScSERF is the first host factor, that has been shown to interact with Aβ40 monomers in multiple stoichiometries and conformations.

We monitored the reaction between ScSERF and Aβ40 over time and took samples every 30 min to be investigated by IM-MS (Fig. 22). We found that the complexes, that we observed at time point zero were present for the first 4 hours. The distribution of complexes did not change over time. This observation suggests that not one specific complex is responsible for the acceleration of primary nucleation. A limitation in the IM-MS experiment is that only soluble states that can be ionized by nESI are observable. Therefore, we cannot exclude that a small insoluble nuclei or aggregates becomes enriched in the presence of ScSERF and are responsible for the change in amyloid kinetics. Some techniques and conditions allow the isolation of oligomers through a series of SEC steps[105,162]. Unfortunately, detailed structural information is not available. Our experimental conditions are more in line with physiological relevant condition and suggest that the conformational space that Aβ40 monomers explore to form nuclei can be expanded by ScSERF, and that the detected structural and stoichiometric diverse interactions might be sufficient to have a significant impact on the amyloid kinetics.

We found that monomeric α-synuclein has at least 14 different charge states and broad arrival time distributions indicating a range of extended conformations (Fig. 23). This result is consistent with previously published native IM-MS data for α-synuclein[163]. Furthermore, the extended nature of α-synuclein conformations was also observed in SV-AUC experiments, the frictional ration f/f0 was 2.1. Five charged states of a α-synuclein dimeric species were detected and also described in the literature[164]. α-synuclein dimers were not detected in the SV-AUC experiment.

In equimolar concentrations of ScSERF and α-synuclein we observe four different stoichiometries (1:1, 1:2, 2:1, 2:2). The 1:1 complex is the most abundant complex and shows a wide charges state distribution and large collision cross section. It appears that ScSERF and α-synuclein both stay in their elongated and disordered conformation in the complex. The higher stoichiometric complex could again be interpreted in two ways, one as the interaction of a dimeric ScSERF/α-synuclein interacting with a monomer or two independent monomers interacting with another monomer. The higher stoichiometric complexes appear to be

conformationally diverse and structural diverse states. The 2:2 complex shows remarkably large CCSs for the interaction of two small protein and are only observed for the interaction between ScSERF:α-synuclein and not for the interaction of ScSERF and Aβ40[133].

The interaction between two ScSERF homologues SERF1a/MOAG-4 and α-synuclein has previously been investigated using NMR spectroscopy. Yoshimura et al. have put forward a model in which MOAG-4 binding to α-synuclein competes with intramolecular interaction between C-terminal and N-terminal charges in α-synuclein[91]. Our finding that both proteins have extended conformations in the 1:1 complex support this hypothesis. Furthermore, computational modeling constrained by NMR and SAXS data done by Merle et al. between SERF1a and α-synuclein suggested that SERF1a binding to α-synuclein results in a exposed hydrophobic NAC region in α-synuclein[140]. The modelling also describes multiple conformations between SERF1a and α-synuclein in complex. Our IM-MS data expands on the published data, by providing direct evidence for complexes between ScSERF and two different amyloid proteins with multiple extended conformations. The observation of complexes with different stoichiometries is a novel finding, showing the advantages of native IM-MS in detecting low-abundant protein complexes.

The phenomenon in which at least one interaction partner stays in a disordered state can be described by the term fuzziness[24]. The plasticity of intrinsically disordered protein allows binding to scaffold or "hub" proteins in multiple conformations. This mode of interaction has the advantage that association rates can be fast, because conformational orientation is not required for association. This phenomenon was observed for the interaction between Sendai virus nucleoprotein and phosphoprotein. Sendai virus nucleoprotein samples a range of conformational states in solution that initially bind to phosphoprotein, the binding event leads to the formation of a stabilizes helical conformation in complex[165]. Another case of fuzzy complexes is the interaction between two disordered domains. Nuclear transport receptor (NTR) are forming fuzzy complexes with the FG-nucleoporins. NTR's have multiple binding sites for FG-nucleoporins and the association kinetics are very fast. The binding of two disordered proteins has low entropic cost, because a high degree of conformational heterogeneity is maintained[166]. An extreme example of a fuzzy complex is the interaction between two intrinsically disordered proteins between prothymosin-α and histone 1.0 [5]. Both proteins stay disordered and conformationally dynamic in complex that is physiologically active. The complexes we have observed here between ScSERF and Aβ40/α-synuclein can be characterized as fuzzy complex between two intrinsically disordered proteins similar to the

example of prothymosin-α and histone 1.0 [5]. In contrast to the weak micromolar binding affinity measured for ScSERF and Aβ40/α-synuclein the affinity between prothymosin-α and histone 1.0 is in the nanomolar range. We hypothesize that conformational flexibility of ScSERF is one reason it is able to accelerate amyloid formation for both of the unrelated amyloid-prone proteins investigated in this study, Aβ40 and α-synuclein, and the same mechanism could also apply for the additional SERF substrates that have been reported in the literature, namely, Huntingtin exon1 and prion protein PrP[90].

It appears that the structural diversity of interaction is important for acceleration of amyloid formation by ScSERF. Well-characterized example in which disorder is employed to achieve function are molecular chaperons like HdeA, Hsp33 or Hsp26[167]. In the case of Hsp33 or HdeA change in environmental conditions leads to an order-to-disorder transition and the exposed disordered regions can facilitate client interaction. Molecular chaperones have been shown to modify amyloid formation and kinetics. The J-domain chaperone DNAJB6 (Hsp40-family) can inhibit the aggregation of Aβ40/42, α-synuclein and polyQ. DNAJB6 inhibits the step of primary nucleation for Aβ42, by binding to oligomeric species[64,168]. The extracellular chaperone clusterin binds to Aβ40 oligomers and sequesters them, which is thought to reduce the number of toxic oligomers[169]. Molecular chaperones are promiscuous and often interact with hydrophobic regions, that are exposed in mis-folded proteins, therefore it is not suppressing that most chaperones inhibit amyloid formation by binding to aggregated or fibril states of amyloid proteins[170]. In the case of larger disordered amyloid proteins like the tau protein, that relies on chaperoning from Hsp70 and Hsp90 to be functional in the first place, the chaperone network can also engage with monomeric misfolded tau protein[171]. In comparison to host folding factors the mechanism by which ScSERF modifies amyloid formation is different by interaction with disordered monomeric states of amyloid proteins.

The observed range of conformation and complexes in the presence of ScSERF demonstrate the challenges in developing molecules or strategies that address amyloid formation in the early stages. Furthermore, our findings suggest that there might be other small or disorder host factors that can influence amyloid formation and that have not been discovered or characterized.

5.5   ScSERF's affect on amyloid formation in vivo

MOAG-4 was discovered in a genetic screen for modifiers of amyloid formation in *C. elegans*. Amyloid proteins that are overexpressed by a strong promoter lead to protein aggregation that causes cytotoxicity in *S. cerevisiae*[100,172]. We used established systems for two amyloid proteins HTT exon 1 (polyQ) and α-synuclein to test whether ScSERF deletion shows a similar phenotype to MOAG-4 in *C. elegans*[87].

First, we could reproduce the published phenotypes for the amyloid over production experiments (Fig.25, 26), but the deletion of ScSERF did not affect the observed cytotoxicity (Fig. 25, 26)[100,101]. We compared the in vivo protein levels of SERF proteins available from other studies ScSERF is present at 143 ppm in S. cereviase[150], human SERF1a is present at 60 ppm, human SERF2 at 318 ppm and the *C. elegans* homologue MOAG-4 is expressed at 387 ppm[173]. This indicates that ScSERF expression level in yeast is 2-3-fold lower compared to *C. elegans*.

Because of the already low levels of ScSERF in *S. cerevisiae* it is possible that a deletion has a smaller effect and therefore is not sensitive to the cytotoxicity experiment. SERF's sequence is highly conserved across eukaryotic species indicating a conserved function, but it is not essential for growth in *S. cerevisiae*. It is conceivable that under the chosen growth and assay conditions *S. cerevisiae* is not reliant on ScSERF function. An approach to investigates ScSERF function in vivo, that is not reliant on toxicity is to monitor the formation of amyloid aggregates with biosensors that can be monitored via fluorescence microscopy[174]. The recent finding that SERF1a can act as an RNA chaperone in a human cell line experiment can be addressed in *S. cerevisiae*[92]. RNA binding proteins like the RNA-binding protein FUS (FUS) can form amyloid fibrils or phase-separate and are associated with neurodegenerative disease[175,176]. SERF might emerge as a new and interesting link between regulation of certain RNAs and amyloid formation.

5.6   Proposed model of ScSERF interaction with Aβ40 and α -synuclein

In summary, we propose a model in which ScSERF forms extended complexes in multiple stoichiometries with Aβ40 and α-synuclein. The protein complexes between ScSERF and Aβ40/α-synuclein have multiple elongated conformation, that indicates high conformational flexibility in the complex. The increased flexibility in complex between ScSERF and Aβ40/α-synuclein might lead to the exploration of an increased conformational space in the complex.
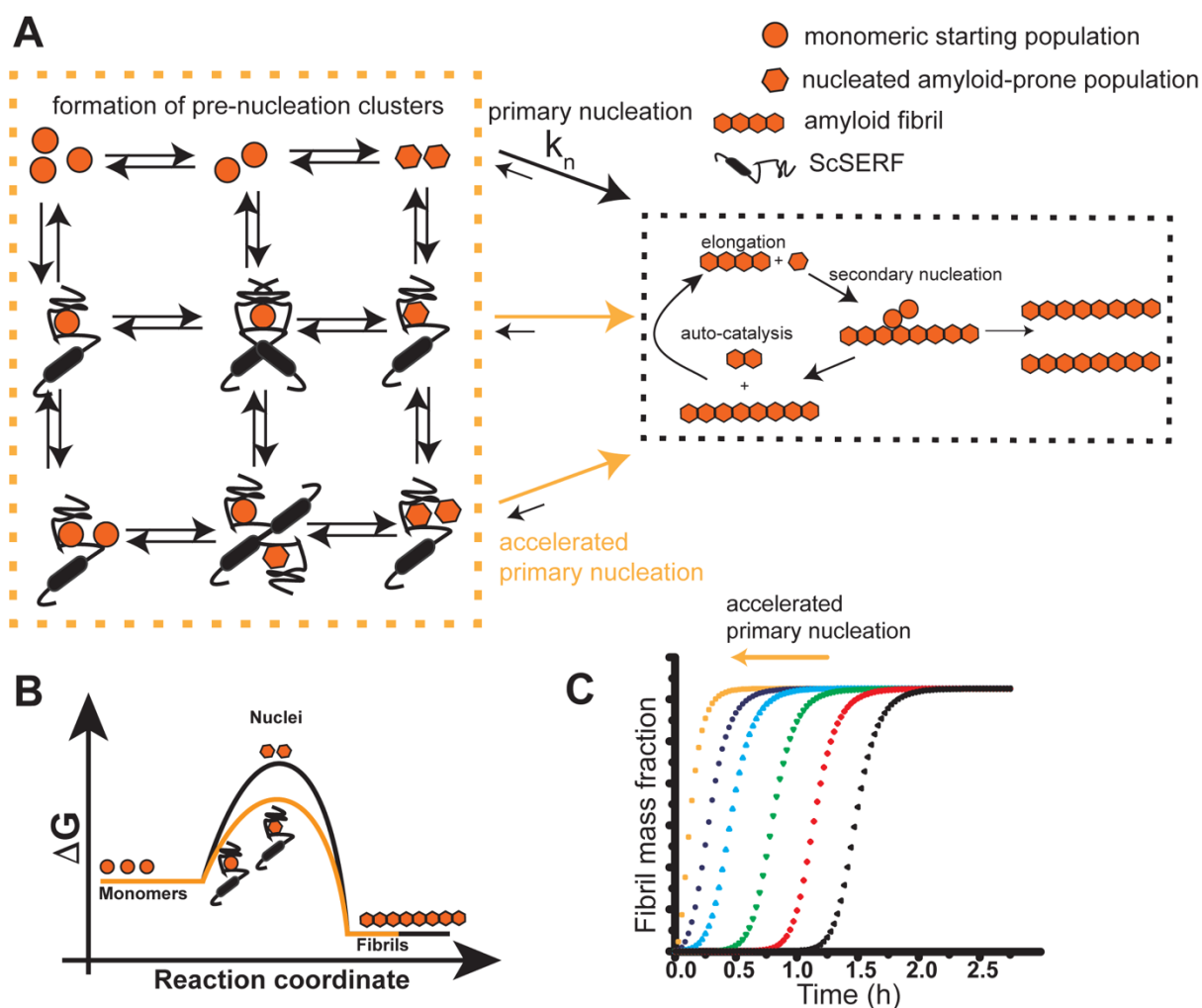
Figure 27: Proposed model of ScSERF's effect on amyloid formation.
(A) The Aβ40/α-synuclein amyloid formation pathway consists of primary nucleation, elongation, and secondary nucleation. During primary nucleation, Aβ40/α-synuclein forms its amyloid-prone conformation (hexagons) from the starting pool of disordered monomeric Aβ40 (circles). ScSERF engages in three different complexes with Aβ40 (1:1, 1:2, 2:1) and in four different complexes with α-synuclein (1:1, 1:2, 2:1, 2:2). In the presence of ScSERF, the primary nucleation step is accelerated by these binding events. (B) Simplified free energy diagram of amyloid formation. Nuclei have the highest free energy state, while fibril are slightly lower free energy than the monomer state. (C) Simulation of amyloid formation, visualizing the change of primary nucleation rate constant (see Fig. 12) (Figure adapted after Meinen *et al.,* 2019).

A mixture of theses complexes is present in the early stage of amyloid formation (Fig. 27 A). We can characterize them as fuzzy complexes, it is the first time that these range of conformational heterogenous complexes have been observed for Aβ40 and α-synuclein. Nuclei have the highest free energy state in the process of amyloid formation[42]. We hypothesize that ScSERF binding lowers the free energy barrier for nuclei formation, which results in an acceleration of primary nucleation (Fig 27 B). For α-synuclein the disruption of intermolecular

interaction is beneficial for amyloid formation[177,178]. ScSERF binding leads to an increase in extended conformation of α-synuclein and disrupts intermolecular interactions. The structure of early Aβ40 conformations is still not well understood, but our data suggest that ScSERF binding and the formation of extended structures is accelerating primary nucleation.

Host factors like ScSERF that accelerate amyloid formation or lead to the formation of toxic intermediates or off-pathway aggregates might provide good targets to reduce the load of amyloid formation in vivo.

5.7 Future directions

This work showed for the first time, that the amyloid proteins Aβ40/α-synuclein can engage in a fuzzy complex with the intrinsically disordered protein ScSERF. One question for future experiments will be to investigate if the conformational flexibility observed for ScSERF is also present in complexes with other native interaction partners in *S. cerevisiae*. The yeast prion protein PrP was shown to interact with SERF1a, PrP might be another target to investigate if the observations made here are applicable for more SERF targets. Furthermore, the cellular function of ScSERF is still unclear, a broad genetic screen in which we cross SERF deletion strains, with a yeast deletion library to create double-gene deletions can reveal synthetic lethal deletion and help identify functions and pathways that SERF is involved in. The recent observation that SERF1a binds to RNA is a new avenue that can be further explored[92].

Merle et al. propose that α-synuclein binds to the N-terminus of SERF1a and the binding site for Aβ40 is still not known[89]. A mutational analysis in the conserved N-terminus of ScSERF can help to identify the binding site and important residues for ScSERF's amyloid aggregation modifying activity. Our data suggest that finding small molecules that can inhibit the interaction between SERF and amyloid proteins could potentially be beneficial in delaying amyloid formation. Small molecule libraries can be screened in vitro in a ThT assay set up. Established in vivo systems of amyloid toxicity in *C. elegans* or *S. cerevisiae* can be utilized to screen small molecules in in vivo experiments.

6 References

1. Hipp, M. S., Kasturi, P. & Hartl, F. U. The proteostasis network and its decline in ageing. *Nat. Rev. Mol. Cell Biol.* **20**, 421–435 (2019).

2. Bartlett, A. I. & Radford, S. E. An expanding arsenal of experimental methods yields an explosion of insights into protein folding mechanisms. *Nat. Struct. Mol. Biol.* **16**, 582–588 (2009).

3. Dobson, C. M., Šali, A. & Karplus, M. Protein Folding: A Perspective from Theory and Experiment. *Angew. Chemie Int. Ed.* **37**, 868–893 (1998).

4. Goloubinoff, P., Sassi, A. S., Fauvet, B., Barducci, A. & De Los Rios, P. Chaperones convert the energy from ATP into the nonequilibrium stabilization of native proteins. *Nat. Chem. Biol.* **14**, 388–395 (2018).

5. Borgia, A. *et al.* Extreme disorder in an ultrahigh-affinity protein complex. *Nature* **555**, 61–66 (2018).

6. Dunker, A. K., Silman, I., Uversky, V. N. & Sussman, J. L. Function and structure of inherently disordered proteins. *Curr. Opin. Struct. Biol.* **18**, 756–764 (2008).

7. White, D. a., Buell, A. K., Knowles, T. P. J., Welland, M. E. & Dobson, C. M. Protein aggregation in crowded environments. *J. Am. Chem. Soc.* **132**, 5170–5175 (2010).

8. Finka, A., Mattoo, R. U. H. & Goloubinoff, P. Experimental Milestones in the Discovery of Molecular Chaperones as Polypeptide Unfolding Enzymes. *Annu. Rev. Biochem.* **85**, 715–742 (2016).

9. Hartl, F. U., Bracher, A. & Hayer-Hartl, M. Molecular chaperones in protein folding and proteostasis. *Nature* **475**, 324–332 (2011).

10. Moreau, K. L. & King, J. A. Protein misfolding and aggregation in cataract disease and prospects for prevention. *Trends Mol. Med.* **18**, 273–282 (2012).

11. Iadanza, M. G., Jackson, M. P., Hewitt, E. W., Ranson, N. A. & Radford, S. E. A new era for understanding amyloid structures and disease. *Nat. Rev. Mol. Cell Biol.* **19**, 755–773 (2018).

12. Chiti, F. & Dobson, C. M. Protein Misfolding, Functional Amyloid, and Human Disease. *Annu. Rev. Biochem.* **75**, 333–366 (2006).

13. Ilie, I. M. & Caflisch, A. Simulation Studies of Amyloidogenic Polypeptides and Their Aggregates. *Chem. Rev.* **119**, 6956–6993 (2019).

14. Powers, E. T., Morimoto, R. I., Dillin, A., Kelly, J. W. & Balch, W. E. Biological and chemical approaches to diseases of proteostasis deficiency. *Annu. Rev. Biochem.* **78**,

959–991 (2009).

15. Cheignon, C. *et al.* Oxidative stress and the amyloid beta peptide in Alzheimer's disease. *Redox Biol.* **14**, 450–464 (2018).

16. López-Otín, C., Blasco, M. A., Partridge, L., Serrano, M. & Kroemer, G. The Hallmarks of Aging. *Cell* **153**, 1194–1217 (2013).

17. Ben-Zvi, A., Miller, E. A. & Morimoto, R. I. Collapse of proteostasis represents an early molecular event in Caenorhabditis elegans aging. *Proc. Natl. Acad. Sci.* **106**, 14914–14919 (2009).

18. Walther, D. M. *et al.* Widespread Proteome Remodeling and Aggregation in Aging C. elegans. *Cell* **168**, 944 (2017).

19. van der Lee, R. *et al.* Classification of Intrinsically Disordered Regions and Proteins. *Chem. Rev.* **114**, 6589–6631 (2014).

20. Uversky, V. N. Protein intrinsic disorder and structure-function continuum. in *Progress in Molecular Biology and Translational Science* 1–17 (Elsevier B.V., 2019). doi:10.1016/bs.pmbts.2019.05.003

21. Dunker, A. K., Brown, C. J., Lawson, J. D., Iakoucheva, L. M. & Obradović, Z. Intrinsic disorder and protein function. *Biochemistry* **41**, 6573–82 (2002).

22. Sugase, K., Dyson, H. J. & Wright, P. E. Mechanism of coupled folding and binding of an intrinsically disordered protein. *Nature* **447**, 1021–1025 (2007).

23. Arbesú, M., Iruela, G., Fuentes, H., Teixeira, J. M. C. & Pons, M. Intramolecular Fuzzy Interactions Involving Intrinsically Disordered Domains. *Front. Mol. Biosci.* **5**, (2018).

24. Tompa, P. & Fuxreiter, M. Fuzzy complexes: polymorphism and structural disorder in protein–protein interactions. *Trends Biochem. Sci.* **33**, 2–8 (2008).

25. Selkoe, D. J. Folding proteins in fatal ways. *Nature* **426**, 900–904 (2003).

26. Soto, C. & Pritzkow, S. Protein misfolding, aggregation, and conformational strains in neurodegenerative diseases. *Nat. Neurosci.* **21**, 1332–1340 (2018).

27. Soto, C. Unfolding the role of protein misfolding in neurodegenerative diseases. *Nat. Rev. Neurosci.* **4**, 49–60 (2003).

28. Selkoe, D. J. & Hardy, J. The amyloid hypothesis of Alzheimer's disease at 25 years. *EMBO Mol. Med.* **8**, 595–608 (2016).

29. Ludewig, S. & Korte, M. Novel Insights into the Physiological Function of the APP (Gene) Family and Its Proteolytic Fragments in Synaptic Plasticity. *Front. Mol. Neurosci.* **9**, (2017).

30. Hardy, J. & Selkoe, D. J. The amyloid hypothesis of Alzheimer's disease: progress and problems on the road to therapeutics. *Science* **297**, 353–6 (2002).

31. Dahlgren, K. N. *et al.* Oligomeric and Fibrillar Species of Amyloid-β Peptides Differentially Affect Neuronal Viability. *J. Biol. Chem.* **277**, 32046–32053 (2002).

32. Xu, M. *et al.* γ-Secretase: characterization and implication for Alzheimer disease therapy. *Neurobiol. Aging* **23**, 1023–1030 (2002).

33. Stefanis, L. α-Synuclein in Parkinson's disease. *Cold Spring Harb. Perspect. Med.* **2**, a009399 (2012).

34. Conway, K. a *et al.* Acceleration of oligomerization, not fibrillization, is a shared property of both alpha-synuclein mutations linked to early-onset Parkinson's disease: implications for pathogenesis and therapy. *Proc. Natl. Acad. Sci. U. S. A.* **97**, 571–576 (2000).

35. Mehra, S., Sahay, S. & Maji, S. K. α-Synuclein misfolding and aggregation: Implications in Parkinson's disease pathogenesis. *Biochim. Biophys. Acta - Proteins Proteomics* **1867**, 890–908 (2019).

36. Theillet, F.-X. *et al.* Structural disorder of monomeric α-synuclein persists in mammalian cells. *Nature* **530**, 45–50 (2016).

37. Glabe, C. G. Common mechanisms of amyloid oligomer pathogenesis in degenerative disease. *Neurobiology of Aging* **27**, 570–575 (2006).

38. Ahmed, M. *et al.* Structural conversion of neurotoxic amyloid-β1–42 oligomers to fibrils. *Nat. Struct. Mol. Biol.* **17**, 561–567 (2010).

39. Biancalana, M. & Koide, S. Molecular mechanism of Thioflavin-T binding to amyloid fibrils. *Biochim. Biophys. Acta - Proteins Proteomics* **1804**, 1405–1412 (2010).

40. Knowles, T. P. J. *et al.* An analytical solution to the kinetics of breakable filament assembly. *Science* **326**, 1533–7 (2009).

41. Meisl, G., Yang, X., Dobson, C. M., Linse, S. & Knowles, T. P. J. Molecular mechanisms of protein aggregation from global fitting of kinetic models. *Nat. Protoc.* **11**, 252–272 (2016).

42. Arosio, P., Knowles, T. P. J. & Linse, S. On the lag phase in amyloid fibril formation. *Phys. Chem. Chem. Phys.* **17**, 7606–7618 (2015).

43. Arosio, P., Cukalevski, R., Frohm, B., Knowles, T. P. J. & Linse, S. Quantification of the Concentration of Aβ42 Propagons during the Lag Phase by an Amyloid Chain Reaction Assay. *J. Am. Chem. Soc.* **136**, 219–225 (2014).

44.	Yamaguchi, T., Matsuzaki, K. & Hoshino, M. Transient formation of intermediate conformational states of amyloid-β peptide revealed by heteronuclear magnetic resonance spectroscopy. *FEBS Lett.* **585**, 1097–1102 (2011).

45.	Cohen, S. I. A. *et al.* Proliferation of amyloid-β 42 aggregates occurs through a secondary nucleation mechanism. *Proc. Natl. Acad. Sci.* **110**, 9758–9763 (2013).

46.	Linse, S. Monomer-dependent secondary nucleation in amyloid formation. *Biophys. Rev.* **9**, 329–338 (2017).

47.	Yang, X. *et al.* On the role of sidechain size and charge in the aggregation of Aβ42 with familial mutations. *Proc. Natl. Acad. Sci. U. S. A.* **115**, E5849–E5858 (2018).

48.	Cohen, S. I. A., Vendruscolo, M., Dobson, C. M. & Knowles, T. P. J. From Macroscopic Measurements to Microscopic Mechanisms of Protein Aggregation. *J. Mol. Biol.* **421**, 160–171 (2012).

49.	Tyedmers, J., Mogk, A. & Bukau, B. Cellular strategies for controlling protein aggregation. *Nat. Rev. Mol. Cell Biol.* **11**, 777–788 (2010).

50.	Xue, W.-F. *et al.* Fibril Fragmentation Enhances Amyloid Cytotoxicity. *J. Biol. Chem.* **284**, 34272–34282 (2009).

51.	Buell, A. K. *et al.* Solution conditions determine the relative importance of nucleation and growth processes in a-synuclein aggregation. *Proc. Natl. Acad. Sci.* **111**, 7671–7676 (2014).

52.	Gaspar, R. *et al.* Secondary nucleation of monomers on fibril surface dominates α-synuclein aggregation and provides autocatalytic amyloid amplification. *Q. Rev. Biophys.* **50**, 1–12 (2018).

53.	Meisl, G. *et al.* Differences in nucleation behavior underlie the contrasting aggregation kinetics of the Aβ40 and Aβ42 peptides. *Proc. Natl. Acad. Sci.* **111**, 9384–9389 (2014).

54.	Zhong, Y., Hyung, S.-J. & Ruotolo, B. T. Ion mobility–mass spectrometry for structural proteomics. *Expert Rev. Proteomics* **9**, 47–58 (2012).

55.	Susa, A. C., Xia, Z. & Williams, E. R. Small Emitter Tips for Native Mass Spectrometry of Proteins and Protein Complexes from Nonvolatile Buffers That Mimic the Intracellular Environment. *Anal. Chem.* **89**, 3116–3122 (2017).

56.	May, J. C. & McLean, J. A. Ion Mobility-Mass Spectrometry: Time-Dispersive Instrumentation. *Anal. Chem.* **87**, 1422–1436 (2015).

57.	Chen, S.-H. & Russell, D. H. How Closely Related Are Conformations of Protein Ions Sampled by IM-MS to Native Solution Structures? *J. Am. Soc. Mass Spectrom.* **26**,

1433–1443 (2015).

58. Bush, M. F. *et al.* Collision cross sections of proteins and their complexes: A calibration framework and database for gas-phase structural biology. *Proc. Natl. Acad. Sci. U.S.A* **39**, 31 (2010).

59. Ruotolo, B. T. & Robinson, C. V. Aspects of native proteins are retained in vacuum. *Curr. Opin. Chem. Biol.* **10**, 402–408 (2006).

60. Soper, M. T., DeToma, A. S., Hyung, S.-J., Lim, M. H. & Ruotolo, B. T. Amyloid-β– neuropeptide interactions assessed by ion mobility-mass spectrometry. *Phys. Chem. Chem. Phys.* **15**, 8952 (2013).

61. Bernstein, S. L. *et al.* Amyloid-β protein oligomerization and the importance of tetramers and dodecamers in the aetiology of Alzheimer's disease. *Nat. Chem.* **1**, 326– 331 (2009).

62. Heuvel, R. H. van den & Heck, A. J. Native protein mass spectrometry: from intact oligomers to functional machineries. *Curr. Opin. Chem. Biol.* **8**, 519–526 (2004).

63. Benesch, J. L. & Ruotolo, B. T. Mass spectrometry: come of age for structural and dynamical biology. *Curr. Opin. Struct. Biol.* **21**, 641–649 (2011).

64. Arosio, P. *et al.* Kinetic analysis reveals the diversity of microscopic mechanisms through which molecular chaperones suppress amyloid formation. *Nat. Commun.* **7**, 10948 (2016).

65. Evans, C. G., Wisén, S. & Gestwicki, J. E. Heat shock proteins 70 and 90 inhibit early stages of amyloid β-(1–42) aggregation in vitro. *J. Biol. Chem.* **281**, 33182–33191 (2006).

66. Schirmer, C. *et al.* Hsp90 directly interacts, in vitro, with amyloid structures and modulates their assembly and disassembly. *Biochim. Biophys. Acta - Gen. Subj.* **1860**, 2598–2609 (2016).

67. Lackie, R. E. *et al.* The Hsp70/Hsp90 Chaperone Machinery in Neurodegenerative Diseases. *Front. Neurosci.* **11**, 254 (2017).

68. Ballet, T. *et al.* DnaK prevents human insulin amyloid fiber formation on hydrophobic surfaces. *Biochemistry* **51**, 2172–2180 (2012).

69. Cohen, S. I. A. *et al.* A molecular chaperone breaks the catalytic cycle that generates toxic Aβ oligomers. *Nat. Struct. Mol. Biol.* **22**, 207–213 (2015).

70. Chen, G. *et al.* Bri2 BRICHOS client specificity and chaperone activity are governed by assembly state. *Nat. Commun.* **8**, 2081 (2017).

71.   DeSantis, M. E. *et al.* Operational Plasticity Enables Hsp104 to Disaggregate Diverse Amyloid and Nonamyloid Clients. *Cell* **151**, 778–793 (2012).

72.   Yokom, A. L. *et al.* Spiral architecture of the Hsp104 disaggregase reveals the basis for polypeptide translocation. *Nat. Struct. Mol. Biol.* **23**, 830–837 (2016).

73.   Torrente, M. P. & Shorter, J. The metazoan protein disaggregase and amyloid depolymerase system. *Prion* **7**, 457–463 (2013).

74.   Gao, X. *et al.* Human Hsp70 Disaggregase Reverses Parkinson's-Linked α-Synuclein Amyloid Fibrils. *Mol. Cell* **59**, 781–793 (2015).

75.   Yu, Y. J. & Watts, R. J. Developing Therapeutic Antibodies for Neurodegenerative Disease. *Neurotherapeutics* **10**, 459–472 (2013).

76.   Aprile, F. A. *et al.* Selective targeting of primary and secondary nucleation pathways in Aβ42 aggregation using a rational antibody scanning method. *Sci. Adv.* **3**, e1700488 (2017).

77.   Agerschou, E. D. *et al.* An engineered monomer binding-protein for α-synuclein efficiently inhibits the proliferation of amyloid fibrils. *Elife* **8**, (2019).

78.   Roher, A. E. *et al.* Bapineuzumab Alters Aβ Composition: Implications for the Amyloid Cascade Hypothesis and Anti-Amyloid Immunotherapy. *PLoS One* **8**, e59735 (2013).

79.   Sevigny, J. *et al.* The antibody aducanumab reduces Aβ plaques in Alzheimer's disease. *Nature* **537**, 50–56 (2016).

80.   Haass, C. & Selkoe, D. J. Soluble protein oligomers in neurodegeneration: lessons from the Alzheimer's amyloid β-peptide. *Nat. Rev. Mol. Cell Biol.* **8**, 101–112 (2007).

81.   Zhao, L. N., Long, H. W., Mu, Y. & Chew, L. Y. The Toxicity of Amyloid ß Oligomers. *Int. J. Mol. Sci.* **13**, 7303–7327 (2012).

82.   Lempart, J. & Jakob, U. Role of Polyphosphate in Amyloidogenic Processes. *Cold Spring Harb. Perspect. Biol.* **11**, a034041 (2019).

83.   Yoo, N. G. *et al.* Polyphosphate Stabilizes Protein Unfolding Intermediates as Soluble Amyloid-like Oligomers. *J. Mol. Biol.* **430**, 4195–4208 (2018).

84.   Cremers, C. M. *et al.* Polyphosphate: A conserved modifier of amyloidogenic processes. *Mol. Cell* **63**, 768–780 (2016).

85.   Cohlberg, J. A., Li, J., Uversky, V. N. & Fink, A. L. Heparin and other glycosaminoglycans stimulate the formation of amyloid fibrils from α-synuclein in vitro. *Biochemistry* **41**, 1502–1511 (2002).

86.   Brandvold, K. R. & Morimoto, R. I. The Chemical Biology of Molecular Chaperones -

Implications for Modulation of Proteostasis. *Journal of Molecular Biology* **427**, 2931–2947 (2015).

87.   van Ham, T. J. *et al.* Identification of MOAG-4/SERF as a regulator of age-related proteotoxicity. *Cell* **142**, 601–612 (2010).

88.   Hsu, A.-L., Murphy, C. T. & Kenyon, C. Regulation of Aging and Age-Related Disease by DAF-16 and Heat-Shock Factor. *Science (80-.).* **300**, 1142–1145 (2003).

89.   Merle, D. A. *et al.* Increased aggregation tendency of apha-synuclein in a fully disordered protein complex. *J. Mol. Biol.* **431**, 2581–2598 (2019).

90.   Falsone, S. F. *et al.* SERF protein is a direct modifier of amyloid fiber assembly. *Cell Rep.* **2**, 358–371 (2012).

91.   Yoshimura, Y. *et al.* MOAG-4 promotes the aggregation of α-synuclein by competing with self-protective electrostatic interactions. *J. Biol. Chem.* **292**, 8269–8278 (2017).

92.   Meyer, N. H. *et al.* Structural Fuzziness of the RNA-Organizing Protein SERF Determines a Toxic Gain-of-interaction. *J. Mol. Biol.* (2019). doi:10.1016/j.jmb.2019.11.014

93.   Chen, Y. *et al.* Crystal structure of human histone lysine-specific demethylase 1 (LSD1). *Proc. Natl. Acad. Sci.* **103**, 13956–13961 (2006).

94.   Blattner, F. R. *et al.* The complete genome sequence of Escherichia coli K-12. *Science* **277**, 1453–62 (1997).

95.   Haynes, S. E. *et al.* Variable-velocity traveling-wave ion mobility separation enhancing peak capacity for data-independent acquisition proteomics. *Anal. Chem.* **89**, 5669–5672 (2017).

96.   Polasky, D. A., Dixit, S. M., Fantin, S. M. & Ruotolo, B. T. CIUSuite 2: Next-Generation Software for the Analysis of Gas-Phase Protein Unfolding Data. *Anal. Chem.* **91**, 3147–3155 (2019).

97.   Meinen, B. A., Gadkari, V. V., Stull, F., Ruotolo, B. T. & Bardwell, J. C. A. SERF engages in a fuzzy complex that accelerates primary nucleation of amyloid proteins. *Proc. Natl. Acad. Sci.* **116**, 23040–23049 (2019).

98.   Nakata, Y., Tang, X. & Yokoyama, K. K. Preparation of competent cells for high-efficiency plasmid transformation of Escherichia coli. *Methods Mol. Biol.* **69**, 129–37 (1997).

99.   Burke, D. J., Dawson, D. & Stearns, T. Methods in Yeast Genetics: A Cold Spring Harbor Laboratory Course Manual. *A Cold Spring Harb. Lab. Course Man.* (2015).

100. Petroi, D. *et al.* Aggregate Clearance of α-Synuclein in Saccharomyces cerevisiae Depends More on Autophagosome and Vacuole Function Than on the Proteasome. *J. Biol. Chem.* **287**, 27567–27579 (2012).

101. Krobitsch, S. *et al.* Aggregation of huntingtin in yeast varies with the length of the polyglutamine expansion and the expression of chaperone proteins. *Proc. Natl. Acad. Sci.* **97**, 1589–1594 (2000).

102. Fairbanks, G., Steck, T. L. & Wallach, D. F. H. Electrophoretic analysis of the major polypeptides of the human erythrocyte membrane. *Biochemistry* **10**, 2606–2617 (1971).

103. Gill, S. C. & von Hippel, P. H. Calculation of protein extinction coefficients from amino acid sequence data. *Anal. Biochem.* **182**, 319–26 (1989).

104. Walsh, D. M. *et al.* A facile method for expression and purification of the Alzheimer's disease-associated amyloid β-peptide. *FEBS J.* **276**, 1266–1281 (2009).

105. Jan, A., Hartley, D. M. & Lashuel, H. A. Preparation and characterization of toxic Aβ aggregates for structural and functional studies in Alzheimer's disease research. *Nat. Protoc.* **5**, 1186–1209 (2010).

106. Jain, N., Bhasne, K., Hemaswasthi, M. & Mukhopadhyay, S. Structural and Dynamical Insights into the Membrane-Bound α-Synuclein. *PLoS One* **8**, e83752 (2013).

107. Kelly, S. M., Jess, T. J. & Price, N. C. How to study proteins by circular dichroism. *Biochim. Biophys. Acta - Proteins Proteomics* **1751**, 119–139 (2005).

108. Ohi, M., Li, Y., Cheng, Y. & Walz, T. Negative staining and image classification — powerful tools in modern electron microscopy. *Biol. Proced. Online* **6**, 23–34 (2004).

109. Demeler, B. & Gorbet, G. E. Analytical ultracentrifugation data analysis with ultrascan-III. in *Analytical Ultracentrifugation: Instrumentation, Software, and Applications* 119–143 (2016). doi:10.1007/978-4-431-55985-6_8

110. Demeler, B., Brookes, E. & Nagel-Steger, L. Analysis of heterogeneity in molecular weight and shape by analytical ultracentrifugation using parallel distributed computing. *Methods Enzym.* **454**, 87–113 (2009).

111. Brookes, E., Cao, W. & Demeler, B. A two-dimensional spectrum analysis for sedimentation velocity experiments of mixtures with heterogeneity in molecular weight and shape. in *European Biophysics Journal* **39**, 405–414 (2010).

112. Brookes, E. & Demeler, B. Genetic Algorithm Optimization for Obtaining Accurate Molecular Weight Distributions from Sedimentation Velocity Experiments. in *Analytical Ultracentrifugation VIII* 33–40 (Springer-Verlag, 2006).

doi:10.1007/2882_004

113. Shen, Y., Delaglio, F., Cornilescu, G. & Bax, A. TALOS+: a hybrid method for predicting protein backbone torsion angles from NMR chemical shifts. *J. Biomol. NMR* **44**, 213–223 (2009).

114. Grzesiek, S., Stahl, S. J., Wingfield, P. T. & Bax, A. The CD4 determinant for downregulation by HIV-1 Nef directly binds to Nef. Mapping of the Nef binding surface by NMR. *Biochemistry* **35**, 10256–10261 (1996).

115. Keith Richardson, David Langridge, Sugyan M. Dixit, Kevin Giles, B. T. R. An improved calibration approach for travelling wave ion mobility spectrometry: robust, high-precision collision cross sections. in *Proceedings of the American Society of Mass Spectrometry Annual Conference* THP319 (2019).

116. Bush, M. F. *et al.* Collision Cross Sections of Proteins and Their Complexes: A Calibration Framework and Database for Gas-Phase Structural Biology. *Anal. Chem.* **82**, 9557–9565 (2010).

117. Ishii, K., Noda, M. & Uchiyama, S. Mass spectrometric analysis of protein–ligand interactions. *Biophys. Physicobiology* **13**, 87–95 (2016).

118. Micsonai, A. *et al.* BeStSel: a web server for accurate protein secondary structure prediction and fold recognition from the circular dichroism spectra. *Nucleic Acids Res.* **46**, W315–W322 (2018).

119. Shen, Y. & Bax, A. Protein backbone and sidechain torsion angles predicted from NMR chemical shifts using artificial neural networks. *J. Biomol. NMR* **56**, 227–241 (2013).

120. Shen, Y. *et al.* Consistent blind protein structure generation from NMR chemical shift data. *Proc. Natl. Acad. Sci.* **105**, 4685–4690 (2008).

121. Lange, O. F. *et al.* Determination of solution structures of proteins up to 40 kDa using CS-Rosetta with sparse NMR data from deuterated samples. *Proc. Natl. Acad. Sci.* **109**, 10873–10878 (2012).

122. Shen, Y. *et al.* De novo structure generation using chemical shifts for proteins with high-sequence identity but different folds. *Protein Sci.* **19**, 349–356 (2010).

123. Brown, C. J., Johnson, A. K., Dunker, A. K. & Daughdrill, G. W. Evolution and disorder. *Current Opinion in Structural Biology* **21**, 441–446 (2011).

124. Biancalana, M. & Koide, S. Molecular mechanism of Thioflavin-T binding to amyloid fibrils. *Biochimica et Biophysica Acta - Proteins and Proteomics* **1804**, 1405–1412 (2010).

125. Xue, C., Lin, T. Y., Chang, D. & Guo, Z. Thioflavin T as an amyloid dye: Fibril quantification, optimal concentration and effect on aggregation. *R. Soc. Open Sci.* **4**, (2017).

126. Lee, M.-C. *et al.* Zinc ion rapidly induces toxic, off-pathway amyloid-β oligomers distinct from amyloid-β derived diffusible ligands in Alzheimer's disease. *Sci. Rep.* **8**, 4772 (2018).

127. Thompson, M. Thermodynamic and Kinetic Analysis of Bromodomain–Histone Interactions. in *Biothermodynamics Part B* **466**, 383–407 (2009).

128. Salvay, A. G., Communie, G. & Ebel, C. Sedimentation Velocity Analytical Ultracentrifugation for Intrinsically Disordered Proteins. in *Intrinsically Disordered Protein Analysis* **896**, 91–105 (Springer New York, 2012).

129. Smith, C. A. Estimation of sedimentation coefficients and frictional ratios of globular proteins. *Biochem. Educ.* **16**, 104–106 (1988).

130. Vivekanandan, S., Brender, J. R., Lee, S. Y. & Ramamoorthy, A. A partially folded structure of amyloid-beta(1-40) in an aqueous environment. *Biochem. Biophys. Res. Commun.* **411**, 312–316 (2011).

131. Fawzi, N. L., Ying, J., Ghirlando, R., Torchia, D. A. & Clore, G. M. Atomic-resolution dynamics on the surface of amyloid-β protofibrils probed by solution NMR. *Nature* **480**, 268–272 (2011).

132. Biancalana, M. & Koide, S. Molecular mechanism of Thioflavin-T binding to amyloid fibrils. *Biochim. Biophys. Acta - Proteins Proteomics* **1804**, 1405–1412 (2010).

133. Ruotolo, B. T., Benesch, J. L. P., Sandercock, A. M., Hyung, S.-J. & Robinson, C. V. Ion mobility–mass spectrometry analysis of large protein complexes. *Nat. Protoc.* **3**, 1139–1152 (2008).

134. Beveridge, R. *et al.* A mass-spectrometry-based framework to define the extent of disorder in proteins. *Anal. Chem.* **86**, 10979–10991 (2014).

135. Smith, D. P., Radford, S. E. & Ashcroft, A. E. Elongated oligomers in β 2-microglobulin amyloid assembly revealed by ion mobility spectrometry-mass spectrometry. *Proc. Natl. Acad. Sci.* **107**, 6794–6798 (2010).

136. Ross, E. D., Baxa, U. & Wickner, R. B. Scrambled Prion Domains Form Prions and Amyloid. *Mol. Cell. Biol.* **24**, 7206–7213 (2004).

137. Ross, E. D., Edskes, H. K., Terry, M. J. & Wickner, R. B. Primary sequence independence for prion formation. *Proc. Natl. Acad. Sci.* **102**, 12825–12830 (2005).

138. Khurana, V. & Lindquist, S. Modelling neurodegeneration in Saccharomyces cerevisiae: why cook with baker's yeast? *Nat. Rev. Neurosci.* **11**, 436–449 (2010).

139. Outeiro, T. F. & Lindquist, S. Yeast Cells Provide Insight into Alpha-Synuclein Biology and Pathobiology. *Science (80-.).* **302**, 1772–1775 (2003).

140. Merle, D. A. *et al.* Increased aggregation tendency of alpha-synuclein in a fully disordered protein complex. *J. Mol. Biol.* **431**, 2581–2598 (2019).

141. Bertram, L. The genetic epidemiology of neurodegenerative disease. *J. Clin. Invest.* **115**, 1449–1457 (2005).

142. Banerjee, S. & Mukherjee, S. Cholesterol: A Key in the Pathogenesis of Alzheimer's Disease. *ChemMedChem* **13**, 1742–1743 (2018).

143. Habchi, J. *et al.* Cholesterol catalyses $A\beta42$ aggregation through a heterogeneous nucleation pathway in the presence of lipid membranes. *Nat. Chem.* **10**, 673–683 (2018).

144. Galvagnion, C. *et al.* Lipid vesicles trigger α-synuclein aggregation by stimulating primary nucleation. *Nat. Chem. Biol.* **11**, 229–234 (2015).

145. Lempart, J. *et al.* Mechanistic insights into the protective roles of polyphosphate against amyloid cytotoxicity. *Life Sci. Alliance* **2**, e201900486 (2019).

146. Chia, S. *et al.* Monomeric and fibrillar α-synuclein exert opposite effects on the catalytic cycle that promotes the proliferation of $A\beta42$ aggregates. *Proc. Natl. Acad. Sci. U. S. A.* **114**, 8005–8010 (2017).

147. Rezaei-Ghaleh, N., Andreetto, E., Yan, L. M., Kapurniotu, A. & Zweckstetter, M. Interaction between amyloid beta peptide and an aggregation blocker peptide mimicking islet amyloid polypeptide. *PLoS One* **6**, (2011).

148. Nilsson, L. *et al.* Transthyretin Interferes with Aβ Amyloid Formation by Redirecting Oligomeric Nuclei into Non-Amyloid Aggregates. *J. Mol. Biol.* **430**, 2722–2733 (2018).

149. Assarsson, A., Hellstrand, E., Cabaleiro-Lago, C. & Linse, S. Charge Dependent Retardation of Amyloid β Aggregation by Hydrophilic Proteins. *ACS Chem. Neurosci.* **5**, 266–274 (2014).

150. Ghaemmaghami, S. *et al.* Global analysis of protein expression in yeast. *Nature* **425**, 737–741 (2003).

151. Breuker, K. & McLafferty, F. W. Stepwise evolution of protein native structure with electrospray into the gas phase, 10-12 to 102 s. *Proceedings of the National Academy of Sciences of the United States of America* **105**, 18145–18152 (2008).

152. Yan, Y., McCallum, S. A. & Wang, C. M35 oxidation induces Aβ40-like structural and

dynamical changes in Aβ42. *J. Am. Chem. Soc.* **130**, 5394–5395 (2008).

153. J. Cavanagh, W. Fairbrother, A. Palmer III, N. Skelton, M. R. *Protein NMR Spectroscopy: Principles and Practice, 2nd*. *Protein NMR Spectroscopy: Principles and Practice,* (2007).

154. Rezaei-Ghaleh, N., Giller, K., Becker, S. & Zweckstetter, M. Effect of Zinc Binding on β-Amyloid Structure and Dynamics: Implications for Aβ Aggregation. *Biophys. J.* **101**, 1202–1211 (2011).

155. Paravastu, A. K., Leapman, R. D., Yau, W.-M. & Tycko, R. Molecular structural basis for polymorphism in Alzheimer's beta-amyloid fibrils. *Proc. Natl. Acad. Sci. U. S. A.* **105**, 18349–54 (2008).

156. Lührs, T. *et al.* 3D structure of Alzheimer's amyloid-β(1-42) fibrils. *Proc. Natl. Acad. Sci. U. S. A.* **102**, 17342–17347 (2005).

157. May, J. C. *et al.* Conformational Ordering of Biomolecules in the Gas Phase: Nitrogen Collision Cross Sections Measured on a Prototype High Resolution Drift Tube Ion Mobility-Mass Spectrometer. *Anal. Chem.* **86**, 2107–2116 (2014).

158. Kaltashov, I. A. & Mohimen, A. Estimates of protein surface areas in solution by electrospray ionization mass spectrometry. *Anal. Chem.* **77**, 5370–9 (2005).

159. Roy, R., Hohng, S. & Ha, T. A practical guide to single-molecule FRET. *Nat. Methods* **5**, 507–16 (2008).

160. Bernstein, S. L. *et al.* Amyloid β-protein: Monomer structure and early aggregation states of Aβ42 and its Pro19 alloform. *J. Am. Chem. Soc.* **127**, 2075–2084 (2005).

161. Hoffmann, W., von Helden, G. & Pagel, K. Ion mobility-mass spectrometry and orthogonal gas-phase techniques to study amyloid formation and inhibition. *Curr. Opin. Struct. Biol.* **46**, 7–15 (2017).

162. Pujol-Pina, R. *et al.* SDS-PAGE analysis of Aβ oligomers is disserving research into Alzheimer´s disease: appealing for ESI-IM-MS. *Sci. RepoRts |* **5**, 14809 (2015).

163. Liu, Y., Jovcevski, B. & Pukala, T. L. C-Phycocyanin from Spirulina Inhibits α-Synuclein and Amyloid-β Fibril Formation but Not Amorphous Aggregation. *J. Nat. Prod.* **82**, 66–73 (2019).

164. Bernstein, S. L. *et al.* α-Synuclein: Stable compact and extended monomeric structures and pH dependence of dimer formation. *J. Am. Soc. Mass Spectrom.* **15**, 1435–1443 (2004).

165. Schneider, R. *et al.* Visualizing the molecular recognition trajectory of an intrinsically

disordered protein using multinuclear relaxation dispersion NMR. *J. Am. Chem. Soc.* **137**, 1220–1229 (2015).

166. Milles, S. *et al.* Plasticity of an Ultrafast Interaction between Nucleoporins and Nuclear Transport Receptors. *Cell* **163**, 734–745 (2015).

167. Bardwell, J. C. A. & Jakob, U. Conditional disorder in chaperone action. *Trends Biochem. Sci.* **37**, 517–525 (2012).

168. Månsson, C. *et al.* DNAJB6 is a peptide-binding chaperone which can suppress amyloid fibrillation of polyglutamine peptides at substoichiometric molar ratios. *Cell Stress Chaperones* **19**, 227–239 (2014).

169. Narayan, P. *et al.* The extracellular chaperone clusterin sequesters oligomeric forms of the amyloid-β1−40 peptide. *Nat. Struct. Mol. Biol.* **19**, 79–83 (2012).

170. Muchowski, P. J. & Wacker, J. L. Modulation of neurodegeneration by molecular chaperones. *Nat. Rev. Neurosci.* **6**, 11–22 (2005).

171. Karagöz, G. E. *et al.* Hsp90-Tau Complex Reveals Molecular Basis for Specificity in Chaperone Action. *Cell* **156**, 963–974 (2014).

172. Khurana, V. & Lindquist, S. Modelling neurodegeneration in Saccharomyces cerevisiae: Why cook with baker's yeast? *Nature Reviews Neuroscience* **11**, 436–449 (2010).

173. Wang, M., Herrmann, C. J., Simonovic, M., Szklarczyk, D. & von Mering, C. Version 4.0 of PaxDb: Protein abundance data, integrated across model organisms, tissues, and cell-lines. *Proteomics* **15**, 3163–3168 (2015).

174. Lázaro, D. F. *et al.* Systematic Comparison of the Effects of Alpha-synuclein Mutations on Its Oligomerization and Aggregation. *PLoS Genet.* **10**, e1004741 (2014).

175. Birsa, N., Bentham, M. P. & Fratta, P. Cytoplasmic functions of TDP-43 and FUS and their role in ALS. *Semin. Cell Dev. Biol.* (2019). doi:10.1016/j.semcdb.2019.05.023

176. Luo, F. *et al.* Atomic structures of FUS LC domain segments reveal bases for reversible amyloid fibril formation. *Nat. Struct. Mol. Biol.* **25**, 341–346 (2018).

177. Bertoncini, C. W. *et al.* From The Cover: Release of long-range tertiary interactions potentiates aggregation of natively unstructured α-synuclein. *Proc. Natl. Acad. Sci.* **102**, 1430–1435 (2005).

178. Ahmad, B., Chen, Y. & Lapidus, L. J. Aggregation of α-synuclein is kinetically controlled by intramolecular diffusion. *Proc. Natl. Acad. Sci.* **109**, 2336–2341 (2012).

7 Appendix

7.1 Purification details SDS-PAGE, Chromatograms
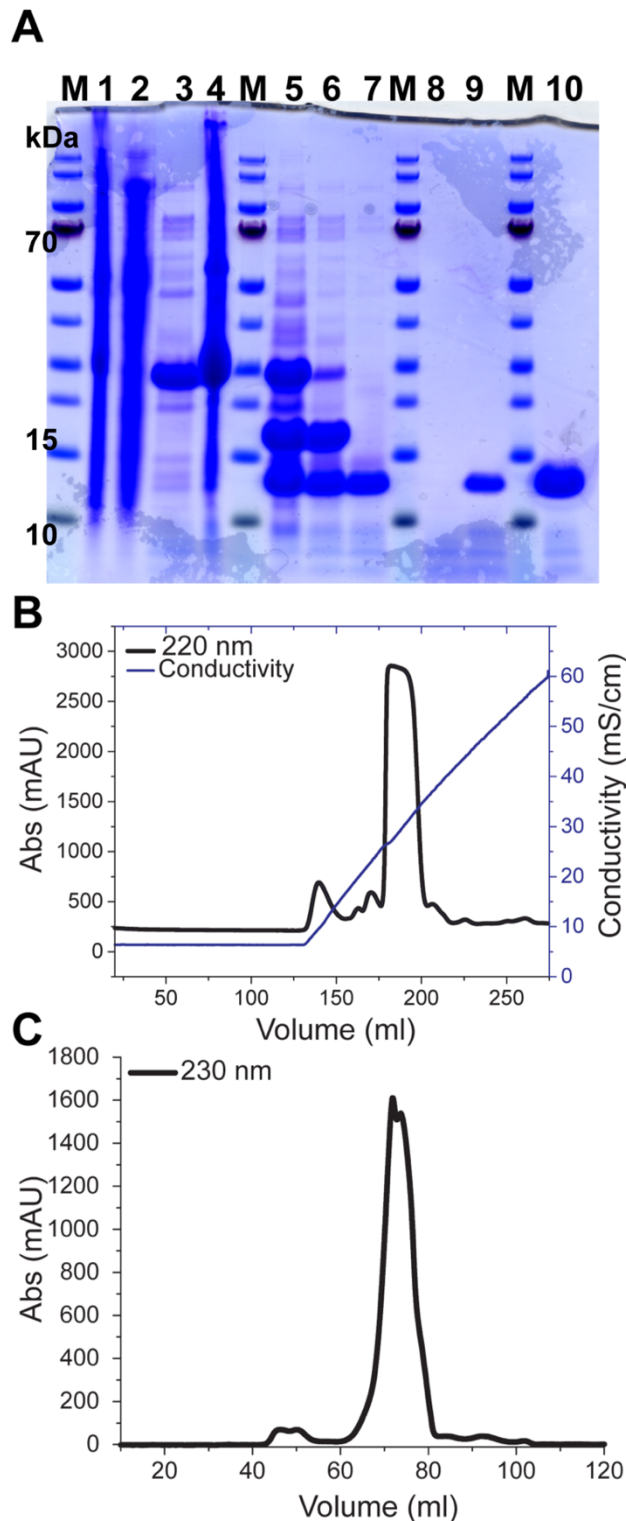
Figure 28: Overview of ScSERF purification. (A) SDS-PAGE of ScSERF purification steps. (M) Molecular weight marker, (1) Cell lysate, (2) NiNTA flow-through, (3) NiNTA wash, (4) NiNTA elution, (5) ULP1 digestion (early), (6) ULP1 digestion overnight, (7) second NiNTA flow-through, (8) Ion exchange flow-through, (9) Ion exchange elution, (10) SEC elution,

(B) Chromatogram Ion exchange. A 5 ml HiTrap SP column was equilibrated with running buffer (50 mM NaH_2PO_4, 125 mM NaCl, pH 6), after loading the column, it is washed and protein eluted in a linear gradient with running buffer containing 1M NaCl. The increasing gradient is shown in the increase in conductivity (blue line). Protein was detected via absorbance at 220 nm (black line). (C) Chromatogram of size-exclusion column. Protein was loaded onto HiLoad 16/60 Superdex S75 equilibrated with SEC buffer (40 mM HEPES, 300 mM NaCl, pH 7.5). Protein was detected via absorbance at 230 nm.
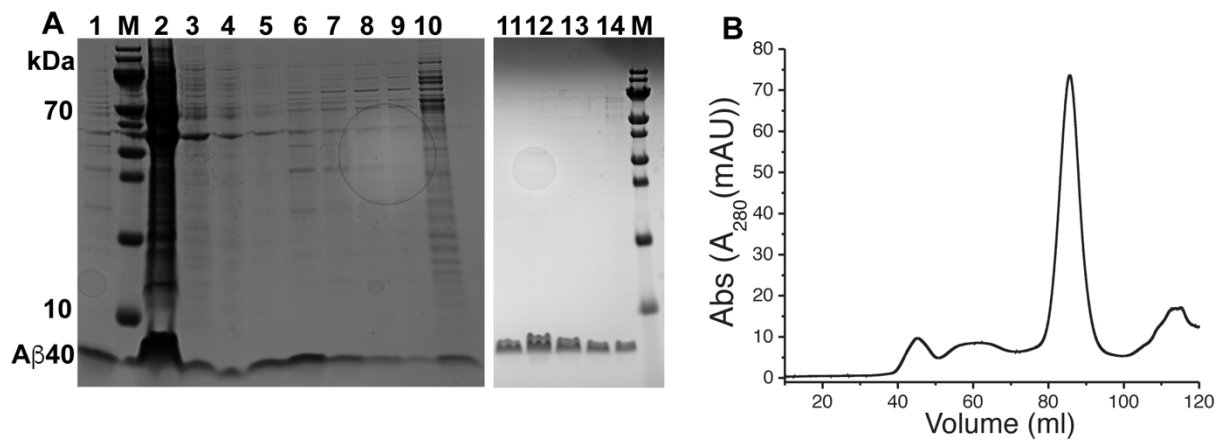
Figure 29: Overview of Aβ40 purification
(A) SDS-PAGE of Aβ40 purification. (M) Molecular weight marker (1) Reference sample Aβ40 (2) Cell lysate (3) Resin Flow-through (4) DEAE resin wash 1 (5) DEAE resin wash 2 (6-9) Elution fractions from DEAE resin (125 mM NaCl) (10) Elution fractions from DEAE resin (300 mM NaCl) (11 - 14). Elution fraction from Superdex S75. (B) Chromatogram of Size-Exclusion. Protein was loaded onto HiLoad 16/60 Superdex S75 equilibrated with buffer 20 mM NaH_2PO_4, 200 μM EDTA pH 7.4.
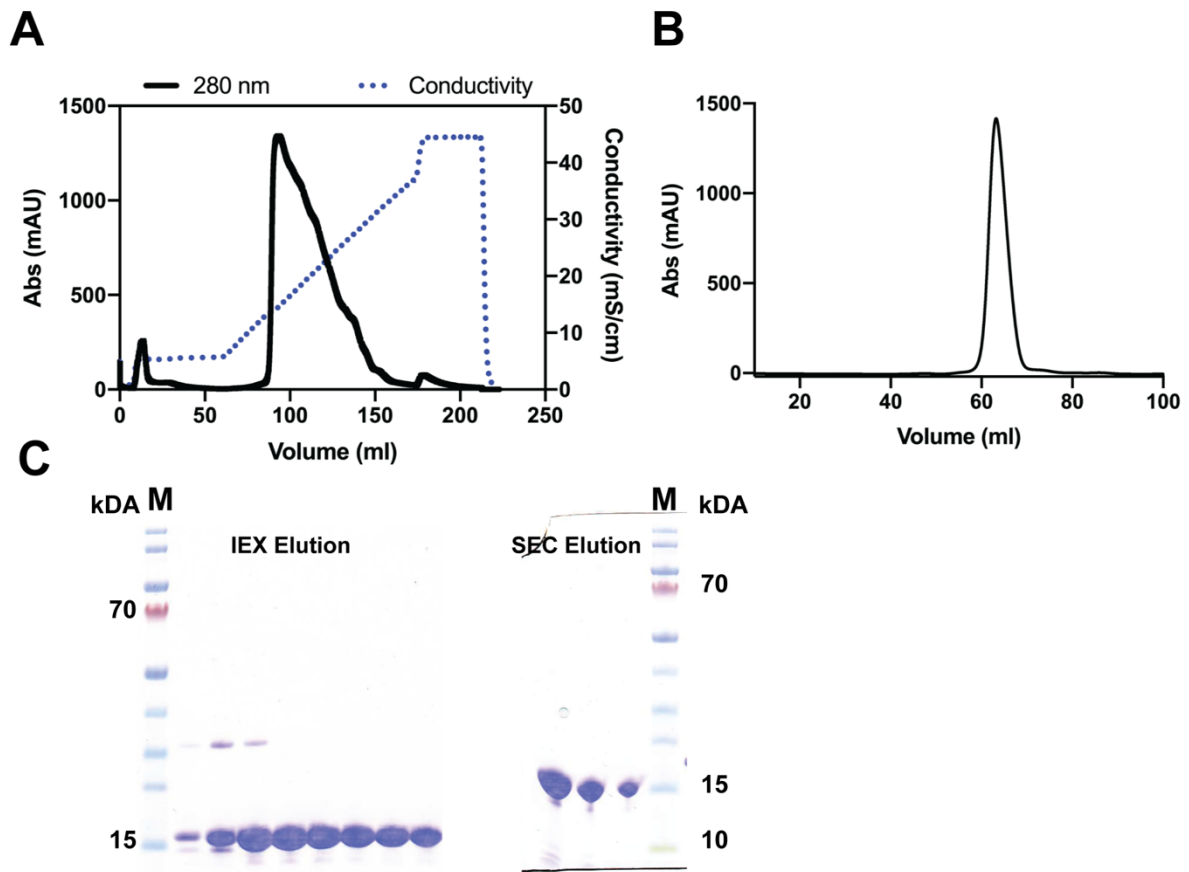
Figure 30: Overview of α-synuclein purification
(A) Chromatogram Ion exchange column. Protein was loaded onto HiTrap Q HP column. The column was washed with buffer 10 mM Tris-HCl, pH 7.5, 50 mM NaCl and eluted with a linear gradient in buffer 10 mM Tris-HCl, pH 7.5, 500 mM NaCl. The increasing gradient is shown in the increase in conductivity (blue line). Protein was detected via absorbance at 280 nm (black line). (B) Chromatogram of Size-Exclusion column. Protein was loaded onto HiLoad 16/60 Superdex S75 equilibrated with buffer 20 mM NaH_2PO_4, 200 μM EDTA pH 7.4. (C) SDS-PAGE analysis of α-synuclein. Molecular weight marker (M), Elution fraction of Ion exchange column (IEX elution), Elution fraction of S75 column (SEC elution).

7.2 ScSERF HSQC Spectra and Assignments

Figure 31: HSQC Spectra of ^{15}N ^{13}C - ScSERF.
HSQC spectra of ^{15}N ^{13}C - ScSERF with a concentration of 1.6 mM in buffer 20 mM NaH$_2$PO$_4$ pH 7.0 at 277 K (4°C) was collected at a 900 MHz Bruker AVANCE^{TM}.

Table 1 Resonance assignments for ScSERF

Residue	Cα (ppm)	Cβ (ppm)	H (ppm)	N (ppm)
A2	51.396	16.045	-	-
R3	53.952	27.907	8.374	121.185
G4	42.214	-	8.339	109.857
N5	50.122	35.746	8.232	118.778
Q6	-	25.747	8.372	120.899
R7	54.664	27.163	8.154	121.134
D8	52.503	37.68	8.021	120.845
L9	53.771	38.699	7.912	122.02
A10	51.008	15.337	7.852	122.34
R11	54.698	27.196	7.726	119.135
Q12	54.395	25.696	7.932	119.452
K13	54.987	29.678	7.996	121.29
N14	-	-	8.037	118.643
L15	53.464	38.895	7.909	121.957
K16	55.184	29.569	7.814	121.045
K17	54.564	-	7.856	121.086
Q18	53.968	-	8.005	120.343
K19	54.708	29.668	8.075	122.191
D20	53.446	36.273	8.183	121.12
M21	53.346	29.396	7.99	120.491
A22	50.264	15.67	7.877	123.439
K23	54.077	29.695	7.819	119.244
N24	50.582	35.588	8.033	118.288
Q25	53.023	26.095	7.954	120.365
K26	53.458	29.848	8.088	122.437
K27	53.313	30.006	8.213	123.038
S28	55.62	60.837	8.22	117.37
G29	41.886	-	8.264	110.831
D30	49.25	38.054	8.056	121.656
P31	60.847	29.202	-	-
K32	54.546	29.497	8.114	120.073
K33	53.755	29.764	7.775	121.272
R34	53.335	27.582	8.02	122.435
M35	53.395	-	7.835	127.615
E36	54.348	-	8.2	121.725
S37	60.833	-	8.295	117.285
D38	53.958	-	8.45	121.921
A39	52.174	15.182	8.078	122.289
E40	51.977	-	7.742	120.966
I41	61.762	-	7.788	121.391
L42	55.126	38.349	7.604	120.244
R43	56.684	-	7.795	120.295
Q44	-	-	8.053	119.331
K45	56.196	-	-	-
Q46	-	26.015	7.874	119.168
A47	54.192	14.614	7.795	122.399
A48	51.808	14.718	7.781	121.399
A49	52.173	14.745	7.692	123.153
D50	55.936	38.753	8.411	120.822
A51	52.168	14.84	7.797	122.392
R52	56.017	25.052	8.026	119.12
R53	54.909	29.73	8.034	121.855
E54	55.273	-	8.119	120.973
A55	52.073	14.619	8.05	121.795
E56	56.094	26.419	7.72	120.205
K57	56.485	29.444	7.558	120.338
L58	54.66	38.547	7.564	119.277
E59	55.893	26.319	7.736	119.581
K60	55.878	29.411	7.655	120.173
L61	54.154	38.986	7.513	119.649
K62	55.503	29.586	7.623	119.404
A63	50.634	15.623	7.638	121.961
E64	54.506	26.866	7.72	118.493
K65	54.015	29.707	7.759	120.036
T66	59.471	66.674	7.692	113.757
R67	53.322	27.63	7.905	124.138
R68	54.471	28.389	7.832	128.072

7.3   Additional kinetic fits for Aβ40 mechanisms
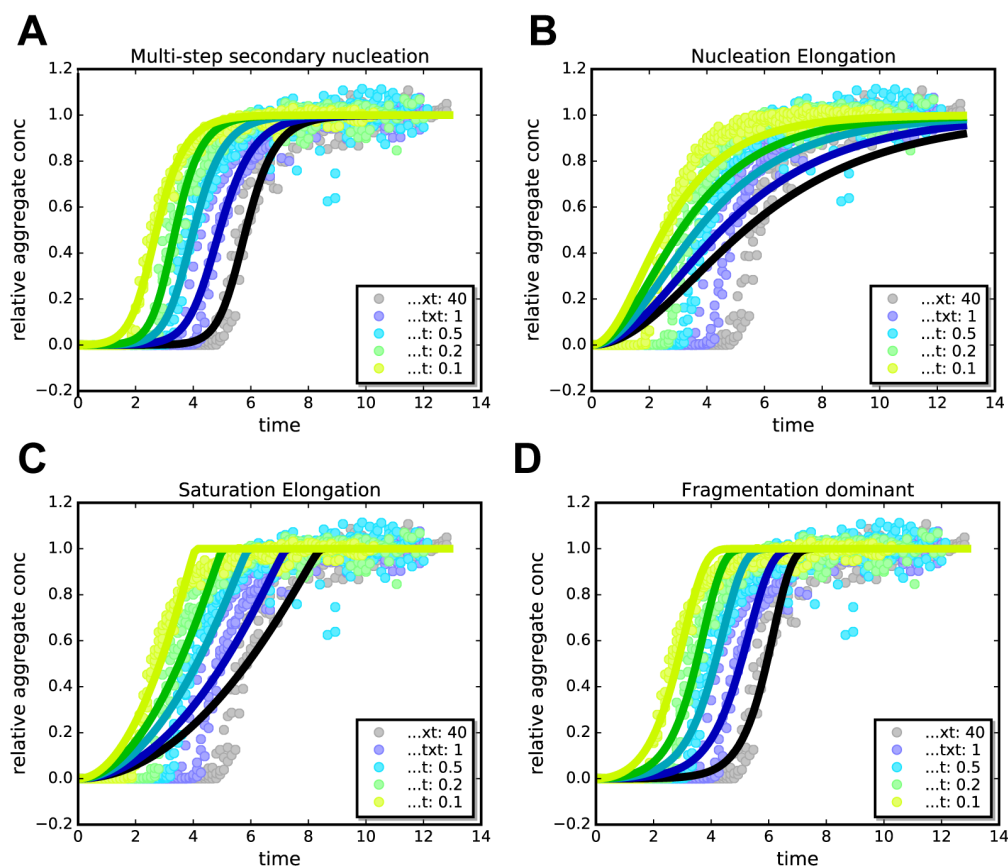
Figure 32: Alternative amyloid mechanism fitted to Aβ40 data in the presence of ScSERF.
Data was fitted with (https://www.amylofit.ch.cam.ac.uk/login) (A) multi-step secondary nucleation
mechanism (B) nucleation elongation (C) saturation elongation (D) fragmentation dominant
mechanism[41].

Table 2 Fitting parameters from fits in Fig. 13.

Aβ40:ScSERF	$k_n k_+$ [M^{-1}s^{-1}]	$k_+ k_2$ [M$^{-3/2}$s^{-1}]
1:0	7539.162559	1.94E+14
1:1	289758.5349	1.43E+14
1:0.5	800698.4702	1.85E+14
1:0.2	1820863.472	2.28E+14
1:0.1	13880596.78	2.05E+14

7.4 Aβ40:ScSERF spectra analysis and assignments

Table 3 Chemical shift changes in ^{15}N-Aβ40 upon addition of ScSERF

Amino acids		1:1Aβ40:ScSERF ΔN [ppm]	1:1Aβ40:ScSERF ΔH [ppm]	Δδ [ppm]
A2N	2	0.003297	0.002275	0.001611
R5N	5	0.029261	0.002576	0.002001
D7N	7	0.009096	0.002532	0.001809
S8N	8	0.016144	0.00217	0.001601
G9N	9	0.002211	0.002902	0.002053
Y10N	10	0.004979	0.000849	0.000617
E11N	11	0.00641	0.003222	0.002286
V12N	12	0.057689	0.003423	0.002919
K16N	16	0.013898	0.002463	0.001785
L17N	17	0.030254	0.003446	0.002583
V18N	18	0.007898	0.002543	0.001812
F19N	19	0.064496	0.003289	0.002956
F20N	20	0.026368	0.002318	0.001801
A21N	21	0.013729	0.000424	0.000491
E22N	22	0.034631	0.000572	0.00106
D23N	23	0.030708	0.005252	0.003814
V24N	24	0.038995	0.006316	0.0046
G25N	25	0.002123	0.003628	0.002566
S26N	26	0.007273	0.000396	0.000347
N27N	27	0.009433	0.002328	0.001668
K28N	28	0.011875	0.003138	0.002244
G29N	29	0.005244	0.003521	0.002494
A30N	30	0.004439	0.003001	0.002126
I31N	31	0.001924	0.00274	0.001938
I32N	32	0.025601	0.004969	0.003587
G33N	33	0.01581	0.004067	0.00291
L34N	34	0.005968	0.00261	0.001853
M35N	35	0.019482	0.003608	0.00261
V36N	36	0.013247	0.002851	0.00205
G37N	37	0.011135	0.002973	0.002126
G38N	38	0.005501	0.003542	0.002509
V39N	39	0.015086	0.002597	0.001885
V40N	40	0.014901	0.003551	0.002546

Table 4 Chemical shift changes in ^{15}N-Aβ40 upon addition of ScSERF

Amino acids Aβ40		1:3 Aβ40:ScSERF ΔN [ppm]	1:3 Aβ40:ScSERF ΔH [ppm]	Δδ [ppm]
A2N	2	0.009114	0.002923	0.002083
R5N	5	0.074145	0.00315	0.003059
D7N	7	0.06524	0.006836	0.005174
S8N	8	0.010431	0.006375	0.004517
G9N	9	0.018822	0.00474	0.003394
Y10N	10	0.012388	0.000973	0.000772
E11N	11	0.020121	0.003068	0.002243
V12N	12	0.072091	0.004143	0.003569
K16N	16	0.055774	0.00575	0.004361
L17N	17	0.063775	0.006318	0.004818
V18N	18	0.01403	0.003868	0.002764
F19N	19	0.047578	0.003595	0.002876
F20N	20	0.062493	0.001638	0.002113
A21N	21	0.033145	0.001888	0.001631
E22N	22	0.03013	0.001324	0.001266
D23N	23	0.053295	0.008165	0.005967
V24N	24	0.094389	0.012817	0.009448
G25N	25	0.010744	0.005102	0.00362
S26N	26	0.003216	0.003824	0.002706
N27N	27	0.023581	0.00057	0.000779
K28N	28	0.001242	0.005228	0.003697
G29N	29	0.015112	0.003329	0.002392
A30N	30	0.011961	0.003096	0.002215
I31N	31	0.028402	0.003219	0.002414
I32N	32	0.055518	0.007136	0.005285
G33N	33	0.027185	0.006456	0.004629
L34N	34	0.008434	0.003329	0.002366
M35N	35	0.041297	0.005901	0.004333
V36N	36	0.021582	0.005795	0.004143
G37N	37	0.024568	0.004746	0.003427
G38N	38	0.005218	0.003471	0.002459
V39N	39	0.04308	0.002514	0.002155
V40N	40	0.038528	0.004077	0.003082

Table 5 Signal intensity changes in ^{15}N-Aβ40 upon addition of ScSERF

Amino acids Aβ40	Intensity Aβ40	Intensity 1:1 Aβ40:ScSERF	Intensity 1:3 Aβ40:ScSERF	Relative Intensity 1:1	Relative Intensity 1:3
A2N-H	2.53E+11	2.08E+11	2.09E+11	0.825229	0.828116
R5N-H	1.71E+11	1.32E+11	1.13E+11	0.774073	0.661303
D7N-H	1.65E+11	1.37E+11	1.37E+11	0.830761	0.829583
S8N-H	1.36E+11	1.13E+11	9.6E+10	0.830229	0.704801
G9N-H	1.84E+11	1.36E+11	1.29E+11	0.741823	0.70076
Y10N-H	1.91E+11	1.47E+11	1.33E+11	0.769055	0.696426
E11N-H	1.95E+11	1.48E+11	1.45E+11	0.760433	0.74347
V12N-H	2.61E+11	2.09E+11	1.92E+11	0.800797	0.734943
K16N-H	1.67E+11	1.31E+11	1.26E+11	0.780707	0.753301
L17N-H	2.11E+11	1.82E+11	1.66E+11	0.863167	0.783968
V18N-H	1.73E+11	1.3E+11	1.17E+11	0.747926	0.673566
F19N-H	1.88E+11	1.6E+11	1.55E+11	0.854841	0.826974
F20N-H	2.07E+11	1.72E+11	1.72E+11	0.831501	0.828283
A21N-H	2.34E+11	1.92E+11	1.97E+11	0.820482	0.842695
E22N-H	2.73E+11	2.19E+11	2.11E+11	0.803826	0.773527
D23N-H	2.33E+11	1.8E+11	1.71E+11	0.7721	0.733749
V24N-H	3.77E+11	2.84E+11	2.3E+11	0.754481	0.611334
G25N-H	2.23E+11	1.93E+11	1.76E+11	0.86409	0.789673
S26N-H	1.7E+11	1.42E+11	1.39E+11	0.836149	0.814647
N27N-H	1.05E+11	9.06E+10	7.98E+10	0.863242	0.760244
K28N-H	2.74E+11	2.39E+11	2.15E+11	0.872583	0.785522
G29N-H	1.77E+11	1.54E+11	1.49E+11	0.869667	0.839667
A30N-H	2.27E+11	1.89E+11	1.55E+11	0.8357	0.684083
I31N-H	3.92E+11	3.42E+11	3.27E+11	0.873204	0.833908
I32N-H	2.83E+11	2.39E+11	2.38E+11	0.843948	0.838541
G33N-H	2.33E+11	1.91E+11	1.74E+11	0.82085	0.749929
L34N-H	2.55E+11	2.09E+11	1.92E+11	0.817307	0.750095
M35N-H	2.76E+11	2.07E+11	2.12E+11	0.747512	0.766334
V36N-H	4.44E+11	3.89E+11	3.79E+11	0.876339	0.852931
G37N-H	2.65E+11	2.23E+11	2.02E+11	0.843674	0.763479
G38N-H	2.8E+11	2.39E+11	2.36E+11	0.853278	0.841207
V39N-H	3.28E+11	2.59E+11	2.34E+11	0.790224	0.712694
V40N-H	4.15E+11	3.6E+11	3.69E+11	0.867866	0.890114

7.5 Abbreviations

°C	degree(s) Celsius
2-DSA	two-dimensional spectrum analysis
α-syn	α-synuclein protein
AD	Alzheimer's Disease
ATD	arrival time distribution
AUC	analytical ultracentrifugation
Aβ40	amyloid-β 1-40 peptide
C. elegans	Caenorhabditis elegans
CCS	chemical cross section
CD	circular dichroism
CSD	charge state distribution
E. coli	Escherichia coli
EDTA	ethylenediaminetetraacetic acid
h	hour
HEPES	4-(2-hydroxyethyl)-1-piperazineethanesulfonic acid
Hsp	heat shock protein
IDP	intrinsically disordered protein
IM	ion mobility
IM-MS	ion-mobility mass-spectrometry
K_d	equilibrium dissociation constant
kDa	kilo Dalton
M	molar
m	milli
μ	micro
min	minute
MOAG-4	modifier of amyloid formation
MS	mass spectrometry
MWCO	molecular weight cut off
nESI	nano-electrospray ionization
n	nano
NiNTA	nickel-nitrilotriacetic acid
NMR	nuclear magnetic resonance
OD_{600}	optical density at 600 nm
PEM	protein expression medium
PBS	phosphate buffer saline
polyQ	polyglutamine
PD	Parkinson's Disease
ppm	parts per million
ROS	reactive oxygen species
RT	room temperature
Rpm	revolutions per minute
s	second
S. cerevisiae	Saccharomyces cerevisiae
SDS	sodium dodecyl sulfate
SEC	size-exclusion chromatography
SERF	small EDRK-rich Factor
SV-AUC	sedimentation velocity analytical ultracentrifugation

TEM	Transmission electron microscopy
ToF	time of flight
ThT	Thioflavin T
Tris	tris(hydroxymethyl)aminomethane
Ura	uracil
v/v	volume per volume
w/v	weight per volume
WT	wild type
x g	times gravity
δ	chemical shift

8 Publications & Presentations

Publication relevant to this thesis:
1. **Meinen BA**, Gadkari V V., Stull F, Ruotolo BT, Bardwell JCA (2019) SERF engages in a fuzzy complex that accelerates primary nucleation of amyloid proteins. *Proc Natl Acad Sci* **116**(46):23040–23049.

Other Publications:

2. Chick JK, Moiseeva V, Goel PK, **Meinen BA,** Koldewey P, An S, Mellone BG, Subramanian L, Cho US. (2019). Structures of CENP-C cupin domains at regional centromeres reveal unique patterns of dimerization and recruitment functions for the inner pocket. J Biol Chem 294(**38**):14119–14134.

3. Teixeira, F., Tse, E., Castro, H., Makepeace, K. A. T., **Meinen, BA.,** Borchers, C. H., … Jakob, U. (2019). Chaperone activation and client binding of a 2-cysteine peroxiredoxin. *Nat. Commun.* **10**, 659

4. Yoo N, Dogra S, **Meinen BA**, Tse E, Haefliger J, Southworth DR, Gray MJ, Dahl JU, Jakob U. (2018). Polyphosphate Stabilizes Protein Unfolding Intermediates as Soluble Amyloid-like Oligomers. *J Mol Biol* 430(**21**):4195–4208.

5. Cristie-David AS, Koldewey P, **Meinen BA,** Bardwell JCA, Marsh ENG (2018) Elaborating a coiled-coil-assembled octahedral protein cage with additional protein domains. *Protein Sci* 27(**11**):1893–1900.

Oral presentations:
Meinen BA. *ScSERF acts as a modifier for Aβ amyloid formation in vitro*, 24th Midwest stress response and molecular chaperone meeting. 2019 Jan.
Meinen BA. *ScSERF acts as a modifier for Aβ amyloid formation in vitro*, MCDB Department Retreat, 2018 Oct.

Poster presentations:
Meinen BA. *SERF a novel modifier of amyloid formation*, Poster presentation, FASEB Meeting: Protein Folding in the Cell. 2018 Jul.
Meinen BA. *SERF a modifier of amyloid formation,* Poster presentation, HHMI Science Meeting at Janelia Research Campus. 2017 Sept.
Meinen BA. *Using a cytosolic folding sensor to uncover new chaperones*, Poster presentation, FASEB Meeting: Protein Folding in the Cell. 2016 Jul.

9 Curriculum vitae

Contact details:
Permanent address:
Gustav-Linden-Strasse 53
40878 Ratingen, NRW, Germany
Email: meinen.ben@gmail.com

Personal Information

Last Name	Meinen
Surname	Ben Alexander
Date of birth	29.01.1990
Place of birth	Düsseldorf
Nationality	German

Education

2000-2009	Abitur, Carl-Friedrich von Weizsäcker Gymnasium, Ratingen
2009-2012	Bachelor of Science, Biochemistry, Martin-Luther-University Halle-Wittenberg
2012	Bachelor Thesis *"Expression and Purification of 4-hydroxybenzoic acid oligoprenyltransferase from S. cerevisiae"* Supervisor: Prof Dr. Milton T. Stubbs
2012-2014	Master of Science, Biochemistry, Martin-Luther-University Halle-Wittenberg Grade: 1.6
01-08/2014	Master Thesis: *"Characterization of protein-membrane-interaction of the N-BAR-Domain from the protein BIN1"* Supervisor: PD Dr. Hauke Lilie, Prof Dr. Jochen Balbach Grade: 1.0 Awarded with the Master Price 2015 by the Society for Biochemistry and Molecular Biology (GBM)

Graduate studies

03/2015-2020	Ph.D. student at Martin-Luther-University Halle-Wittenberg, PD Dr. Hauke Lilie Graduate Researcher at University of Michigan, Ann Arbor Dissertation research conducted with Prof Dr. James Bardwell (University of Michigan) Title *"SERF is as a modifier of amyloid formation"*

10 Acknowledgements

I am very thankful for the experiences and opportunities I encountered in the last five years, that all together helped me grow as a scientist and human being.

First and foremost, I want to thank **Prof. Dr. James Bardwell** for his support and the opportunity to do research in his lab that the University of Michigan. I am thankful for his encouragement, ideas, enthusiasm, advice, positivity and ability to find and initiated great collaborations for my projects.

I also want to thank **PD Dr. Hauke Lilie** for supporting me and being my official advisor. I am grateful for his trust in me and the training I obtained as a master student in his lab, that prepared me for my graduate studies.

Furthermore, I would like to thank my great collaborators. I want to thank **Dr. Varun Gadkari** and **Prof. Dr. Brandon Ruotolo** for the great and productive collaboration on the Native-IM-MS data. I want to thank **Dr. Josh Damron** and **Dr. Debashish Sahu** for the help collecting NMR Data. I want to thank **Dr. Michael Cianfrocco** and **Dr. Tony Ludlam** for helping with the negative-staining and transmission electron microscopy. I want to thank **Prof. Dr. Sheena Radford** for her input in the early stages of the project.

I want to thank every member past and present in the Bardwell lab for providing and creating a great and supportive atmosphere in and outside the lab. I want to thank Rishav, Veronika, Kevin and Mark who share the graduate student experience with me. Especially, I want to thank Ricky, Phil and Scott for all the help and the lessons I have learned from you guys. I am thankful for May, Ken, Molly and Chris for all the lab and administrative support. Also, special thank goes out to the Jakob lab for the productive discussions during our joint lab meetings.

At this point I like to thank all my new friends I made while being in Ann Arbor and all my friends that supported and visited form a far. I am lucky to have meet you and I am grateful for the great time. I would like to thank my partner Sumin who patiently listened to all my problems, concerns, insecurities and supported me personally and scientifically. I could not ask for a better partner. Last but not least I want to thank my mother, brothers and my family, who came to visit me multiple times and supported me from a far.

11 Statutory Declaration

Ich erkläre an Eides statt, dass ich die Arbeit selbstständig und ohne fremde Hilfe verfasst, keine anderen als die von mir angegebenen Quellen und Hilfsmittel benutzt und die den benutzten Werken wörtlich oder inhaltlich entnommenen Stellen als solche kenntlich gemacht habe. Teile dieser Arbeit wurden in einem wissenchaftlichen Journal publiziert.

Weiter erkläre ich, dass ich die vorliegende Dissertation an keiner anderen wissenschaftlichen Einrichtung zur Bewerbung eines Doktorgrades eingereicht habe. Ich selbst habe mich noch nicht um einen Doktorgrad beworben.

Ratingen, den 25.06.2020

Ben Alexander Meinen